UNIVERSITÀ
DEGLI STUDI
DI PADOVA

Università degli Studi di Padova

Dipartimento di Ingegneria Industriale DII

Corso di Laurea Magistrale in Ingegneria dei Materiali

Non-destructive evaluation of 3D printed materials using air-coupled ultrasonic technique

Relatore: Prof. Giorgia Franchin

Correlatore: Dott. William M. D. Wright

Laureando: Matteo Scorrano

Anno Accademico 2021/2022

Ringraziamenti

Desidero ringraziare innanzitutto l'Università degli Studi di Padova e l'Università di Cork, che insieme al loro accordo mi hanno permesso di svolgere molto più di una semplice tesi sperimentale. Un ringraziamento speciale al mio supervisore e correlatore, il Dottor Bill Wright, che, sin dal primo giorno e per tutto il periodo di permanenza in Irlanda, mi ha dato piena fiducia e disponibilità. Allo stesso modo ringrazio la mia relatrice, la professoressa Giorgia Franchin, che mi ha seguito e consigliato a distanza, portandomi a compimento di questo percorso accademico.

Ringrazio i miei genitori e mia sorella per aver reso tutto questo possibile e aver creduto in me in ogni momento non facendomi mai mollare, e Francesco, che durante il lockdown ed oltre è stato il personal trainer della famiglia. Infine ringrazio tutti i miei amici, quelli di una vita, che durante le ultime estati non mi hanno mai lasciato a piedi, Alice e Martina che mi hanno dato forza nei momenti più difficili, Valerio per essere stato la copisteria di fiducia per tutta la durata della magistrale e tutti quelli che seppur da meno tempo, riescono a far sentir meno la mancanza del Salento.

Acknowledgement

Thanks to the University College of Cork who hosted me and gave me the opportunity to do this work in their laboratories. Thanks in particular to my supervisor, Dr Bill Wright, who made himself available and gave me confidence throughout my stay in Ireland.

Abstract

3D printing for prototyping and manufacturing components has become increasingly popular in recent years due to the improvement of available printers and cost reductions. One of the most widely used technologies is FDM (Fused Deposition Modelling), which involves the deposition of polymer filaments in overlapping layers by extrusion from a heated nozzle.

The increasing use of this technique, and the fact that 3D printed products can have various defects, has increased the demand for characterisation of these objects to check their quality. Among the various existing techniques, ultrasound emitted by non-contact probes has been used in this study.

Due to the non-use of a coupling agent, this technique allows for faster analysis and is an excellent alternative to traditional immersion or contact methods.

Various samples differing in size, filling density, infill pattern were 3D printed and excited with ultrasound probes, evaluating the effect of these characteristics on ultrasonic propagation in the specimens. In particular, the aim is to understand the internal pattern with which they are made and the orientation along which the test is carried out, searching for measurable relationships between the speed of sound and signal intensity with the different internal patterns and densities.

The results obtained, although not always predictable, gave important and encouraging answers, showing that non-contact ultrasound inspection is a promising technique for analysing 3D printed objects.

Sommario

La stampa 3D per la prototipazione e la produzione di componenti è diventata sempre più popolare negli ultimi anni, grazie al miglioramento delle stampanti disponibili e alla riduzione dei costi. Una delle tecnologie più utilizzate è la FFF (Fused Filament Fabrication), che consiste nel deposito di filamenti polimerici in strati sovrapposti, mediante estrusione da un ugello riscaldato.

Il crescente utilizzo di questa tecnica e il fatto che i prodotti stampati in 3D possono presentare vari difetti, ha aumentato la richiesta di caratterizzazione di questi oggetti per verificarne la qualità. Tra le varie tecniche esistenti, in questo studio sono stati utilizzati ultrasuoni trasmessi da sonde senza contatto. Grazie all'assenza di un agente di accoppiamento, questa tecnica consente un'analisi più rapida e rappresenta un'ottima alternativa ai metodi tradizionali a immersione o a contatto.

Sono stati stampati in 3D campioni differenti per dimensione, modello e densità di riempimento, in seguito eccitati con sonde a ultrasuoni, per valutarne l'effetto di queste caratteristiche sulla propagazione degli ultrasuoni all’interno dei campioni stessi.

In particolare, l'obiettivo è capire il modello interno con cui sono realizzati e l'orientamento lungo il quale viene effettuato il test, cercando relazioni misurabili tra la velocità del suono e l'intensità del segnale con i diversi modelli e densità interne.

I risultati ottenuti, anche se non sempre prevedibili, hanno dato risposte importanti e incoraggianti, dimostrando che l'ispezione a ultrasuoni senza contatto è una tecnica promettente per l'analisi di oggetti stampati in 3D.

Contents

Chapter 1

3D printing objects

3D printing, more properly called additive manufacturing (AM), allows for the creation of 3D objects without the aid of moulds by depositing overlapping layers of material until the desired shape is reached. It is therefore different from conventional processes that are subtractive or formative. In drilling or milling, which are examples of subtractive manufacturing processes, the material is eliminated from a solid block to achieve the desired shape [1], while in forming processes such as lamination or forging this is achieved by applying a certain stress to the material [2]. By producing functional components as opposed to mere prototypes, the manufacturing industry aims to meet industrial requirements comparable to those of conventional technologies [3].

1.1 Advantages and disadvantages

The main advantages of 3D printing are that it is possible to create complex shapes at high precision (figure 1.1a) that could not be manufactured otherwise, and to reduce the amount of material needed as well as the product manufacturing cycle [4]. In fact, as already mentioned above, it is not a subtractive process but the only material used is that necessary to produce the final object. In any business model, one of the most important aspects is definitely the reduction of costs, and it was demonstrated that by 3D printing it is possible to save up to 25% of energy and reduce up to 90% of the material and waste [5] in comparison with traditional manufacturing methods. The reduction in costs is achieved among other things also with regard to travel and logistics costs, as the digital design of an object can be realised in one place and sent by email to be fabricated where it will be used; for example, spare items can be produced on site and on demand [6]. Reduced storage and

logistics requirements lead to a decrease in the environmental impact of production. In addition, additive manufacturing is becoming more and more versatile with respect to the feedstock material, starting from polymers and moving into rubbers, resins, metals, ceramics, glass, and also concrete for the construction of houses (figure 1.1b). In this regard, an additional advantage is represented by the reduced time of operation. In fact, this kind of process is faster than conventional construction methods: the time needed to build the structure of a house ranges from one to three days depending on its size [7], with minimal human intervention required. It should be noted that the final properties of the printed part are crucially influenced by the choice of material and its characteristics, which are important factors to consider [8].


a.

b.

Figure 1.1a. Complex shape of a 3D printed lamp [9]. Figure 1.1b. 3D printed house [10]

Recently, 3D printing of composite structures was achieved by combining a reinforcing material with a polymer matrix [11], such as carbon fibre reinforced plastic (CFRP). The ability to print multiple materials at the same time through multiple printheads allows to increase the operating speed of 3D printers [12].

When considering mass production, this technique is slower and therefore conventional ones are preferred, while AM is preferred for custom production. Other shortcomings include limited build

volumes, with the consequence of having to assemble multiple parts for the fabrication of bigger components. In addition, AM processes often use liquid polymers, resins or plaster powders with limited mechanical properties, and the rough, imperfect surface often resulting from the process can aggravate such limitations [13]. The price of printing equipment, particularly printer and filament materials, might be an initial obstacle, but as the technology progresses, prices are expected to drop in the coming years.

With respect to AM employment in prototyping, the probability of producing flawed components is low as multiple design iterations are possible with no added cost. All necessary changes are implemented into the computer-aided design (CAD) model which is then sent to the printer to realise a single prototype. Modifications are easy to realise and allow to generate also customized products. With many printers, the job can be paused in case problems are encountered during the operation, giving a chance to solve them and start again from the same point [14].

1.2 Application and growth

Various industries benefit from additive manufacturing. The ability to customize products is being exploited in the medical field for the production of dental implants or custom-made prostheses after scanning the patient with CAD software. The next objective in this field is to print fully functional organs. One of the biggest difficulties resides in the reproduction of capillaries with diameters in the order of 5 to 10 microns, smaller than the resolution of most printers and thus extremely small to be accurately reproduced [15]. Another main application is the manufacturing of lightweight yet mechanically sound components. More than 20% of the AM market is covered by the automotive and aerospace industries [16]. Maintenance tools and spare parts could potentially be printed directly aboard space stations [12]. Another application that could revolutionize current

manufacturing is food production. Although it is still in its infancy, it points to positive goals such as solving food scarcity problems, eliminating malnutrition, reducing climate change, etc. [17].

AM production has experienced significant growth in recent years, and this is expected to persist [18]. Over time the quality it offers is increasing and at the same time the costs are decreasing gaining relevance and enabling more and more industries to adopt it [12, 19]. With the increased use of 3D printing in the automotive, aerospace and medical industries, it is expected that these fields will cover 84% of the 3D printing market by 2025 according to Lux Research [20]. Taking into account the slowdowns that have occurred in the progress of this technology in recent years due to the COVID-19 pandemic, Imarc Group estimates that the global 3D printing market will reach US$57.1 billion by 2027 [21].

1.3 Mode of operation

A general AM process (in the example, fused filament fabrication or FFF) can be divided into three phases: Design, Manufacturing and Testing (figure 1.2) [22].

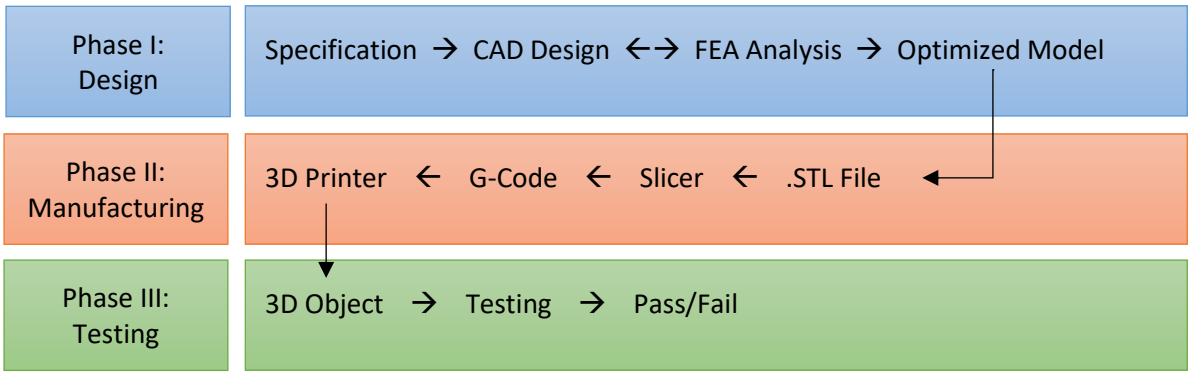

Figure 1.2 Outline AM process chain.

The basic principle of 3D printing is to make an object on a platform by accumulation of material in overlapping layers, obtained by converting a complex three-dimensional model [23]. As mentioned

earlier, a CAD model is used as a starting point for the realization of a 3D printed object. There are a lot of software tools that can generate a 3D printable CAD model and among them, in the studies that will be carried out here, Solidworks will be used.

Once a 3D model has been created, finite element analysis (FEA) can be performed in order to verify that the initial specifications are fulfilled and possibly modify the design to meet them. The final design is then converted to a standard tessellation language file (STL) that is sent to the printer slicing software. The software slices the 3D model in numerous layers parallel to the printing platform and produces a machine path file in a language that can be processed by the printer (G-Code). Finally, the new file is sent to the printer that will proceed with printing the object layer by layer. There are several slicing programs that can transform a STL into a G-Code file; here, Ultimaker Cura was used. Instructions encrypted by the G-code file include the quantity of material extruded, the movement of the head along the x-, y- and z-axes, its speed, as well as where to place multiple objects on the printing plate and where support material is needed [22]. This manufacturing technique allows for the rapid production of prototypes and models of parts or even finished products. In both cases, before they are bulk produced, it is necessary to proceed with checks and tests of the products [12]. These tests are both mechanical and physical, can be destructive or non-destructive, and are performed for validation and quality control, differing in execution time and resolution [22].

1.4 Additive manufacturing processes

According to the ASTM standard, there are 7 categories into which AM processes can be divided. The additive manufacturing processes can be differentiated particularly according to the instrumentation used and the way of operating, therefore they are classified as follows: [24]

- *Material extrusion*: the material is deposited with a continuous flow layer by layer by a nozzle. The material adheres to the previous layer thanks to gravity and to its liquid state as it is either fused (fused filament fabrication, FFF) or deposited as a paste (direct ink writing, DIW).
- *VAT photopolymerization*: in this process, a vat of liquid photosensitive polymer resin is used, and a laser beam or a light projector sketches a shape in the resin, creating a hardened (cured) layer. Then the build platform is moved to generate a new layer of fresh resin and the operation is repeated until the object is completed.
- *Powder bed fusion (PBF)*: a layer of powdered material is selectively melted (or sintered) by a thermal energy source, i.e. an electron beam or laser. Once the first layer is completed, the tool lays down a new layer of powder on the build platform and the process is iterated. In PBF process a rapid solidification of the layers occurs and they bond together forming the final part [25].
- *Material jetting*: the material in form of droplets is deposited by a printhead on the surface, then solidifies thanks to solvent evaporation or UV light hardening.
- *Binder jetting*: the difference with the previous technology relies in the combination of a powdered bed and a binder material. First, the powder bed is deposited by a roller on the build platform and then it is selectively wetted with a liquid binder. The latter consolidated or reacts with the powder bed, in each case allowing the formation and adhesion of the layers.
- *Sheet lamination*: this family includes ultrasonic additive manufacturing (UAM) and laminated object manufacturing (LOM). In the first case, sheets of metals are joined by ultrasonic welding, while in the second case, sheets of paper and an adhesive are utilised.
- *Directed energy deposition*: is used in particular with metal material, in form of powder or wire form, that is melted by an electron beam and is deposited by 4-5 axes robotic arms.

1.5 FFF technology

The additive manufacturing techniques just listed are similar in producing objects by depositing and bonding materials in layers but differ in the way they operate. A classification into four categories is possible considering the state of the material used: liquid, filament, powder and solid sheet [13]. Among them we consider the extrusion of material in the form of a continuous filament. This technique emerged under the name Fused Deposition Modelling (FDM) when it was patented by the company Stratasys Ltd. So, for other companies interested in using this technique, it was deemed necessary to use another, more general term, that is, Fused Filament Fabrication (FFF) [26]. An FFF 3D printer (figure 1.3) deposits material on the printing plate in the form of filament by extruding it from a nozzle that can have different diameters.

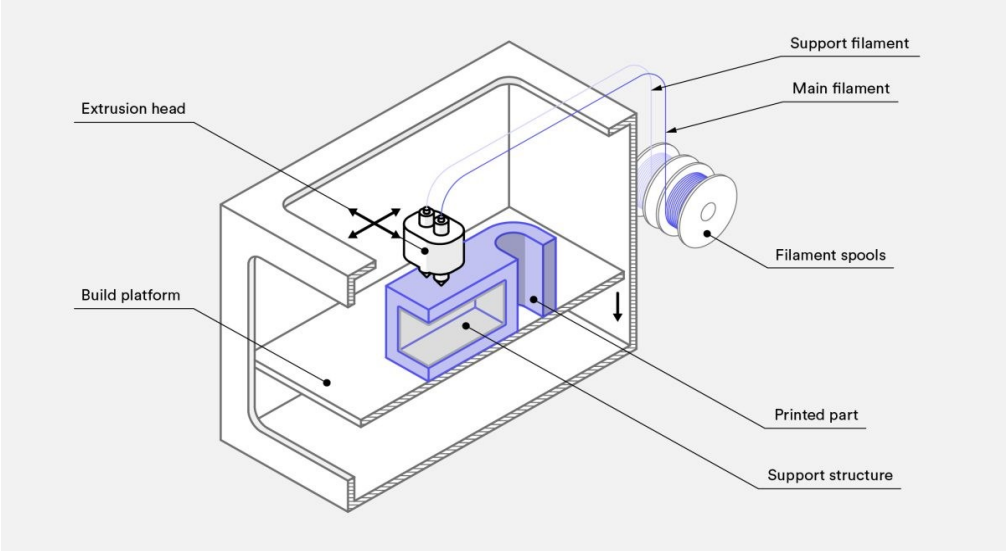

Figure 1.3 Draft of FDM 3D printer [27]

The typical materials used are ABS (Acrylonitrile butadiene styrene) and PLA (Polylactic acid), but other polymers such as PET (Polyethylene terephthalate), Nylon, TPU (Thermoplastic polyurethane), and PC (Polycarbonate) are also used [28]; the properties of the thermoplastic

filament determine the resolution of the extrusion and the performance of the final component [29]. In order to allow the material to adhere to the previous layer and solidify quickly, the filament is heated at around 2 °C above its melting point [13]. Sometimes the use of support material may be required to make support structures [30]; this is usually of the same material as that of the component (figure 1.4), but it can also be soluble in liquids to facilitate its removal. The use of support material often results in increased process cost. Two spools of filaments then act to provide the necessary materials. The material is then deposited in layers which gradually cool and solidify until the end of the process.

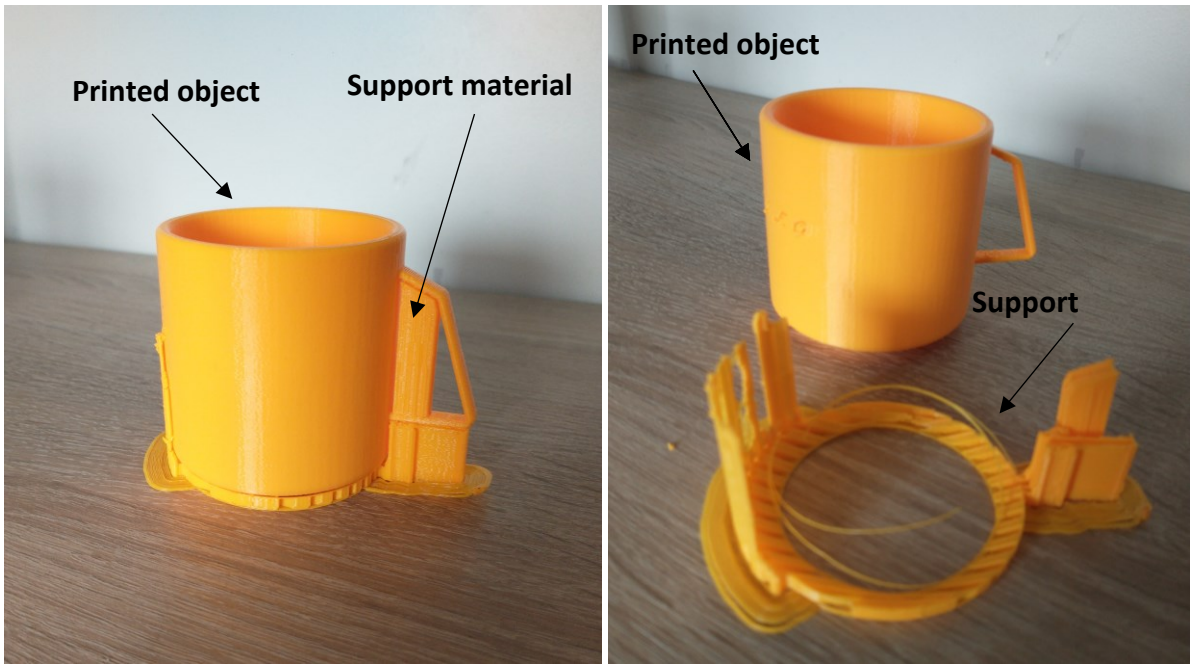

Figure 1.4 3D printed PLA object with PLA support material

1.5.1 Process parameters in FFF

In order for the process to run smoothly and guarantee an optimal result, it is important to choose proper parameters, comprising process parameters embedded in the slicing software configuration, and material parameters resulting from the properties of the filament to be extruded. Examples of

the first category include air gap, infill density, infill pattern, print speed, layer thickness, extrusion and platform temperatures, and build orientation [31]. The build orientation indicates at what angle the object is placed on the printing plate. The latter is heated to a certain temperature to promote print adhesion, as is the heat supplied to the extrusion head to melt the filament from the spool. The main disadvantage of the process is the so-called stair stepping effect on the objects surface, due to the layer by layer build-up of material, particularly visible on inclined or rounded surfaces [32]. The resulting surface is therefore characterised by high roughness in the micrometres range [29]. To improve surface quality, it is possible to print with a lower layer height for greater accuracy and smoother components. Consequently, production would take longer than a process with wider layers, which would be faster, cheaper, but of lower quality. However, post-processing might still be necessary if a high surface quality is required.

1.5.2 Characteristics influencing quality and accuracy

There are common issues in every FFF process despite the choice of proper parameters: these include part warping, presence of a pattern in the object, removal of support structures and poor material adhesion [27]. During the production of the part, the different layers cool at different speeds and therefore at different times. Cooling leads to shrinkage and inhomogeneous cooling develops internal stresses. Large, flat areas are more prone to warping, as well as specific materials such as ABS (figure 1.5). To avoid this phenomenon, the temperature of the plate and of the printing chamber should be controlled, and adhesion between the plate and the extruded material should be promoted.

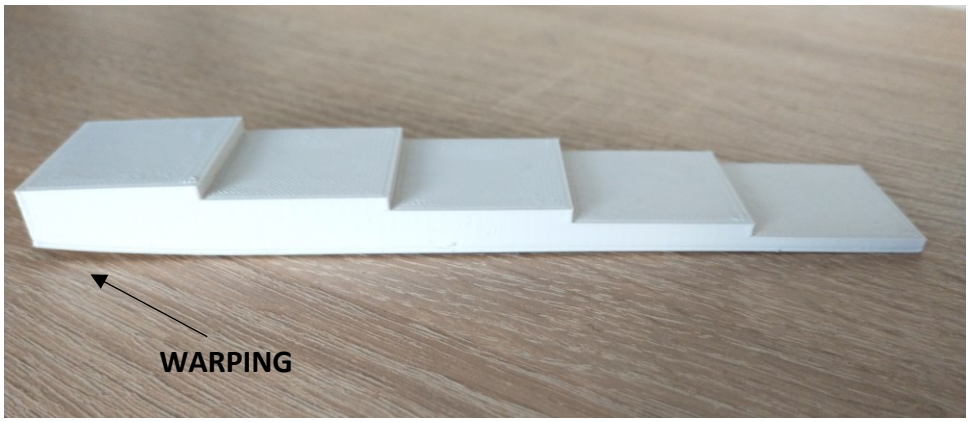

Figure 1.5 ABS specimen with warped base

Generally, parts produced with the FFF technique are not solid but have a low-density internal structure, named infill, enclosed between walls, named shells. Thus, shells are the outer layers of a 3D printed object and are generally the first parts to be fabricated. Low density infill allows for faster and cheaper printing; infill geometry and percentage of solid vary according to the required functionality of the part (figure 1.6). For non load-bearing applications, 20% infill is usually selected, but this value can increase proportionally to the required strength. In fact, a 25% increase in strength is obtained by going from a 25% infill to one of 50%, while going from 50% to 75% infill results in a 10% improvement in strength [33]. Usually, a grid pattern is used as it allows for cheap and quick production, while if greater strength is required, a 3D part made with a triangular pattern is a better choice.

Figure 1.6 From left to right, infill pattern: grid, octet, cross 3D

Adequate adhesion is essential for making good quality objects, both between layers and between the component and the printer plate. When the nozzle deposits material on the previous layer it applies pressure to make it adhere, and this tends to widen the profile of the extruded material providing for a higher contact area. Adhesion problems occur particularly when there is no proper temperature of the printing plate or chamber. As you can see from figure 1.7a, when the part does not adhere well to the plate, it can detach resulting in incorrect continuation of the process. In detail, in figure 1.7b, it is possible to see that successive layers did not have proper adhesion, due to the movement of the part during processing or inadequate temperature of the environment.

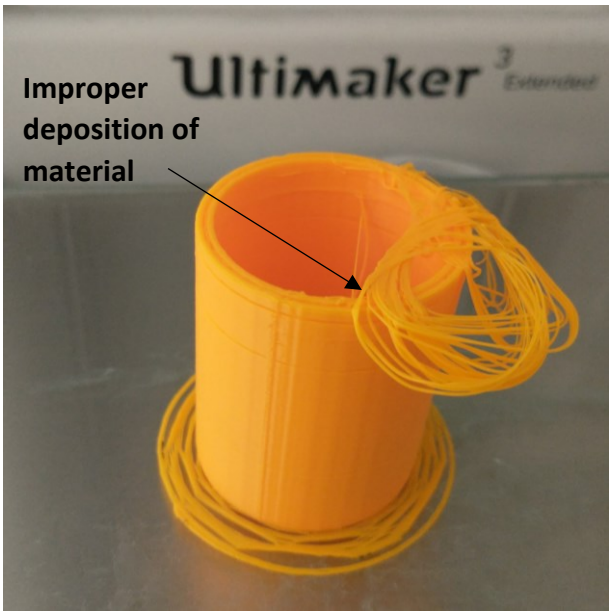

a.

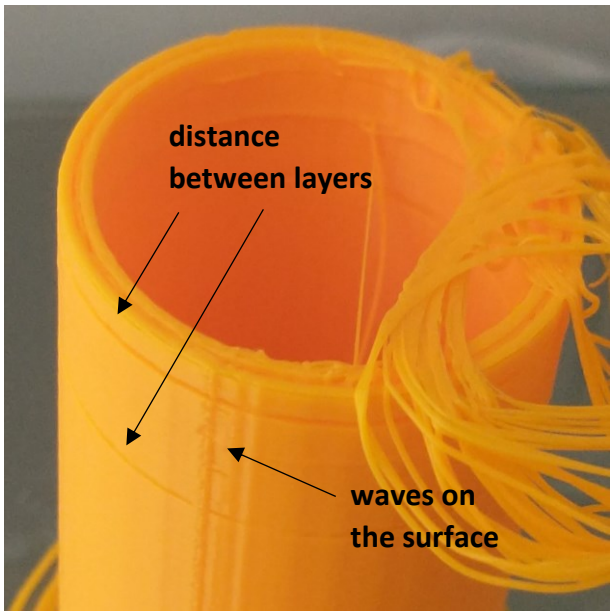

b.

Figure 1.7 Defected object due to its detachment from the platen (a) and low layers adhesion (b)

The above mentioned parameters, selected at the design stage, determine the quality of the final product, including dimensional accuracy. Minor or major defects may occur during the printing of the part as a result of an inadequate calibration of the various components of the printer. According to [34], defects may be generated by a misalignment of the printing plate or nozzle, nozzle obstruction, depletion or discontinuity of the material filament, vibrations. Calibrating the printing

plate and the nozzle is important to prevent the distance between the two from being too far apart such that the print does not adhere or too close together, resulting in a different design from the one designed. An insufficient spool of filament could leave the product incomplete, but a clogged nozzle and frayed, broken or tangled filament can also ruin the model [35].

As already mentioned, the choice of parameters also affects mechanical properties, such as tensile strength, compressive strength and flexural strength. The highest tensile strength is achieved by arranging the filaments parallel to the load, that is, with a 0° build orientation, and the same happens for flexural strength. A high infill density and a large number of shells on its turn improve both tensile and compressive strength [31].

To avoid printing errors with consequent waste of material, the process can be controlled by a user watching a web cam placed in the work room that gives him the possibility of remote supervision [36].

Chapter 2

Products control

As the quality of parts manufactured via FFF can affected by dimensional inaccuracy and the presence of defects, it is important to incorporate offline and online quality control methods to the process flow chain. Online quality control is of utmost relevance, because in case of errors during the execution the process can be stopped limiting loss of time and material.

2.1 Categories of defects

In the previous chapter, some problems related to the FFF technique and the consequences on 3D printed products were analysed. These problems may be due to the production equipment and process, of which as we have seen proper calibration and choice of parameters is required, and to the material. The internal defects present can be of different types: cracks, porosity, balling, and thermal or internal stress which reduce the quality of final parts. Understanding these defects is important in order to reduce them.

Due to thermal stresses, the formation of internal cracks is common, and in particular the choice of process parameters is a determining factor in their occurrence [37]. Because of the considerable temperature variation, thermal stresses develop, that cause dimensional variations in the component prone to generate a fracture [25]. The entity of these thermal stresses can be limited with proper choice of process parameters, material properties, component height and thickness of the deposited layers [38].

Pores in FFF components, usually small and spherical, are generated due to trapped gases as a result of the melting and rapid solidification of the material, which does not allow their complete release

[25]. Moreover, the material can solidify in spheres at the nozzle instead being deposited, a phenomenon often referred to as balling [39].

In order to produce fully functional products, mechanical properties and surface quality must be improved by reducing manufacturing defects through the use of inspection techniques, which are more and more employed in AM processes. Ideal inspection techniques are cheap and able to pick up different types of defects quickly, both on irregular surfaces and with complex shapes [40]. Some test methods allow to analyse also the internal structure of the sample and provide information on the depth, size, contour and category of internal and surface defects that can cause premature failure [41]. Finally, data on material properties and mechanical performance (such as elastic, plastic and viscoelastic behaviour, yield and rupture strength, hardness, fracture toughness, fatigue strength, etc.) can be collected in order to assess their quality and compare different feedstocks.

2.2 Testing methods

The 3D printed products could be inspected with two methods: destructive or non-destructive. Some of the differences between the two types of tests are that in destructive testing, generally of mechanical nature, a load is applied until the material properties are altered and the object fails; non-destructive tests usually involve electromagnetic waves and do not interfere with the material and object properties [42].

2.3 Destructive testing methods

These are methods that give quantitative information thanks to direct measurements of mechanical and chemical parameters. The conditions of the process are severe enough to bring the sample to

break, for this reason after the test it can no longer be used. These, being destructive, are not performed on the final part, which is necessary for the final use but on a certain selected number of samples or prototypes. [43]

In fact, in mechanical tests, a static or dynamic load is applied to the sample or product up to failure or up to an established deformation level. The first type includes tensile test, compression test, bend test, creep test, etc., where a constant load is applied gradually, while in a dynamic (or impact) test, the specimen is subjected to a rapid load like Charpy or Izod test. There are then cyclic tests, where a stress is applied periodically with a certain frequency.

2.4 Non-destructive testing methods

Non-destructive testing methods allow to verify the quality and structural integrity of the final parts to be sure that they can withstand reliably and are suitable for any subsequent processing. Furthermore, they can be used for regular inspection during components maintenance. For these reasons, these techniques are used both during and after manufacturing process. The quality of the finished product involves different factors such as dimensional accuracy, surface quality, mechanical properties and microstructure.

The aim of these tests is to be conducted without damaging the tested components; for this reason, they are defined as non-destructive techniques (NDT).

The AM products can be analysed with several techniques that have been developed over the years, both individually and combined, including [44]:

- *Visual Inspection*: the defects are detected optically, with the naked eye or with the help of a microscope.

- *Penetrating liquid*: the surface of the product is covered with a low viscosity liquid that penetrates the cracks and then is removed to reveal the defect. It is used for detecting surface defects.
- *Radiography:* in this case are used x-rays or γ-rays to detect internal flaws. These rays penetrate the solid materials and depending on the density and thickness of the sample they are in part absorbed and then detected by a film on the opposite side to the source of rays.
- *Magnetic detection*: the component, ferromagnetic, initially is magnetised. The magnetic flux lines will be distorted at the crack where another North and South region is created and the iron particles is collected. In this way the presence of the crack is displayed.
- *Eddy current*: electrically conductive materials are inspected with this technique to discern superficial defect and near the surface. A coil, in which an alternating current flows, is approached to the surface of a material so the variable magnetic field of the coil creates eddy currents within the test piece. Consequently, is generated a magnetic field that opposes the first. The presence of cracks is demonstrated by controlling variations in Eddy current flow.
- *Ultrasonic test*: mechanical vibrations, known as ultrasonic waves, are generated by a transducer and propagate through the material (solid, liquid or gas). The waves may be subject to scattering or reflection by flaws. Due to variations in propagation direction and intensity, information about defects are collected.

Chapter 3

Ultrasonic non-destructive testing

As seen in the previous chapter, among the non-destructive techniques we find the analysis of materials by ultrasound. Now the method will be analysed in detail describing the procedure, the principles underlying the method, the instrumentation and data representation.

3.1 Basic principles

Ultrasonic testing (UT) is a versatile technique for inspecting materials and is one of the most used among the non-destructive ones. This is due to several advantages:

- it has a high penetration depth,
- it can detect both surface and internal defects,
- a minimum preparation of the components is required,
- it is fast and economical.

It exploits the propagation of longitudinal and transverse waves in the medium allowing information to be obtained about changes in physical properties such as elasticity and strength of the material [45].

In order to explain the examination principle, the pulse echo method is here introduced.

UT exploits the propagation of ultrasonic waves within materials (solids, liquids or gases). When there are no defects in the material, the wave travels through it until it reaches the back-wall of the component and is reflected back (back surface echo); if it encounters a discontinuity (such a fracture), the wave is deviated and part of its energy is reflected back or scattered, producing a different echo between the initial and back wall echo that reduces its amplitude (figure 3.1). During

its propagation, the ultrasound wave collects information about the material so that by analysing the echoes it is possible to obtain information on the position of the defects according to the propagation delay, and on the shape and size according to the variation in amplitude and frequency, respectively.

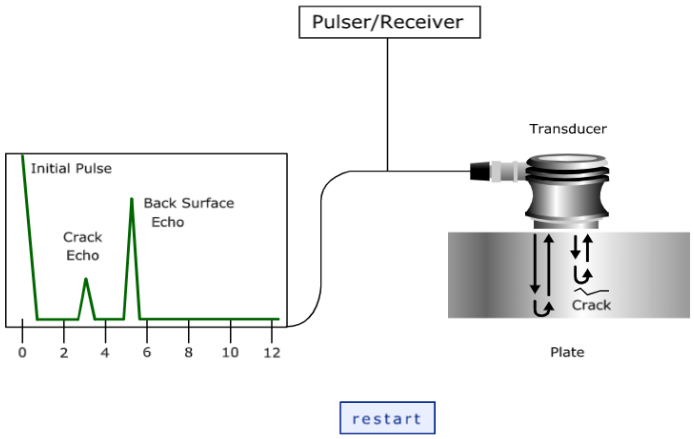

Figure 3.1 Transducer and flaw detector screen display

The most common technique uses an electronic device, pulser/receiver, to produce high voltage pulses which stimulate a transducer that converts electrical energy into ultrasonic energy. These waves that will propagate in the material as mentioned above have a frequency higher than the human audible upper limit (20 kHz), in particular a frequency between 500 kHz and 25 MHz is typically used. The transducer then transforms the reflected sound signal back into an electrical signal which is represented on a screen that is read by a qualified operator.

3.1.1 Types of ultrasonic waves

Waves can be subdivided among mechanical and electromagnetic waves (EM), the former requiring a medium to propagate, the latter being able to propagate also in vacuum.

Ultrasound waves belong to the first family, with modes of vibration differing in the direction of propagation and in the movement of atoms. An ultrasonic wave can be defined as a mechanical vibration of the atoms of matter that propagates in a solid, liquid or gas, depending on the elastic properties of the medium, with a frequency of oscillation that is equal to:

$$c = f\lambda \tag{3.1}$$

Where:

- c is the ultrasonic velocity in the material, in $\left[\frac{m}{s}\right]$.
- f is the frequency of oscillation, in [Hz].
- λ is the wavelength, in [m].

Depending on the density and the elastic properties that change in various materials, the ultrasound waves travel through it with different velocities. There is also an influence of the way in which the ultrasound is generated, whether they are longitudinal (or compression), transverse (or shear), superficial waves, etc. [46]. Ultrasonic waves are classified as bulk waves and guided waves. The former can be longitudinal or transverse waves [47], that are predominant in ultrasonic NDT.

Longitudinal waves can propagate in all materials and are characterized by regions of compression and expansion. Their propagation occurs in the same direction of mechanical vibration of the atoms (figure 3.2a) and travels with a speed equal to:

$$c_L = \sqrt{\frac{E(1-\nu)}{\rho(1+\nu)(1-2\nu)}} \tag{3.2}$$

which depends not only on the elastic constants such as the Young's modulus, E, and density, ρ, but also on Poisson's ratio, ν. The temperature influences the velocity as well, more in liquids and gases, less in solids.

Transverse waves differ from longitudinal ones in some characteristics. In fact, the vibration of the atoms occurs at 90° with respect to the direction of propagation of the wave (figure 3.2b); moreover, since it is necessary for the particles to be rigidly bonded, they can't exist in gases and most liquids. Considering the same material, transverse wave propagates within it with about half the speed of a longitudinal wave:

$$c_S = \sqrt{\frac{E}{2\rho(1+\nu)}} \tag{3.3}$$

$$c_S = \sqrt{\frac{G}{\rho}} \tag{3.4}$$

In this case the shear modulus G is considered.

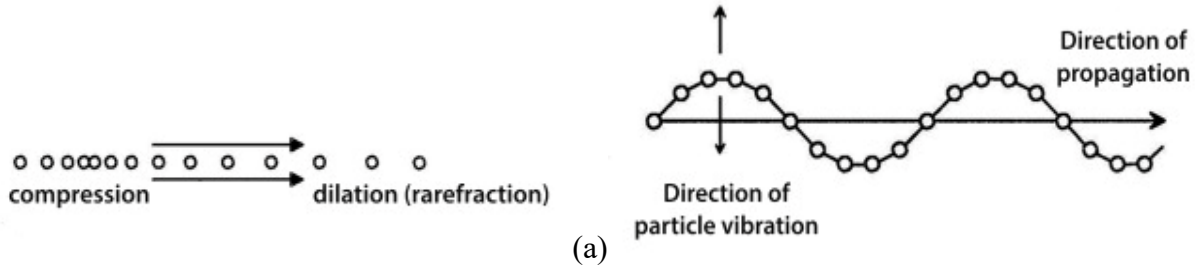

(a) (b)

Figure 3.2 Relative movement between vibration of atoms and propagation of a longitudinal (a) and transverse (b) wave

As far as guided waves are concerned, the most common in ultrasonic testing are surface (Rayleigh) and plate (Lamb) waves [48], that require a structure to guide them, like a surface or a plate.

Rayleigh waves penetrate the surface to a depth of about one wavelength, while the direction of the propagation is parallel to the surface, with particles that describe an elliptical motion with both the components, longitudinal and transverse. The velocity is around 90% of shear velocity in the same material:

$$c_R \approx 90\%\, c_S \tag{3.5}$$

When you have a thin plate and a surface wave is introduced into it, it is called Lamb wave, which can be symmetrical or asymmetrical depending on its displacement. Their velocity is calculated using the Rayleigh-Lamb frequency equations that is solved by numerical methods. As can be seen in Declercq [48], when it is a bounded beam that generates Lamb waves, the centre of the beam is the main part that generates such waves while the edge is more likely to generate Rayleigh waves.

3.1.2 Interactions and mode conversion

Bulk waves are employed to carry out the majority of the ultrasonic tests and sometimes certain conditions are exploited to convert longitudinal waves into transverse ones and vice versa.

In particular, when a wave encounters an interface, it interacts with it by being reflected, refracted or scattered, but mode conversion can also occur. Together with adsorption from the material, scattering is the main source of wave attenuation.

Scattering depends on the inhomogeneities that are crossed by the wave, such as cracks and voids as well as grain borders. They divert the wave from its original direction of propagation and the phenomenon is only negligible in case of small inhomogeneities (< 0.01 λ).

The absorption of the wave increases with the distance, x, it travels in the material according to the law:

$$I_x = I_0 e^{-\alpha x} \tag{3.6}$$

Where $\alpha = \alpha_A + \alpha_S$, includes the absorbed and scattered component.

The sound energy is converted into heat and therefore the initial intensity I_0 becomes I_x considering the attenuation coefficient α [Nepers/metre], that depends on the ultrasonic frequency. Variations of sound intensity are measured in decibels according to the logarithmic equation (3.7)

$$\Delta I(dB) = 10 \log_{10} \frac{I_2}{I_1} \tag{3.7}$$

Usually, however, the amplitude of the signal is measured instead of the intensity. In this case the difference in decibels will be given by the equation (3.8)

$$\Delta I(dB) = 20 \log_{10} \frac{A_2}{A_1} \tag{3.8}$$

where a ratio of 2 corresponds to a difference of 6 dB between the two signals and the amplitude doubles with each 6 dB increment.

While traveling through a medium, part of the wave is reflected, and part is refracted (wave transmitted with a different direction) when it encounters the boundary between two materials with an angle other than 90° and the materials have different indices of refraction. In addition, in this case of incidence not perpendicular to the interface, mode conversion may occur as mentioned above (figure 3.3), and often this mechanism is used specifically to convert a compression wave into a shear wave. In fact, these waves are particularly useful, for example, when mapping a material in search of defects with a different orientation.

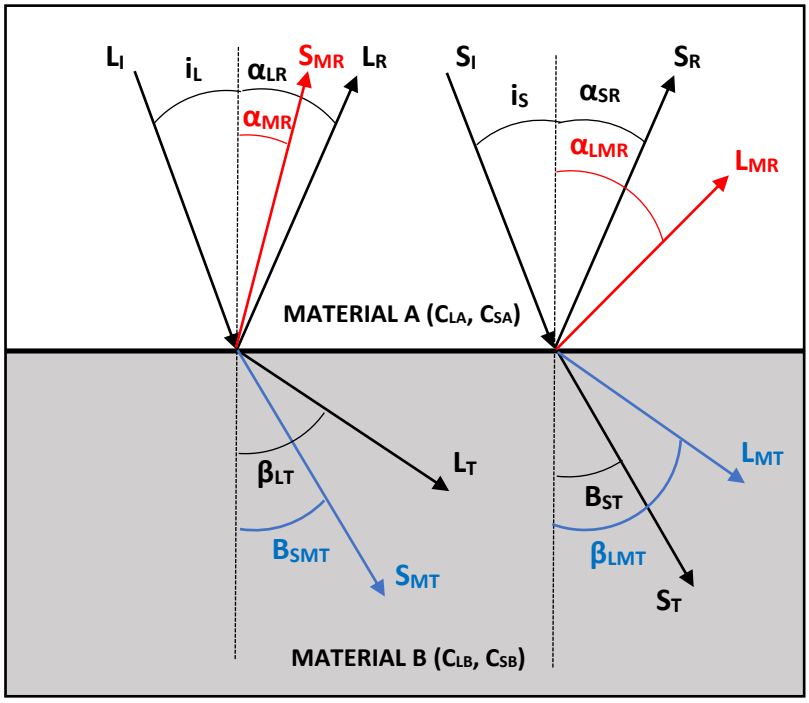

Figure 3.3 Mode conversion of longitudinal wave into a shear wave and vice versa

Referring to the figure above we have that:

- for an incident longitudinal wave L_I:

$$\frac{\sin i_L}{c_{LA}} = \frac{\sin \alpha_{SMR}}{c_{SA}} = \frac{\sin \alpha_{LR}}{c_{LA}} = \frac{\sin \beta_{LT}}{c_{LB}} = \frac{\sin \beta_{SMT}}{c_{SB}}$$

- for an incident shear wave S_I:

$$\frac{\sin i_S}{c_{SA}} = \frac{\sin \alpha_{LMR}}{c_{LA}} = \frac{\sin \alpha_{SR}}{c_{SA}} = \frac{\sin \beta_{ST}}{c_{SB}} = \frac{\sin \beta_{LMT}}{c_{LB}}$$

The parameter that determines the amount of reflected and refracted energy, through an interface between two different materials, is the acoustic impedance Z [$kgm^{-2}s^{-1}$] or [Rayl]:

$$Z = \rho c \tag{3.9}$$

where

- ρ is the mass density [kgm^{-3}],
- c is the ultrasonic velocity [ms^{-1}].

Reflection and refraction are two sides of the same coin, in fact the amount of energy that characterizes the two waves is a fraction of the incident one. In the case of normal incidence, the transmitted and reflected intensity of the wave are described by equations (3.10 and 3.11)

$$T = \frac{4Z_1Z_2}{(Z_1+Z_2)^2} \times 100\% \tag{3.10}$$

$$R = \left(\frac{Z_1-Z_2}{Z_1+Z_2}\right)^2 \times 100\% \tag{3.11}$$

The higher the impedance mismatch, the higher the percentage of energy reflected at the interface.

What causes refraction is the variation of wave propagation speed inside the two materials, which also depends on the refractive index 'n'

$$n = \frac{c}{v} \tag{3.12}$$

This expresses the ratio between the speed of sound in vacuum and that in the material considered. In figure 3.4, a wave crossing an interface between two materials with different impedance is represented.

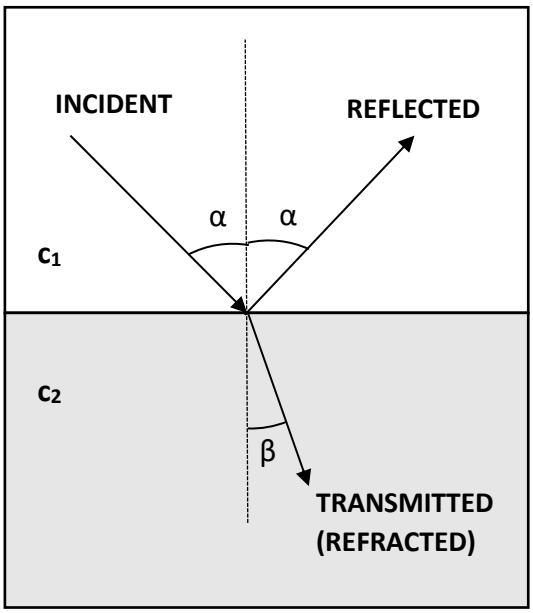

Figure 3.4. Wave reflection and transmission at the interface between 2 different materials

So, a wave traveling in a medium with a lower refractive index will do so at a higher speed, while if the refractive index is greater, the speed will be correspondingly lower [49].

A wave incident at a certain angle α will be reflected at the same angle because the wave is traveling in the same material, and transmitted at a different one β. Snell's law describes the relation between angles and wave velocity, and it is equally appropriate for longitudinal and shear waves

$$\frac{\sin\alpha}{\sin\beta} = \frac{c_{L1}}{c_{L2}} = \frac{n_2}{n_1} \tag{3.13}$$

c_{L1} and c_{L2} are the longitudinal wave velocity in material 1 and 2 respectively.

In the case of a ray passing from a denser medium (lower velocity and higher n) to a less dense one (higher velocity and lower n), as the angle of incidence α increases, the angle of refraction β in the second medium increases. This is until the critical angle α_{CR} is reached, where the wave will be refracted parallel to the interface between the two mediums (β=90°). For each incident angle higher than the critical one, the phenomenon of total internal reflection occurs, and the sound is not able to enter. This typical angle differs between longitudinal and shear waves and therefore there will be different velocities in the same material.

A sound wave can also be diffracted in case it encounters an obstacle along its path that redistributes its intensity in space and bend the wavefront. In case a plane wave meets a barrier with a slit, this is crossed and its edges act as sources of new waves, with a spherical wavefront, radiating energy in different directions (figure 3.5).

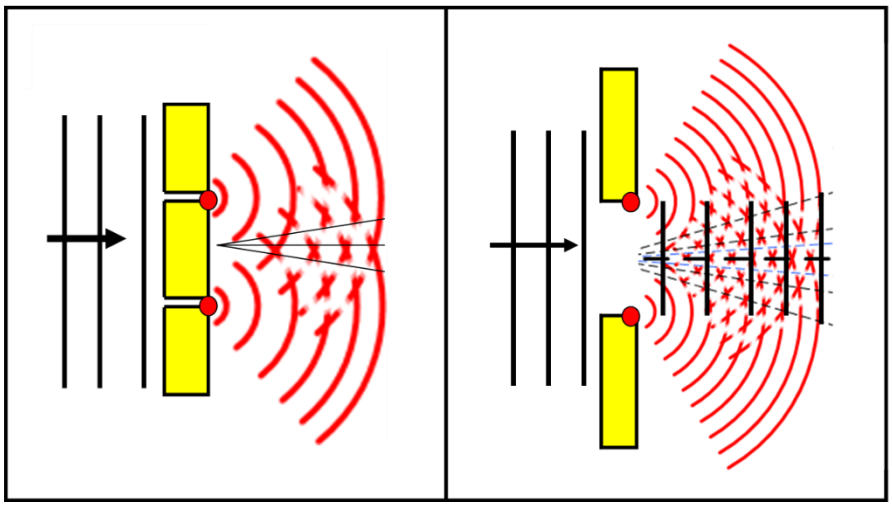

Figure 3.5 Diffraction of a wave passing through slits [50]

In an ultrasonic transducer, which will be described in the next paragraph, the same phenomenon occurs. The transducer usually has a circular shape that produces a plane wave (similar to a circular slit), while its edges yield spherical wavefronts that overlap with each other and with the plane wave, resulting in constructive and destructive interference and disturbing the signal near the transducer. In this region, called the near-field, it is therefore hard to detect the presence of any defects. In the case of a transducer with diameter D at wavelength λ, the length of the near-field N can be calculated with the formula:

$$N = \frac{D^2}{4\lambda} \tag{3.14}$$

The area beyond N is called far-field; there, a uniform beam is encountered that has reached its maximum intensity and therefore allows an easier identification of defects present in the area [51]. This is the most suitable region for NDT.

Another consequence of diffraction is that the ultrasonic beam diverges away from the circular transducer (figure 3.6). This phenomenon is known as beam spread. The divergence angle (half of

the spread angle) can be calculated as a function of the diameter D and the wavelength λ of the transducer, and the velocity of the beam in the medium as:

$$sin\theta = 1.2\frac{\lambda}{D} \tag{3.15}$$

$$or$$

$$sin\theta = 1.2\frac{V}{Df} \tag{3.16}$$

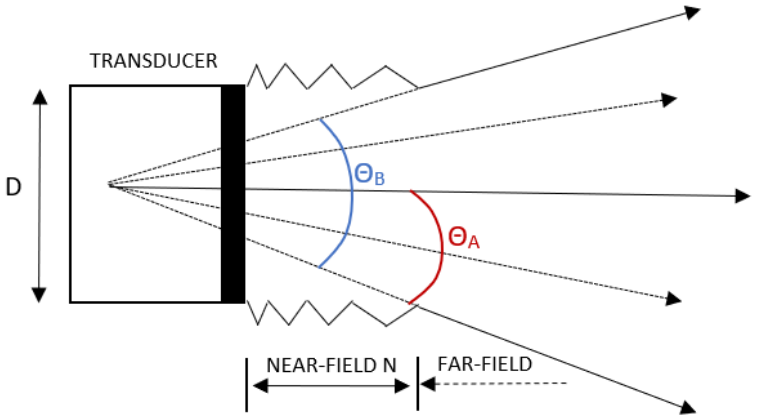

Figure 3.6 Divergence of an outgoing wave beam from a transducer

It is evident that at equal frequency, a large transducer diameter will have a narrow beam, while as the diameter decreases the transducer beam widens. By fixing the diameter instead, a narrower beam is obtained by increasing the frequency. This consequently possesses more energy and hitting a defect makes it more visible as the echo will be more intense.

3.2 Equipment

The instrumentation commonly includes [52]:

- Power supply: provides power supply to all the parts via a cable or in the case of a portable device by means of a battery.
- Pulser/Receiver and Amplifier: pulser/receiver produces high voltage electrical pulses at rates of up to 1000 Hz that are applied to a transmitter probe that generates a mechanical vibration. The reflected signal is then amplified, after reception and conversion back into an electrical signal, and displayed on the screen.
- Transducer (or probe): it converts one form of energy into another. In the specific case of an ultrasonic transducer, the electrical energy is converted into ultrasonic energy by exploiting the piezoelectric effect and the inverse piezoelectric effect. In fact, the transducer contains a piezoelectric element capable of producing electric charges on its surface when it is deformed by an external pressure. The reverse piezoelectric effect is obtained instead when a piezoelectric material is placed between two electrodes to which an electrical field is applied causing the deformation of the material, phenomenon of electrostriction. The element usually is a thin flat circular disk whose thickness t depends on the desired frequency. It vibrates at the first fundamental resonance frequency f_0 with a wavelength that is twice the thickness t:

$$f_0 = \frac{c}{2t} \quad (3.17) \qquad\qquad t = \frac{\lambda_0}{2} \quad (3.18)$$

where c is the speed of sound in the piezoelectric.

It can be seen that the higher the frequency, the thinner the element and this is the reason why it is difficult to fabricate high-frequency elements. What determines the mode of vibration is the direction in which the piezoelectric crystal is cut. If this is done in such a way that the wide face of the cut element is on the x-axis, this will result in compression waves with longitudinal vibration. If, on the other hand, the wide face of the cut element is on the y axis, shear waves with transverse vibrations will occur.

At the same time, it is necessary to consider the attenuation of the energy of the wave when it crosses the interface between two media. In order that as much energy as possible enters the sample, the matching layer is used, a layer coupled to the element, which is 1/4 the thickness of the desired wavelength and allows efficiency to be maximised.

The frequency is also linked to sensitivity and resolution. To achieve good sensitivity and resolution, a high frequency is used, which involves at the same time a high attenuation and therefore a low penetration. On the other hand, with a low frequency the attenuation will be less and the penetration deeper, but sensitivity and resolution are less.

To ensure that there is no disturbance in the probe, a backing with similar impedance is placed in it, with absorbing and damping capabilities.

The following figure 3.7 shows the scheme of a piezoelectric transducer with various components and the details of the matching layer.

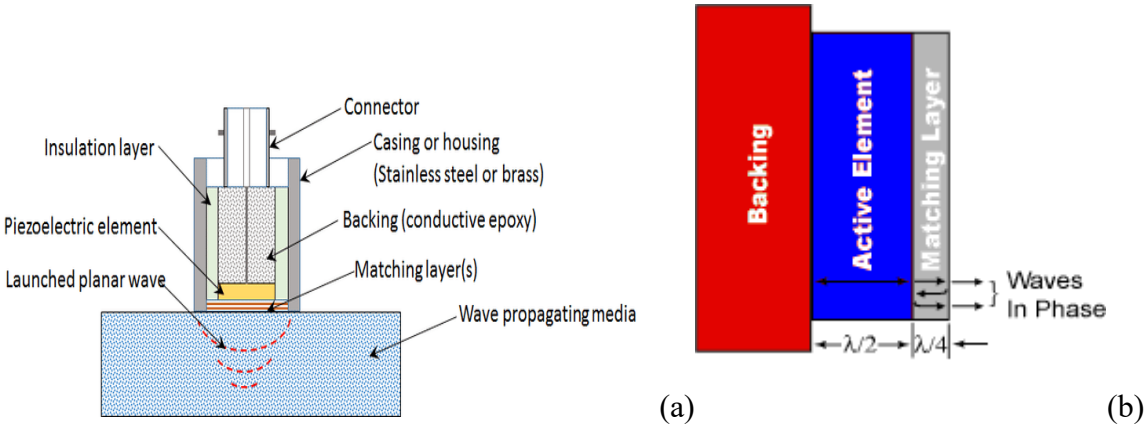

Figure 3.7 (a) Scheme of a piezoelectric transducer [53]

(b) Thickness of active element and Matching Layer [51]

- Couplant: due to the rough surface of the sample to be tested, when the probe is placed on it, micro air pockets are created between the two surfaces and almost all the energy is reflected

reducing the amount transmitted. This is due to the large difference in acoustic impedance between air and solids [51]. Therefore, a layer of couplant is utilised between the transducer face and the component surface, ensuring good contact and an efficient transfer of ultrasonic energy. In contact ultrasonic testing the couplant is usually in liquid form e could be glycerin, oil, grease or water, especially in the immersion ultrasonic testing. The selection also depends on the surface finish and the temperature of the sample on which it is deposited [46].

The requirements are:

- Acoustic impedance between that of the probe face and of the sample.
- Non-toxic.
- Non-corrosive.
- Cheap.
- Easily removable at the end of the inspection.

- Display and timer: a display gives the possibility to represent the received signal so that it can be examined by an operator. While the pulse is applied to the probe, the display is started and synchronized by means of a time base generator. The speed at which the pulses are emitted, pulse repetition frequency (PRF), range from 100 Hz to 1 kHz.

3.2.1 Types of probes

Depending on the material examined and the defects investigated, probes may be used that differ in size, frequency, and angles, and thus the ultrasonic testing methods can be divided according to the types of probes and their configuration [54] as follows.

- Pulse echo: to describe the basic principles of ultrasonic analysis, in paragraph §3.1 reference was made to the simplest configuration of the probe, the pulse-echo. A single

transducer is used with the dual function of transmitter and receiver of the waves that are reflected. By measuring the time taken by the wave to travel from the transducer to the back wall or to the defect and then go back, it is possible to measure the thickness of the sample or locate the depth of the defect. In figure 3.8 is showed a schematic set-up of pulse-echo testing at normal incidence of the waves. If wave velocity is c and the thickness of the sample is h, then the ultrasound is reflected from the back-wall after t=2h/c (probe A) or t=2d/c in the event that it is reflected by a defect (probe C). In the case B, the probe is only partially over the defect and the reflected signal by the back-wall has a reduced amplitude. As you can see a vertical defect D may not be detected.

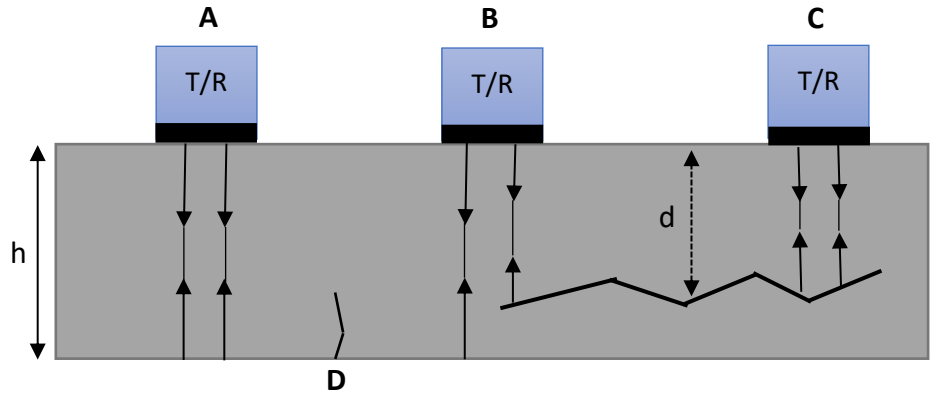

Figure 3.8 Pulse/Echo transmitter 0° compression probes, (A) without defect, (B-C) with defect

A disadvantage of the single probe is the presence at the surface of the so-called dead zone, where it is unable to receive signal and thus find defects since it continues to emit signal while the reflected one tries to enter the probe. The solution involves the use of twin-element probes, that is, two piezoelectric elements, a transmitter and a receiver, inserted into a probe, separated by an insulating material. This eliminates the presence of the dead zone and allows surface defects to be detected.

- Through transmission: in this case, two separate transducers, one transmitter and one receiver are placed on opposite sides of the sample being tested. So, the signal passes through the material only once. Looking at figure 3.9, in case A the signal travels through a single thickness in t=h/c, in case B part of the signal is blocked by the crack and part reaches the receiver with lower amplitude, in case C the ultrasound is totally blocked by defect and does not reach the receiver on the other side. In the latter case, care must be taken not to confuse it with a poor coupling between probe and sample. As in the previous case a defect D not perpendicular to the ultrasonic waves may not be detected.

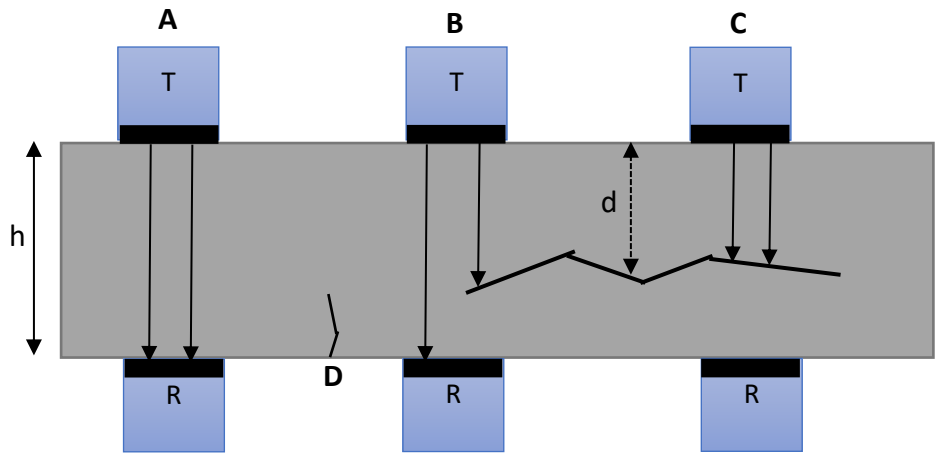

Figure 3.9 Through transmission probe configuration

In this configuration, it is required to access both sides of the material and it is not possible to detect the depth of the defect, but it is particularly good in different circumstances. Testing of highly attenuating materials is possible, like porous materials, and thick components, thanks to a lower divergence and scattering of the waves due to a single crossing of the thickness. Furthermore, this is even an advantage to evaluate dissimilar metal joints. In their presence, the signal is reflected acting as a noise that can also suppress the signal near the joint, but in

through transmission no interference is noted between signals at the interface as only the transmitted wave is acquired [55].

- Resonance: it is similar to pulse echo, and it is mainly used when only one side of the material is accessible. The same term, acoustic emission (AE), is used for describing the technique as well as the phenomenon [56]. When inside a material there is a rapid release of strain energy from a source, this generates acoustic emissions, that are elastic waves in the ultrasonic frequency regime. These sources are events within the body and can be mechanical deformations and fractures, but also phase transformations, corrosion and friction [57], and it is not always easy to understand what the generation mechanism is.
  In fact, AE is a passive test method, in the sense that a direct excitation is not applied. In general, the phenomenon occurs when the stress field or deformation are varied; the waves propagate to the boundaries where there are sensors attached, and an eventual weak electrical signal coming from the transducer is amplified and displayed. The transducer, like in the previous technologies, has a high sensitivity and is usually made of piezoceramic or piezocomposite, and it may be either undamped (to highlight sensitivity at the frequency of resonance and minimise the background noise at the others) or broadband (to get additional information). The AE apparatus (figure 3.10) also includes the amplifiers, that are recommended in order to reduce the noise, and high pass filters (20-30 kHz).

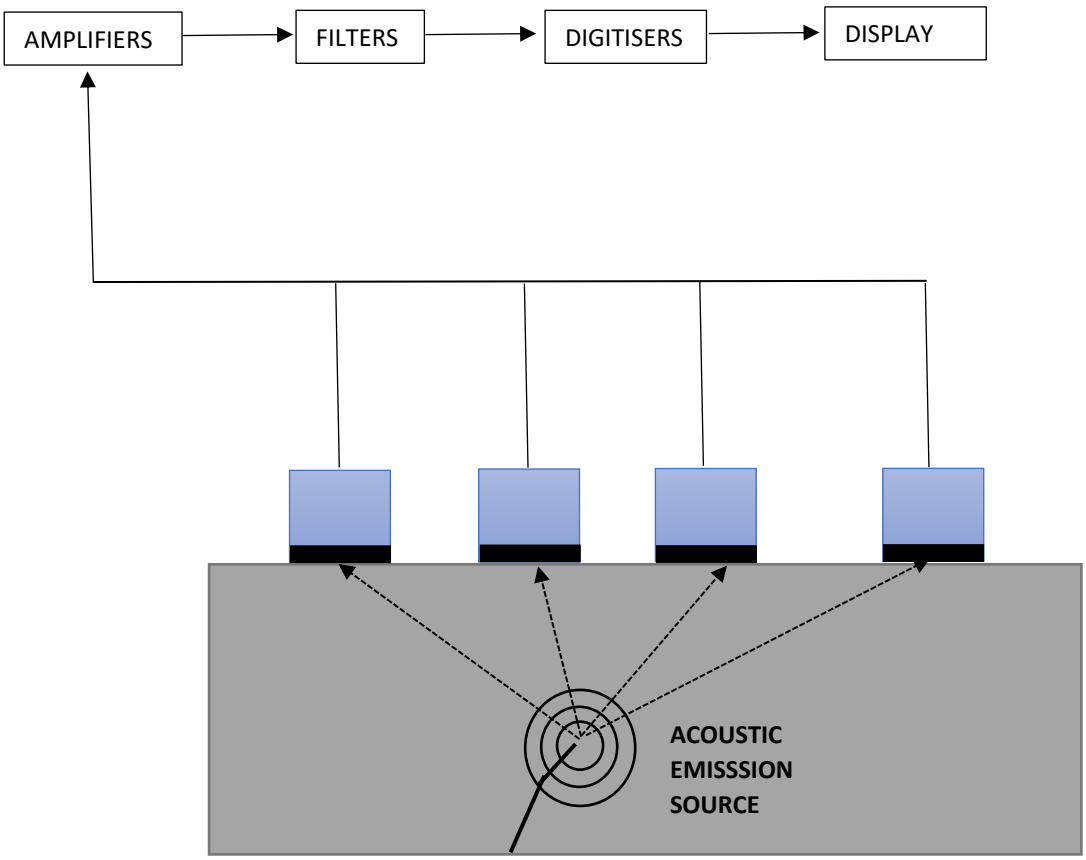

Figure 3.10 Schematic representation of AE apparatus

All the advantages of AE described here are exploited for structural testing, process monitoring and check, materials characterisation and testing [56].

More particularly, the acoustic emission techniques are mainly used in three modes:

- to locate the source of the AE by using several receivers.
- to determine each variation in rate of AE, which may be linked to the generation of new defects or to their increase in size.
- to establish the residual safe life of a component.

As AE testing methods are non-localised, it is possible to inspect large regions or entire structures, like bridges or pressure vessels, through multiple sensors positioned on the entire

surface. The main difficulties could be measuring with adequate accuracy how much the arrival times of the same pulse differ at two different points and identifying the same event once it has been attenuated and distorted by crossing the structure in different directions.

3.2.2 Other probe types

- Angle probe: As previously mentioned, it can happen that a defect not perpendicular to the ultrasound beam is not detected. For this reason, ultrasounds are emitted within the sample at a certain angle, producing surface and shear waves by mode conversion of a longitudinal wave in a Perspex wedge (figure 3.11). To prevent interference effects with the received signal, since reflected waves will be present in the wedge, the wedge needs to be angled and damped.

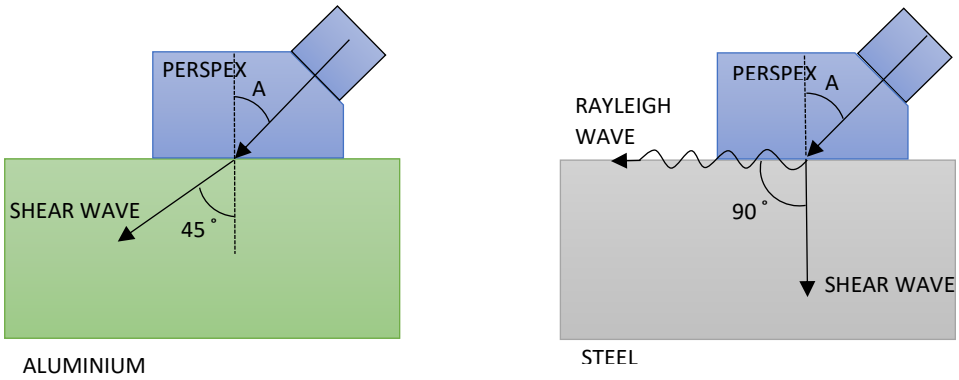

Figure 3.11 Angled probes producing shear and surface waves

It is possible to calculate the wedge angle A and the sample thickness t, in case shear or surface waves are produced as in figure 3.11 by knowing the wave propagation velocities in the materials and applying Snell's law, under the given frequency conditions. In case no defects are present in the sample or because a poor coupling of the probe with the sample

there may be no signal, then on top of the angled probe is positioned a second compression wave probe at normal incidence that will collect the echo from the backwall of the sample. Especially this slanted configuration is very useful in the noncontact ultrasonic analysis technique as it offers increased acoustic coupling with solids due to the conversion of acoustic modes [58]. Recently, progress has also been made on the analysis of defects, to classify and size them by ultrasonic guide waves [59].

- Immersion probe: The problem of variable couplant layers can be avoided by entirely submerging the sample in a tank filled with a liquid (water or oil) (figure 3.12).

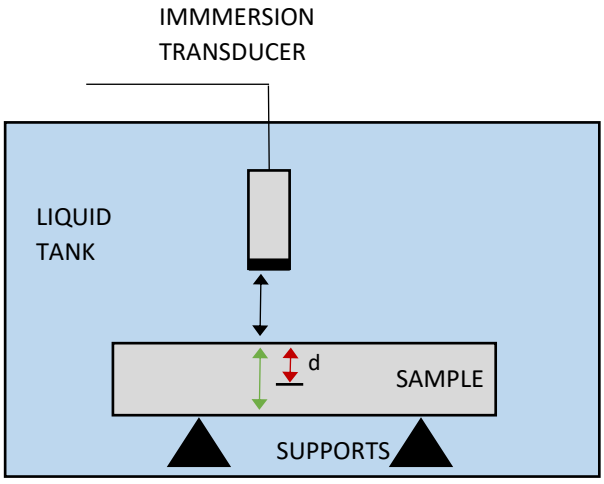

Figure 3.12 Immersion probe configuration

There is impedance mismatch between the PZT of the probe and the water, and to reduce it, a layer of epoxy is usually applied on the probe. One benefit of this technique is that it requires no contact between probe and sample, so rapid inspection is possible. On the other hand, it is not suitable for wide components or porous and absorbent materials. The signal received by the pulse-echo transducer in an immersion system consists of several echoes. To prevent multiple echoes to be reflected from the front surface before the first reflection from the back wall, the length of the water column is fixed with respect to the thickness of the

material under test. Restriction that does not occur in the through-transmission technique. [55]. A variant of this technique is the so-called pool technique, where the sample to be tested is only partially submerged in the liquid and the immersion probes are turned toward it from inside the liquid. This is useful in the case of cylindrical samples that can be rotated for full inspection.

- Focus probe: Focused ultrasound allows energy to be concentrated at the focal point. The region with higher sensitivity is called focal zone; these types of probes allow for an increase in sensitivity due to the shortening of the near-field distance. The focalised probes are manufactured to produce a certain focal length in a specific material, and the focus can be a point, spherical focus, or a line, cylindrical focus. The manufacture of a focused transducer is influenced by several factors such as the power to be supported, the frequencies, and the material of construction [60]. They are used to produce high resolution images, in particular a smaller beam and a higher lateral solution.

3.3 Data presentation

There are various ways to represent the ultrasonic signals that are picked up by the probes, each has a different way of viewing the inspected region. The three most common types are known as A-Scan, B-Scan and C-Scan and are chosen according to the characteristics of the instrumentation and the information you are interested in obtaining from the data.

A-scan is the standard way to represent the signal received by the probe, displaying the amplitude of the signal on the y-axis as a function of the elapsed time, x-axis (figure 3.13a,3.13b). The position of the discontinuity placed in front of the probe is thus localized. By measuring the distance between the peaks on the graph, the location of the defects can be identified. Moreover, the operator can determine the size of the flaws, as the amplitude is an evaluation of the quantity of

ultrasonic energy reflected to the receiver, by comparing the amplitude of the signal from an unknown source with that from a known one [51]. If the speed of the wave in the material is noted, it is possible to represent directly the depth of the defect on the horizontal axis.

Referring to the configurations of figure 3.8 and figure 3.9, paragraph §3.2.1, the A-scan representations are shown in figure 3.13a and 3.13b. Consider the pulse-echo configuration of figure 3.8 and its representation in figure 3.13a. When the probe is then moved along the surface, other signals appear on the screen in a different position on the time axis. The initial pulse of the transducer is represented close to time zero and record the energy of the initial pulse. Together with this, in case A, a peak corresponding to the wave reflected from the back wall is represented that will not have the same energy as the first pulse, because in part it is absorbed by the test object. In the position B of the probe, the signal partially encounters a defect, so a spike due to the defect and one to the back wall appear respectively. The latter is of smaller amplitude than in case A, as part of the energy has been reflected by the defect. When it is in the far-right position, C, the probe is completely on the defect, so only the peak relative to it appears, with greater amplitude than case B. Some attention must be paid in case C of figure 3.13b, through-transmission configuration, since it could be confused with a poor coupling between probe and coupling in the ultrasonic test with contact.

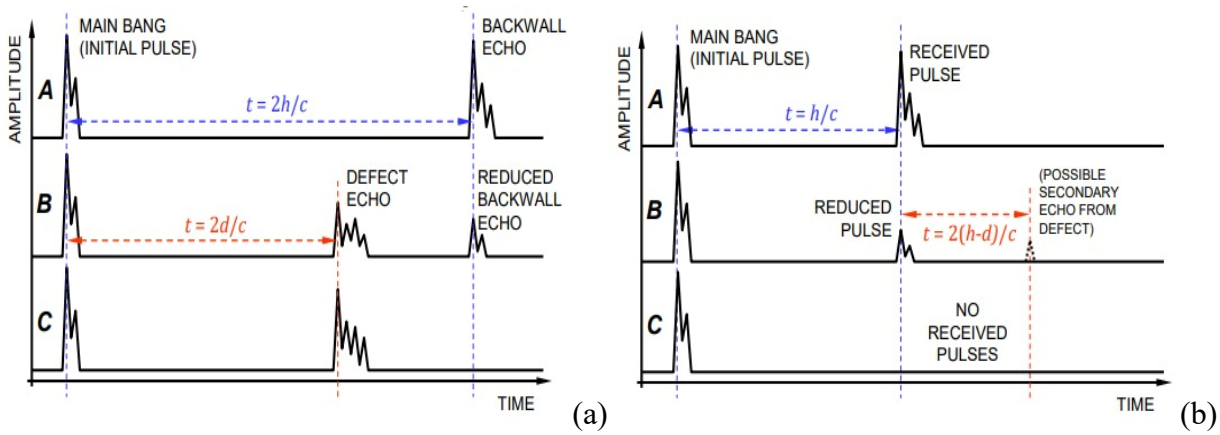

Figure 3.13 A-scans of pulse echo (a) and through transmission (b) configurations

B-scan representation is more appropriate for large components and to acquire two-dimensional information of the defect. It is obtained by mapping the surface of the tested object (figure 3.14a) with multiple A-scans that combined create a view of the component's cross-section. In this case, the travel time of the wave or the flaw depth is displayed along the y-axis, while along the x-axis the position of the probe is indicated (figure 3.14b). In case of large discontinuities, it is possible to evidence the form and orientation to some extent [46]. Figure 3.14b illustrates the lines B and C of length similar to that of the defects and at their depth in the material. The IP and BW lines are the signals from the initial pulse and coming from the back wall. To obtain much more information a grey or colour-scales is feasible to use, corresponding to different amplitudes.

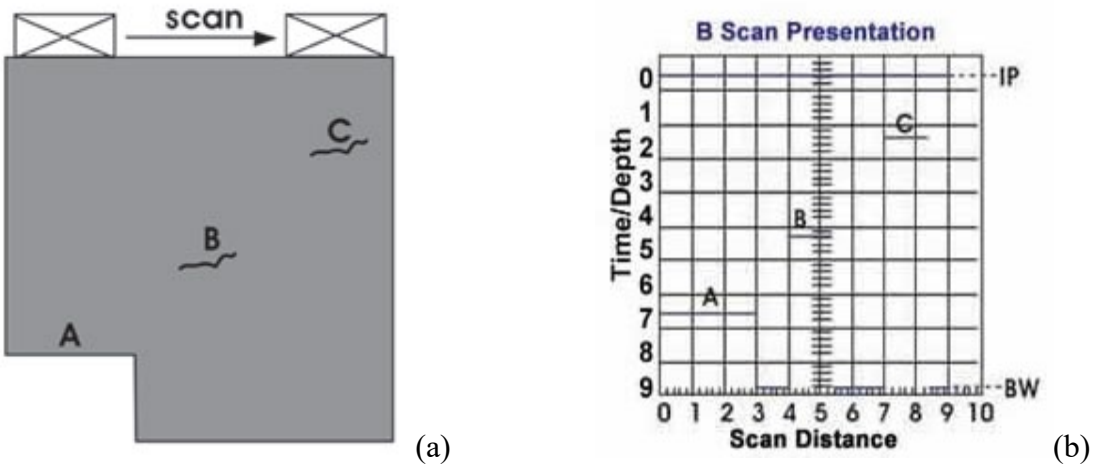

Figure 3.14 (a) probe moved along the sample surface; (b) B-scan presentation

C-scan presentations are generated by an automatic data acquisition system, providing a flat view of the component, and the position and size of the features within it [51]. A software produces a waveform output of the C-scan after the scanning of the sample and a data file with a C-scan picture with the pixel of different colours [61]. The quality of the final image created depend on the size of the transducer. A raster scanning is used by moving it on the surface to be examined and at each point an A-scan is recorded, which corresponds to a pixel in the final image of the C-scan (figure

3.15). A specific depth can be selected using a corresponding window within the A-scan, and depending on the relative amplitude of the signal, each pixel in C-scan will have a different colour. This mode of representation is particularly used with automated immersion system, and it is also appropriate with through-transmission systems [46].

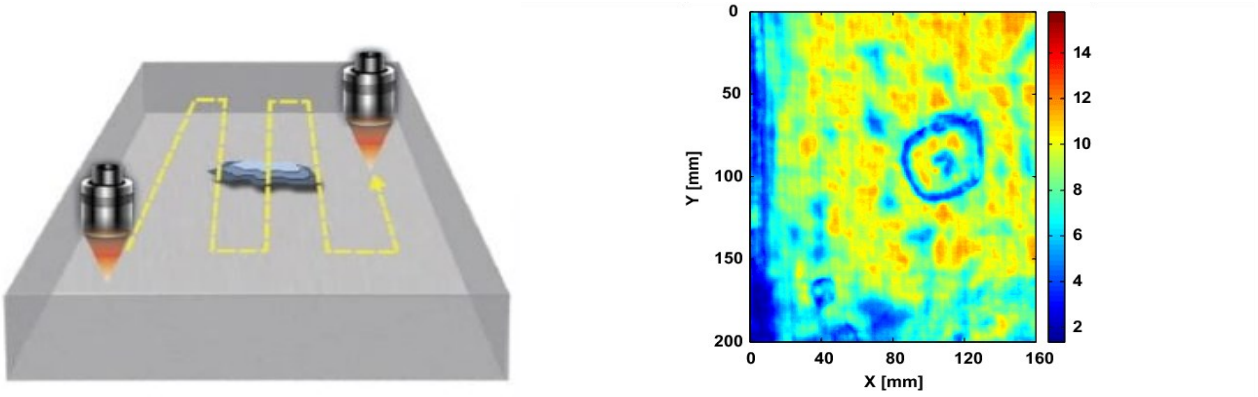

Figure 3.15 The transducer is scanned over the test piece (left) [62].

Final image of C-scan with coloured pixel (right) [63].

3.4 Advantages and disadvantages

Ultrasonic testing is broadly employed, from the industrial sector, such as the automotive industry, to the medical applications, as it offers several advantages over other techniques. In fact, ultrasonic testing can be used on a wide variety of materials, requiring little or no preparation of the sample to be tested and it is less time consuming. From the point of view of safety, it does not affect the specimen nor the safety of the operator who performs the test, so it is safe and not harmful; moreover, it is cheaper than other methods [64]. Thanks to a deep penetration of ultrasound into the materials it is possible to scan the entire volume and find internal and surface defects. The position and size of these defects are localized, as well as their nature, shape and orientation. In metals, with

the ultrasonic technique it is also possible to evaluate microstructural differences measuring attenuation, velocity and backscatter. Comparing the decay pattern of the specimen with that of the standard, information about the microstructure can be obtained: for example, if the sample has a lower decay pattern, then its microstructure is coarser [46]. In case a component needs to be examined in situ and it is difficult to access both sides to install two probes, the pulse-echo technique allows to perform the test by accessing only one end of the part.

However, as in any technique, there are also limitations, such as the need for a qualified operator able to interpret the resulting signal represented on the screen. Then the structure of the part being tested is important. If it has a rough surface or an irregular shape it is difficult to test as well as if it is very small or too thin. What is of particular interest here is the way in which the ultrasounds enter the material to be tested. In the previous paragraphs we referred to the use of a layer of couplant between the probe and the surface of the sample or to the immersion technique. When a couplant is used, it is hard to control its thickness and the homogeneity especially when the probe is moved on the surface of the sample during the test [65]. In substance it is necessary that there is physical contact that allows a good transmission of the wave from the transducer into the object under examination. However, not all materials are suitable for contact with a liquid, and this prevents their inspection. In the immersion technique, water is often used, which makes difficult the examination of materials such as paper, metals and porous materials. Similarly, contact ultrasound analysis is limited by the use of couplant as this reduces the simplicity and velocity of scanning and also can be absorbed, damaging those substances that are adverse to it [66].

Chapter 4

Ultrasound without contact

The inspection through ultrasound without contact, also known as air-coupled ultrasonic inspection, it is defined as such because the coupling medium (air or another gas) does not require further physical contact but is part of the environment.

Advantages and disadvantages of traditional ultrasound analysis have just been outlined in section §3.4. Particular attention has been paid to the limitations induced by the need of contact between the probe and the object to be tested. This led to the necessity of developing a different solution that allows to perform an analysis without contact. This kind of method is becoming more and more important and widely used. It is mainly employed during the production chain to control the process as well as to test complex materials such as composites and honeycomb structures. This is possible thanks to the continuous evolution in transducer technology and electronics, and innovative analysis algorithms [67]. This evolution of transducers stems directly from the attempt to cope with the large difference in acoustic impedance that exists between air and solid matter.

4.1 Physical principles

The operation of this technique can be explained by referring to Figure 4.1. Here the through-transmission method is considered, so a transmitter and a receiver are used. These two transducers are placed on opposite sides of the sample, at a distance from it of L1 and L2, respectively, and spaced L apart.

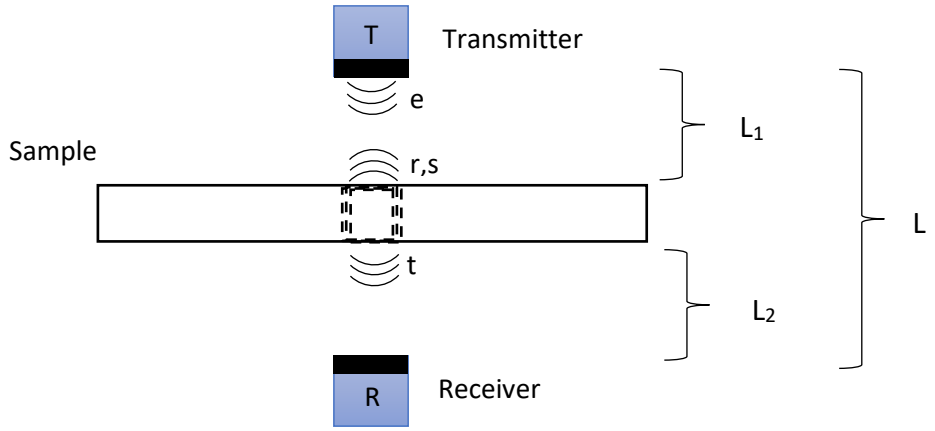

Figure 4.1 Air-coupled probes in through-transmission configuration

The waves emitted (waves e) by the transmitter travel through the air towards the surface of the sample and, because of the great incompatibility of acoustic impedance between air and solid, most are reflected back to the source (waves r) [68]. Part of the energy penetrates into the material and within it the waves travel with a greater speed than in the air and interact with any defects or boundaries being scattered and reflected. The waves produced are transmitted towards the receiver (t-waves) and towards the source (s-waves). Facing the front surface of the sample, the s-waves overlap with the r-waves, and since the s-waves are many orders of magnitude smaller, they do not allow the pulse-echo technique to be adopted to collect information about the sample. The characterization of the sample here is instead possible since the transmitted t-waves propagate themselves towards the receiver. The wave leaving the sample and traveling through the air to the receiver takes a certain time and is characterized by a certain frequency. This information is related to the thickness of the plate and the speed of the wave, which are useful for the characterization of materials [63]. Interestingly, there is an increase in the amplitude of the transmitted waves when the resonance frequency of the sample is matched to the frequency of the incident wave [63,64]. What happens is an increase in the transmission coefficient, this seen in equation (3.10) can also be defined as the ratio of transmitted energy to incident energy. This improvement, which occurs at a certain frequency, makes it possible to analyse material properties and geometry (such as thickness,

density and modulus of elasticity) whose variations influence the frequency spectrum of the transmitted wave [66]. The superposition of the waves trapped in the material creates instead a high resonance that, depending on the geometry of the ultrasonic field and the air cavities, is exploited especially in materials with high impedance to increase the energy transmitted through the plates [65].

4.2 Benefits and applications

Whenever conventional techniques cannot be used, the use of air-coupled ultrasound presents itself as an excellent non-destructive material characterisation technique. This avoids the need for immersion techniques in water or a coupling medium, which have been seen before, particularly for materials with porous structures or water-soluble. Sometimes the coupling fluid can also result in contamination of the material and change its structure. Other benefits of this technique include the possibility of saving water, time and therefore production costs while saving energy usage [72]. This is also linked to the absence of coupling agents, a sustainability factor on which industries rely during quality control [64, 69, 73]. Furthermore, in addition to single-sided access to the component, neither an immersion container (immersion technology) nor a radiation shield (x-ray technique) is required. The need to apply pressure to the probe is also eliminated, resulting in no fluctuations in signal amplitude or damage to the component surface [74]. Overall, the ease and speed of execution of the test are improved. The pulse-echo method is useful when the roughness of the surface is to be investigated, less in the case of the inner volume of a solid for the reason mentioned earlier about the echoes of the rear and front surface superimposed. This method is therefore generally applied in distance measurement, like parking assistant, instead of component testing, in which the transmission method is preferred, for instance for the ultrasonic characterisation of multi-layer bonded structures as has been demonstrated by Schindel [66]. Non-contact ultrasound is also used in manufacturing processes because it can provide more accurate

information regarding the fabricated parts. Especially, regarding two important aspects: proximity sensing and gauging, the first aims to guide the process, the other to accurately control the size of objects [75].

4.3 Acoustic impedance mismatching

As mentioned above, in air-coupled ultrasound, the main obstacle is the large acoustic impedance difference at the air-solid material interface. This means that only a small part of the energy is transmitted (T≈0) and most of it is reflected (R≈1) (figure 4.2), resulting in faint signal-to-noise ratio (SNR) values and short amplitude of the transmitted signal. Losses occur both as the signal from the air enters the medium and as it leaves the medium to continue outside. Furthermore, due to the difference in the speed of propagation of sound in air and in solid material, the signal also undergoes refraction at the interface [72].

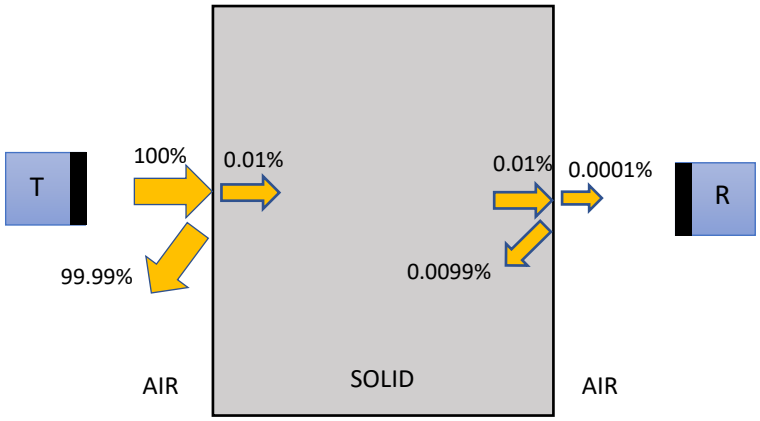

Figure 4.2 solid material in air present two solid-air interface

A way to increase the transmission efficiency is to have a thin solid layer as a sample compared with the wavelength, and in particular its thickness should be a small integer number of half wavelength thick, $d = n\frac{\lambda}{2}$, (n=1,2,3...) [76], as this creates constructive interference inside the layer

that makes it resonate. In essence the solid layer acts as a narrow band pass filter. Minimum transmission occurs instead, when the thickness of the sample is an odd integer multiple of a quarter of the wavelength $d = n\frac{\lambda}{4}$, (n=1,3,5...).

It should then be added that in the high-frequency range there is a large attenuation coefficient in air, which limits the air-coupled technique to frequencies below about 2 MHz [66]. A signal with an intensity in the range of 1MHz-2MHz can propagate for a few centimetres. In fact, since the intensity of the signal decreases with the distance covered, the amplitude of the signal is reduced to 1/e from its initial amount, in correspondence of a space that is inversely proportional to the square of the frequency of the sound [64]. This space is known as the extinction distance. In general, transducers working in different frequency ranges are used depending on the application. If they are in direct contact with the solid or liquid, waves in the MHz range are produced, if they transmit through the air, they are preferred in the kHz range [77]. However, as shown in section 4.4, new developments make it possible to go beyond this limit in the case of transmission in air.

The temperature of the air and the humidity in it affect the absorption coefficient as is possible to see from Figure 4.3 where the absorption coefficient [m^{-1}] is represented as a function of the ratio of frequency [Hz] to air pressure [Atmos], at a defined temperature. It is good to note that for a fixed pressure, as the frequency increases, the absorption increases [75]. Since the speed of ultrasound waves is affected by temperature variation, an increase in temperature causes the sound to travel faster, and in a distance measurement the target may appear closer to the sensor than it actually is [78].

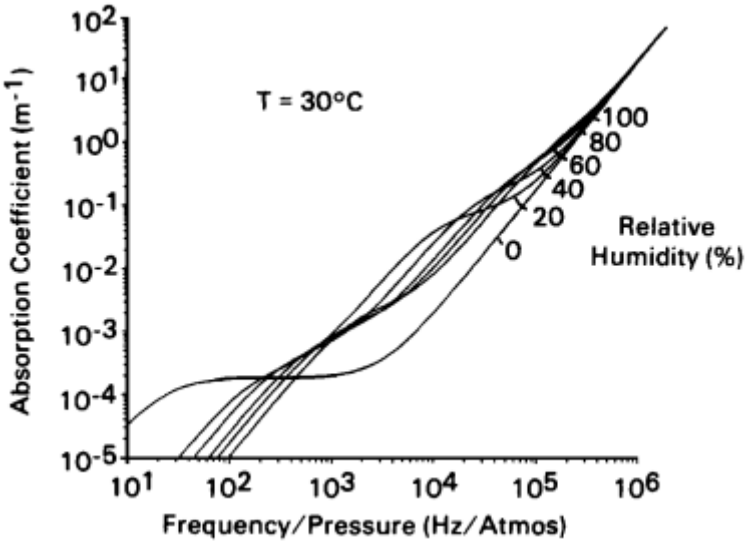

Figure 4.3 Trend in absorption coefficient as a function of frequency/pressure ratio at a temperature of 30 °C

4.4 The transducers

Despite these problems and the initial belief that there was no energy transfer between air and solid matter due to the high acoustic impedance difference, it is now possible to perform material characterization using non-contact ultrasonic probes thanks to the continuous improvement of transducers, electronics and signal processing. In fact, to make possible an analysis without contact, the main focus of the last years has been to improve the sensitivity of the transducers.

The new types of probes developed include mainly two types of transducers: piezo-transducers where to increase the ultrasonic transmission in air, a series of layers are added to the piezoelectric element, and capacitive ones that contain a vibrating membrane [64].

Traditional piezoelectric transducers do not work properly in air, in fact part of the energy remains confined in the piezoelectric element. These possessed on their face a layer of material λ/4 thick of the frequency of interest, with intermediate impedance between that of air and PZT given by

$$Z_{LAYER} = \sqrt{Z_{PZT}^2 + Z_{AIR}^2}\ , (4.1)$$

to minimize transmission losses.

This layer of material can be made of silicon rubber or silica aerogel, a material consisting of silica microspheres pressed together maintaining high porosity within the particles; it offers good impedance but at the same time high ultrasound attenuation. The difficulty in designing piezoelectric transducers lies in having a low sensitivity and narrow bandwidth [79] due to the high impedance mismatch with air. Using only one coupling layer improves sensitivity but more than one is required to widen the bandwidth [79]. A possible solution is to place an extreme layer of material with low impedance, attenuation and a thickness suitable for the working frequency, and other intermediates with properties that improve bandwidth without affecting sensitivity [80].

Recently, therefore, transducers have been developed with multiple layers of decreasing impedance and a final critical matching layer (Figure 4.4). These narrow bandwidth devices are capable of operating only near a single frequency.

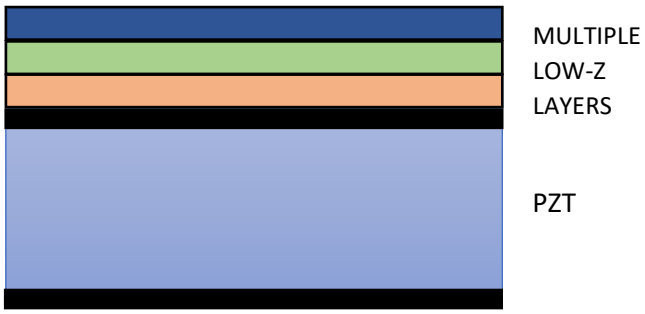

Figure 4.4 Schematic representation of a probe with decreasing impedance layers

To reduce the higher acoustic impedance that characterizes the traditional piezoceramics transducers, piezopolymers are often used, which are also easier to manufacture and more flexible, allowing the construction of curved focused probes, besides favouring a more effective coupling with the air. Among the most common ones there is PVDF, (Polyvinylidene Fluoride), characterized by relatively low acoustic impedance, as well as low density and velocity. To further

reduce the high acoustic impedance, piezocomposite transducers of different types are made, depending on the electrical and mechanical connectivity. This is usually a so-called 1-3 connection, in which an epoxy resin matrix contains PZT (Lead Zirconate Titanate) pillars. This matrix has a lower density and helps dampen the inter-pillar vibration modes of the element. Within the composite material, the ratio of the ceramic can be varied in order to make the device more suitable as a transmitter or receiver. As it is difficult to make a single probe to implement the pulse-echo technique, these types are often used in the through-transmission mode.

Another kind of transducers is represented by capacitive transducers (also called electrostatic transducers), which instead are broadband and can work over a wider frequency range. They consist of a rigid back electrode and a flexible one placed a few μm from the former, between which there is an air gap. A capacitor is then formed, which acts like a transmitter when an alternating voltage is applied between the electrodes, which causes the film to vibrate, producing ultrasound in the air. In detection mode instead it picks up the ultrasonic waves in case a d.c. bias voltage is applied [81]. In the frequency range of <100 kHz to about 2 MHz, the response is well attenuated, and the higher limit is determined by the type of voltage applied and the length travelled by the air [69]. These transducers have demonstrated good sensitivity and bandwidth for use in ultrasonic inspection of polymeric materials and fibre-reinforced composites [82]. The main characteristic of the micromachined capacitive transducers that distinguish them is the ability of varying the operation frequency. This enhances the low signal-to-noise ratio that emerges from air/solid coupling, allowing it to accommodate various types of material resonant vibrations [66]. Thanks to the presence of the air gap between the two electrodes in its design, a better matching with air is given by the capacitive transducer with respect to piezoelectrics [83].

A further optimization is obtained with hybrid devices (Figure 4.5), which generate ultrasounds by a piezoelectric element and detect the waves by a capacitive element. In fact, the piezoelectric element moves a larger mass of air more easily and therefore it is more efficient to yield waves,

which are received without difficulty by striking a small mass of the capacitive membrane. The pulse-echo configuration might also be possible using these devices.

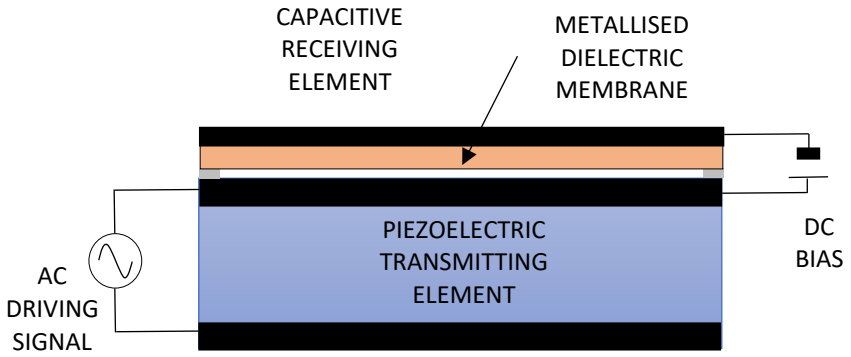

Figure 4.5 Hybrid device consisting of a piezoelectric and a capacitive element

For ultrasound generation, there are also other types of transducers besides the common piezoelectric disks with coupling layer or capacitive transducers, these can be exciting lasers, ferroelectric transducers and thermoacoustic emitters [74]. Ferroelectric polymers are charged cellular polymers that exhibit piezoelectric and pyroelectric properties. Commercial polypropylene cellular (cPP) films can be employed without matching layers due to their very low acoustic impedance (0.03MRayl) which is comparable to that of air. [84].

In the table below, (Table 4.1) the values of density ρ, sound velocity in the materials c, impedance Z and reflection R and transmission T coefficients of some materials interfaced with air are shown.

Table 4.1 Value of ρ, c, Z, R and T of some materials interfaced with air

MATERIAL	ρ (kg/m^3)	c (m/s)	Z (MRayl)	R (%)	T (%)
Steel	7800	5900	46	99.9964	0.0036
Aluminium	2700	6130	17	99.9903	0.0097
PE	900	1950	1.8	99.9085	0.0915
PZT	7500	4440	30	99.9945	0.0055
PVDF	1800	2300	4.1	99.9599	0.0402

The transmission and reflection coefficients were calculated considering an interface between the materials in the first column and the air, which is characterised by ρ=1225 kg/m^3, c=343 m/s, Z=412 Rayl.

It is worth noting that the energy loss, i.e. the amount of reflected ultrasounds, decreases if the acoustic impedance of the material gets closer to that of the coupling material, which is air in this case. In fact, the transmission coefficient would be unitary (T=1) if the impedances of the two materials were equal (Z_1=Z_2) [64].

CHAPTER 5

Ultrasound analysis of 3D printed objects

We already discussed the ability of ultrasound analysis to detect defects, assess density and porosity, measure thickness and mechanical properties.

The analysis of 3D printed objects with non-contact ultrasound techniques allows for the same characterisation, but the signal picked up by the receiver is not as simple and easy to interpret as for conventional components, (see Appendix A).

5.1 Materials

The materials used for the 3D printing of the objects via Fused Filament Fabrication (FFF) are thermoplastic polymers: Polylactic acid (PLA) and Acrylonitrile Butadiene Styrene (ABS), which are the most common feedstock materials for the process. In this work, filaments with a diameter of 2.85 mm were employed.

PLA is biodegradable, odourless, generally easy to print and requires less energy (lower temperatures) to be printed than most plastics [85]. ABS, on the other hand, is characterised by good toughness and resistance to high temperatures but requires a higher nozzle temperature and a heated printing bed, and it emits potentially harmful fumes [86].

Table 5.1 Properties of Polylactic acid (PLA) and Acrylonitrile Butadiene Styrene (ABS) [87]

Property	PLA	ABS
Build plate temperature (°C)	20 - 60	80 - 110
Printing temperature (°C)	180 - 230	210 - 250
Heat resistance	Low	Moderate
Strength	Brittle	Impact resistance
Flexibility	Low	Medium
Raft	Optional	Recommended
Shrinkage/Warping	Minimal	Considerable
Fumes	Little/None	Intense

The most divergent characteristics have been included in the table 5.1; the two materials also share similar characteristics in terms of price, strength and storage recommendations (dry environment).

5.2 3D printers and slicer software

The choice of 3D printer has an impact on the quality of the final product. Before carrying out the ultrasound tests, objects were produced with three available commercial 3D printers: Ultimaker s3, Ultimaker s5 and Stratasys Dimension elite.

Table 5.2 Main features of printers [88], [89], [90]

Features	**Ultimaker s3**	**Ultimaker s5**	**Stratasys Dimension Elite 3D Printer**
Build material	PLA, ABS, PVA, Nylon, PC, PP, …	PLA, PVA, ABS, CPE, Nylon	ABS plus
Support material	PLA, Nylon, ABS, PC, PP, PVA, Breakaway, …	PLA, Nylon, ABS, PC, PP, PVA, Breakaway, …	Soluble
Part density	1 – 100%	1 – 100%	Solid, Sparse-low density, Sparse-high density
Min. Layer thickness	20 - 600 µm depending on the nozzle size	20 - 600 µm depending on the nozzle size	178 µm or 254 µm
Nozzle diameter	0.25 mm, 0.4 mm, 0.6 mm, 0.8 mm	0.25 mm, 0.4 mm, 0.6 mm, 0.8 mm	-
Max. Printable size	230 x 190 x 200 mm	330 × 240 × 300 mm	203 × 203 × 305 mm
Software	Ultimaker Cura	Ultimaker Cura	CatalystEX

PLA samples were produced with the two Ultimaker s3 and s5 printers, while the Stratasys Dimension elite worked exclusively with ABSplus. This is because PLA is easier to use and is more flexible to printing conditions such as those found in a desktop printer like the Ultimaker s3. ABS, on the other hand, is prone to shrinkage when printed in open 3D printers and therefore requires special printers with an enclosed printing chamber controlled by a heating system, such as the Dimension elite. The finished products obtained with this professional machine have a high quality and excellent process repeatability is guaranteed.

Slicing software CatalystEX and Ultimaker Cura allowed the setting of the printing parameters such as nozzle and printing plate temperatures, layer and perimeter thicknesses, position of the object on the platform, printing speed, etc. Note that the two software allow for different options for the object infill: low, medium or high in CatalystEX, which correspond to approximately 20, 60 and 100% infill in Cura.

5.3 Equipment

The testing equipment is comprised of the following components (figure 5.1), which operate simultaneously for the proper conduct of experiments:

- **Thurlby Thandar Instruments (TTi) TGP110 10 MHz Pulse generator (low voltage pulse generator)**

  It is a pulse generator that operates in the frequency range of 0.1 Hz to 10 MHz and from which mode, period, bandwidth and delay of the pulse can be set. It is connected to an amplifier to excite the transmitter and to an oscilloscope, making it possible to set a delay between the Sync Output and the Pulse Output [91].

- **Falco Systems WMA-300 DC - 5 MHz High Voltage Amplifier (50x gain high voltage amplifier, up to 300 V DC)**

  The amplifier is characterised by 5MHz bandwidth DC current and 300mA output current, and it allows 50x high voltage amplification up to ± 150 V [92]. After amplifying the signal, it transfers it to the transmitter by passing it through a decoupler.

- **Decoupler circuit**

  The decoupler circuit, housed in an aluminium box, receives DC bias voltage from the power supply via banana sockets and is connected to the transmitter and an amplifier via BNC sockets for signal transfer. It prevents excessive current absorption from the signal generator and mixes the amplified signal with the 100 V DC from the power supply before the signal reaches the transmitter.

- **Cooknell SU2/C Power Supply and Cooknell CA6/C Charge Amplifier**

  The SU2/C unit works together with the CA6/C amplifier for good signal transfer. The power supply is equipped with two channels, each with one input and one output, the latter

featuring a 0-100 V bias voltage that can be individually adjusted with 10-turn dials. A bipolar BNC cable connects it to the very low noise, charge-sensitive amplifier, which receives the signal from the receiver on the other side with a standard BNC cable.

- **Delta Elektronika ES 0300-0.45 Power Supply (DC bias supply, up to 300 V DC)**

  The power supply is used to power the transmitter via the decoupler to which it is connected by shrouded plug wires to protect against high output voltage. This is in the range 0-300 V while the current range is 0-450 mA, which can be adjusted with 10-turn potentiometers [93].

- **Tektronix TDS200 Series Digital Oscilloscope**

  It represents the signal (voltage as a function of time) on its display. Its main features are 2 channels and an external trigger, 60 MHz bandwidth, 1 GS/s sampling frequency for each channel, time/division range 5 ns to 5 s/div, sensitivity 2 mV to 5 V/div [94]. Two BNC cables connect channel 1 with the output of the power supplier and the output of the pulse generator is connected to the external trigger of the oscilloscope.

- **2 x Senscomp 600 environmental grade capacitive ultrasonic transducers**

These are electrostatic transducers with a frequency of 50 kHz, a broadband frequency response and excellent reception sensitivity [95]. These capacitive transducers are housed in aluminium boxes with grounded BNC connectors and the BNC cables are shielded for connection to them.

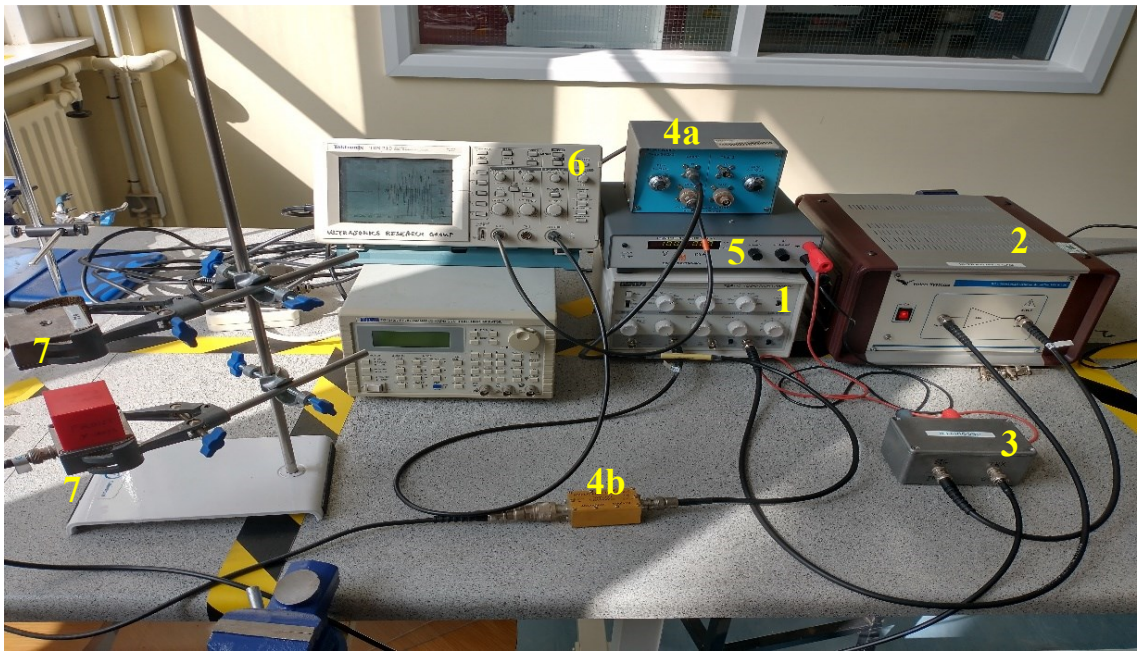

Figure 5.1 Equipment and connections.

1. TGP110 Pulse generator; 2. Falco Systems High Voltage Amplifier; 3. Decoupler circuit; 4a. Cooknell Power Supply, 4b. Cooknell Charge Amplifier; 5. Delta Elektronika Power Supply; 6. TDS200 Series Digital Oscilloscope; 7. Senscomp 600 capacitive ultrasonic transducers

5.4 Calibration and connection

The first step is to verify the correct operation of the equipment; then, the system is calibrated before conducting the experiments.

At the beginning, all devices must be switched off (switching on an instrument in an unknown state could damage transducers or cause further hazards). Correct functioning of the transducers is verified first. The receiver must be connected to the power supply via an amplifier using shielded BNC cables. The output of the power supply is connected to the oscilloscope on which the vertical and horizontal scales are adjusted to 50.0 mV and 1.00 ms respectively. The power supply is activated by turning the "Bias 0-100V" knob clockwise until the number 10 is read. After "AUTO Mode" is set in the trigger menu of the TDS200, a signal will appear on the oscilloscope screen

which updates continuously; any noise near the receiver should result in a response from the oscilloscope.

The next step ensures that the pulses generated are 3.00 V and 10.0 µs wide before high-voltage amplification. The voltage sensitivity of the oscilloscope is set to 1.00 V and the time scale to 10.0 µs. On the oscilloscope, the "NORMAL Mode" is set and the parameters set on the generator are: "PERIOD" in the 10 ms range with the control knob turned fully clockwise to 10, "PULSE WIDTH" to 5 µs by turning the controller below to the second sign after 1 so that the pulse width is 10 µs, "PULSE DELAY" to 50 ns and "AMPLITUDE" set to 3. The 'SYNC OUT' socket of the TTi TGP110 pulse generator is connected to the 'EXT TRIG' socket on the front panel of the TDS200 using a shielded BNC cable.

A similar cable is used from the "MAIN OUT 50 Ω" socket of the TTi TGP110 pulse generator to the "CH1" socket on the front panel of the TDS200. The pulse generator is then switched on from the front panel and a narrow pulse appears on the oscilloscope display. This is adjusted to a width of 10 µs by turning the controller on the pulse generator. Its amplitude is also adjusted so that it is no greater than 3 V.

These settings ensure that there is no overlapping of pulses. By adjusting the PERIOD and WIDTH of the pulses, it is guaranteed that for each pulse sent there is sufficient time for all gradually decreasing echoes reflected by the receiver before another pulse is produced. In addition, the signal undergoes 50x high voltage amplification up to ± 150 V by the amplifier, which is why the pulse width should not exceed 3 V.

The next step is to check that the high-voltage DC bias supply is correctly set to 100 V. It is ensured that the red '+' and black '-' terminals of the Delta Elektronika are connected to the red 'D.C. BIAS' and black 'GND' terminals of the decoupler respectively, and that the 'TRX OUT' socket of the decoupler is correctly connected to the Senscomp 600 transmitter via a shielded BNC cable.

The Delta Elektronika ES 0300-0.45 is switched on; the display should show '000' in green digits for both voltage in V and current in mA.

The "DC 0-450 mA" dial is then carefully turned clockwise approximately ¼ turn, then the "CV 0-300 V" dial is turned clockwise until the display shows "100" for voltage V. The current in mA must remain at '000'.

Finally, the high-voltage amplifier is connected: the "OUTPUT" socket of the Falco Systems WMA-300 must be connected to the "SIG IN" socket of the decoupler circuit using a shielded BNC cable. The "MAIN OUT 50Ω" socket of the TTi TGP110 pulse generator must be connected to the "INPUT" socket of the Falco Systems WMA-300 using a shielded BNC cable and the "OUT" socket of the Cooknell SU2/C must be connected to the "CH1" socket of the TDS200 series oscilloscope using a shielded BNC cable.

Once all the equipment has been set and properly connected, the system calibration is performed by placing the two sensors facing each other, with the faces of the transmitter and receiver parallel and overlapping with an air gap of 10 cm. On the front panel of the TDS200 the "HORIZONTAL SEC/DIV" is then adjusted until the displayed time base indicates 100 μs.

After switching on Falco Systems WMA-300 high-voltage amplifier, a faint clicking noise should be heard from the Senscomp 600 transmitter as individual pulses propagate through the air gap and an oscillating signal should appear on the right-hand side of the TDS200 oscilloscope display.

For a transducer separation (L) of about 10 cm, this signal should start at a time of about 350 μs.

This value (ToF_a) may vary slightly, depending on environmental conditions (i.e, temperature of the room) when the experiments were conducted. The temperature, in fact, influences the speed of the ultrasound waves in air (c_a), and so each time the ToF of the signal in the air is noted down and the relative speed calculated with the following equation (5.1):

$$c_a = \frac{L}{ToF_a} \tag{5.1}$$

An example is shown in the following figure (5.2).

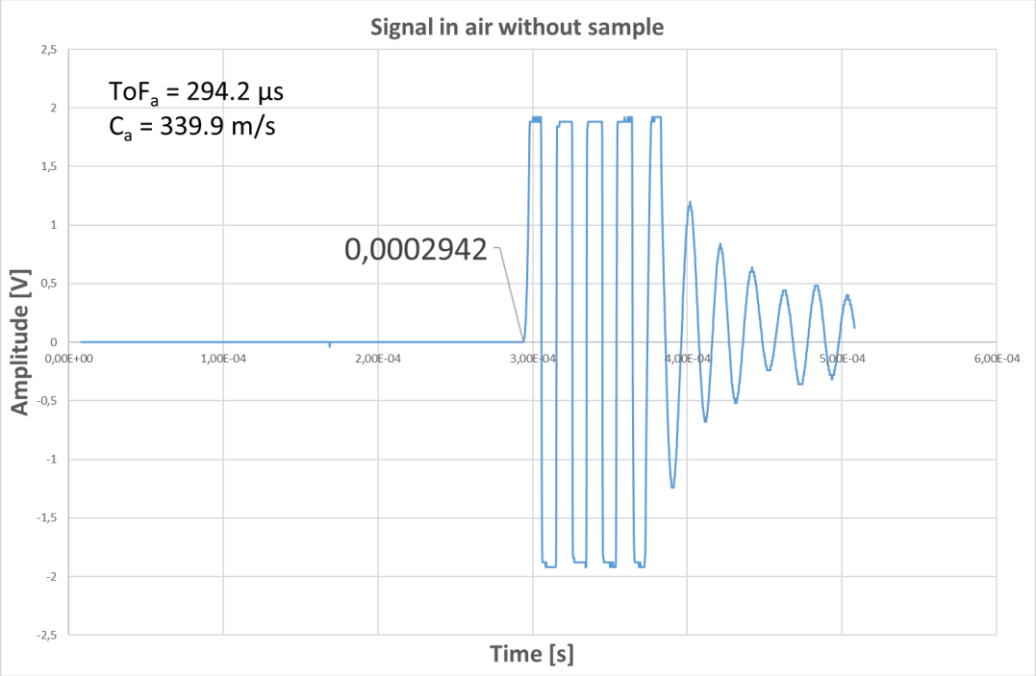

Figure 5.2 Initial ultrasound signal travelling between transmitter and receiver without any interposed samples

During the calibration process, by varying the WIDTH of the pulse, it is also possible to adjust the frequency range at which the transmitter works; if the WIDTH is decreased slightly, the frequency increases accordingly. This way, the preferred frequency of 50 kHz can be set for the transmitter.

When conducting the experiments, the vertical sensitivity of the oscilloscope is increased as the signal is of the order of mV. This also increases the noise, so the environment must be quiet and minimally disturbed. The air-coupled capacitive transducers used here have a wide frequency bandwidth, but the signal level obtained from these devices tends to be low. To extract the signals from the noise, averaging is therefore performed using the AVERAGE function of the oscilloscope, reducing the noise and stabilising the signal.

After confirming correct functioning and calibration, ultrasonic tests were performed on 3D printed objects produced with different materials and infill patterns.

CHAPTER 6

Experiments and results

In order to understand whether there is a relationship between sound speed and intensity of the received signal with internal pattern and density, all data obtained in the measurements of different samples were analysed and compared. The aim is to be able to extrapolate information on the samples, such as its internal pattern or the density, from the variations in the speed of sound, signal intensity and shape; if the internal pattern is known, the orientation along which the measurement takes place could be identified. The portion of the signal considered is that collected before the ToF_a; in fact, the two portions may interfere, constructively or destructively, and not accurately represent the energy content. In the first part of the chapter, samples made in PLA and with Ultimaker s3 were analysed, in the second part, the material and printer were varied to check for any influence.

6.1 Reproducibility and errors

The experiments were repeated on different days to verify the reproducibility of the tests. Furthermore, for each orientation, ultrasounds were introduced from both opposite faces of the cubes, verifying the symmetry of the sample. Differences in ToF_m were detected, due to the fact that the pattern inside is not perfectly symmetrical, the signal is reflected differently at the different air/material interfaces and due to environmental conditions that influence the results obtained from measurements on different days. The velocities on the different days were quite similar with a variation of ToF of 0.2 or 0.4 μs. Therefore, a comparison between the signals was made considering the speed of sound, the shape of the signal and the normalised frequency spectrum. The noise in the signal due to the surrounding environment must also be taken into account, such as

other ultrasounds in the air that may be produced by PCs, amplifiers, and other devices which bounce between transmitter and receiver until they disappear and can affect the measurements.

6.2 Cubes with different internal patterns and densities

PLA test specimens were printed with the same geometry, i.e. a cube of side 40 mm, using the Ultimaker s3 printer. Three different patterns were selected for the internal infill: cubic (CU), concentric (CONC) and zig-zag (ZZ) (figure 6.1); each of the patterns is reproduced with three different infill densities (15%, 20% and 60%). A total of nine cubes was therefore produced.

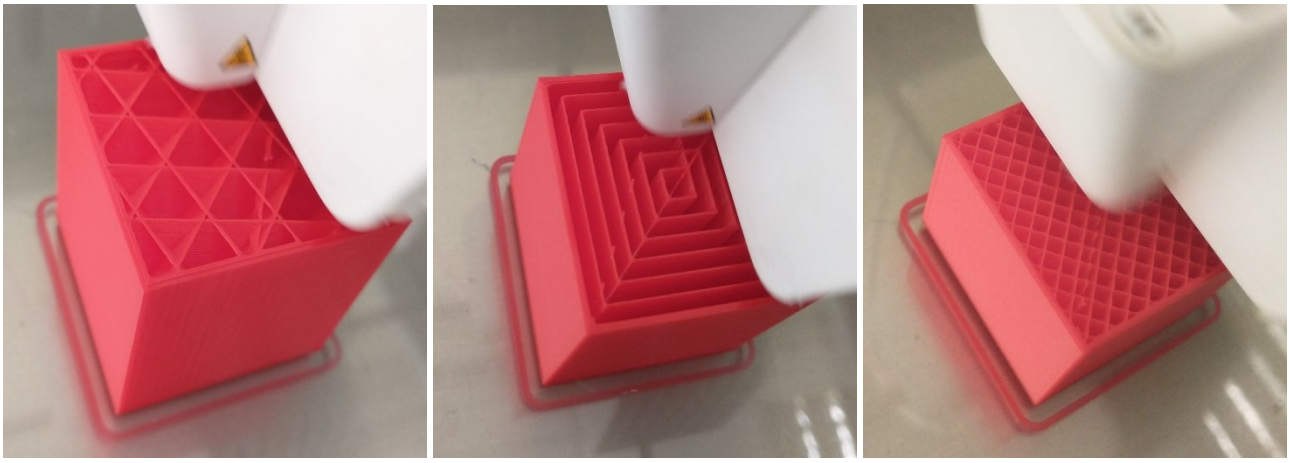

Figure 6.1 Different types of infill pattern: (left to right) Cubic, Concentric, Zig-Zag

The three models differ mainly in the construction of the various layers. In fact, in the CONC one all layers are perfectly overlapping, in the ZZ one they repeat alternately, while the cubic one has a 3D geometry in which each layer is different, creating closed air pockets.

The cubes were analysed with ultrasound by recording the time of flight and signal amplitude along the three axes of the objects, x, y and z. The orientation of the cubes along which the ultrasound passes will follow the following legend, (see also figure 6.2):

- standing = stand orientation = z-axis,

- lying on the side = side orientation = x-axis,

- lying on front = front orientation = y-axis.

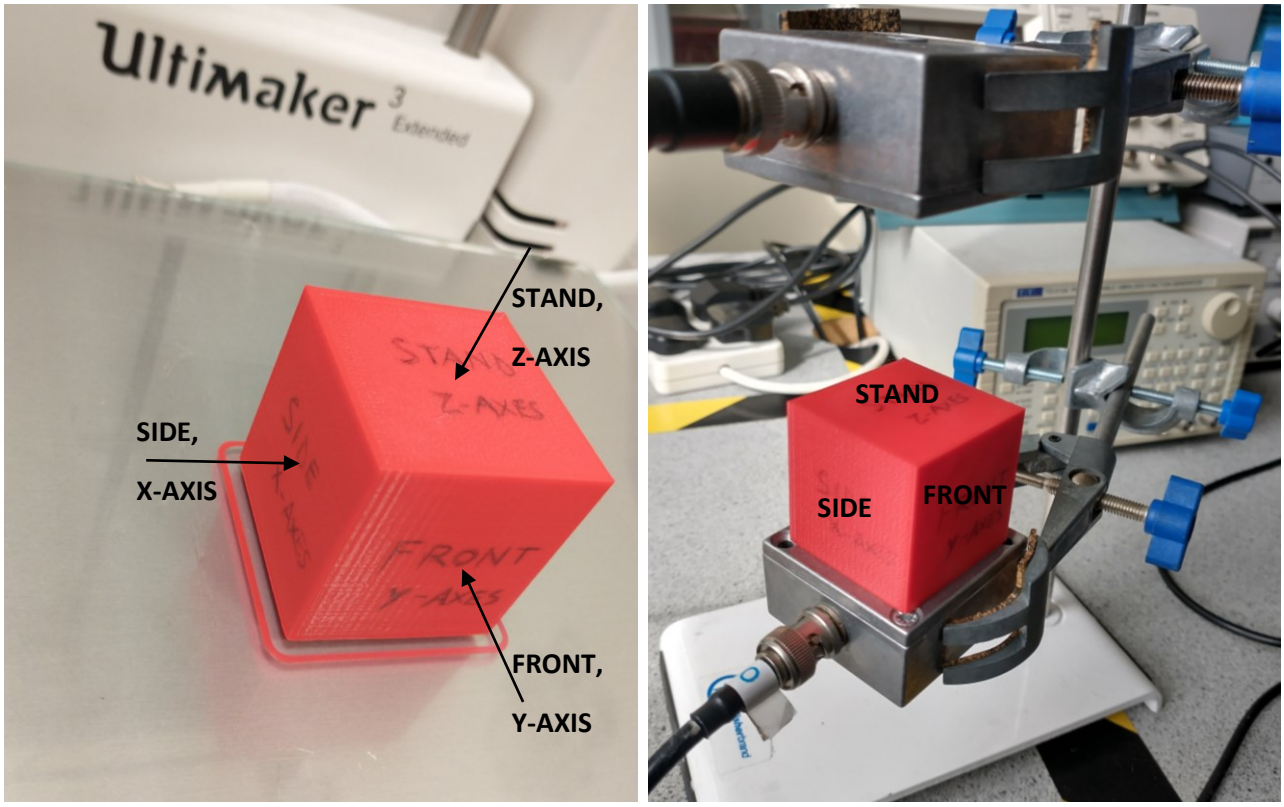

Figure 6.2 Orientation of the 3D printed cube. In relation to the construction platform (left) and the probes (right)

The same experiment was carried out on the same sample on different days to assess the reproducibility of the results. As mentioned, the speed of the ultrasound also varies depending on the environmental conditions and in particular the temperature. On warmer days, the ultrasounds travel faster, passing through the sample in a shorter time. Using equation 6.1, it is possible to have a theoretical value of the sound in air before the measurement using the probes and the oscilloscope.

$$C_a = \sqrt{\gamma_{air}\, R_{air}\, T} \tag{6.1}$$

with

$\gamma = \frac{c_p}{c_v}$, ratio of specific heats of a gas at constant pressure and constant volume respectively, (=1.4),

R_{air} = 287 [J/kg K] specific gas constant for air.

Before starting the sample tests, the speed of sound was measured without a sample between the probes, using formula 5.1, as seen in the previous paragraph.

This was found to be C_a = 339.9 m/s, with

- L = 10 cm distance between the probes.

- ToF_a = 294.2 μs sound flight time from transmitter to receiver.

These data will be used in the following sections of this chapter to calculate the various C_m.

Interposing the samples between the probes results in shorter times of flight; in fact, the sound travels through the material at a higher speed C_m.

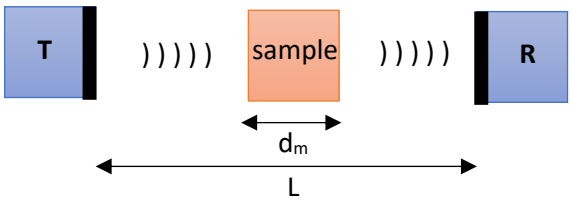

Figure 6.3 Schematic representation of transmitter, receiver and sample

Referring to figure 6.3, the ultrasound velocity within the sample was calculated using the following equation (6.2):

$$C_m = \frac{d_m}{\frac{d_m}{C_a} - \Delta t} \tag{6.2}$$

Where:

- d_m is the thickness of the sample.
- Δt is the difference between the time required by the ultrasound waves to reach the receiver without a sample and the signal start time when the sample is interposed.

6.2.1 Cubic pattern

Table 6.1 reports the signal data for the experiments performed on the cubes with cubic infill pattern. It shows that, for all infill densities, the ultrasound waves travel more slowly when the cube is standing, while the two lying orientations are quite similar. The maximum peak amplitude is in the standing orientation for 60% density, while this orientation has the lowest peak in the other two densities. For each orientation, as the density increases, the speed at which the ultrasound travels through the sample increases and the peaks appear higher.

The cubes with 15% and 20% infill densities behave similarly and show the same number of peaks (3) in the portion of interest; the cubes with 60% infill density show a similar wave shape, yet 4 narrower peaks. A smaller number of peaks means a lower transmitted frequency; samples with lower density contain more air, and the high frequencies are reflected more as they travel through it. In the denser sample, on the other hand, there is less air to travel through, thus less reduction of high frequencies and higher energy.

Table 6.1 Signal data at different infill densities and orientations for cubes with cubic infill pattern

CUBIC	Orientation	ToF$_m$ (µs)	Δt (µs)	Ultrasounds speed, C$_m$ (m/s)	Amplitude max. peaks (mV)	Peak-peak (mV)
15%	STAND	214.2 similar	80 similar	1061.52 similar	4.4; -8.4	12.8
	SIDE	209.4 (208.8)	84.8 (85.4)	1216.48 (1239.09)	6; -11.2	17.2
	FRONT	208.6 similar	85.6 similar	1246.82 similar	7.6; -12.8	20.4
20%	STAND	214 (213.4)	80.2 (80.8)	1067.19 (1084.55)	8.4; -18	26.4
	SIDE	208.8 similar	85.4 similar	1239.09 similar	10.8; -16	26.8
	FRONT	208.2 (209.2)	86 (85)	1262.56 (1223.93)	11.6; -17.6	29.2
60%	STAND	209.2 similar	85 similar	1223.93 similar	24.4; -34	58.4
	SIDE	207 similar	87.2 similar	1312.26 Similar	20; -28	48
	FRONT	206.6 similar	87.6 similar	1329.71 similar	19.6; -27.2	46.8

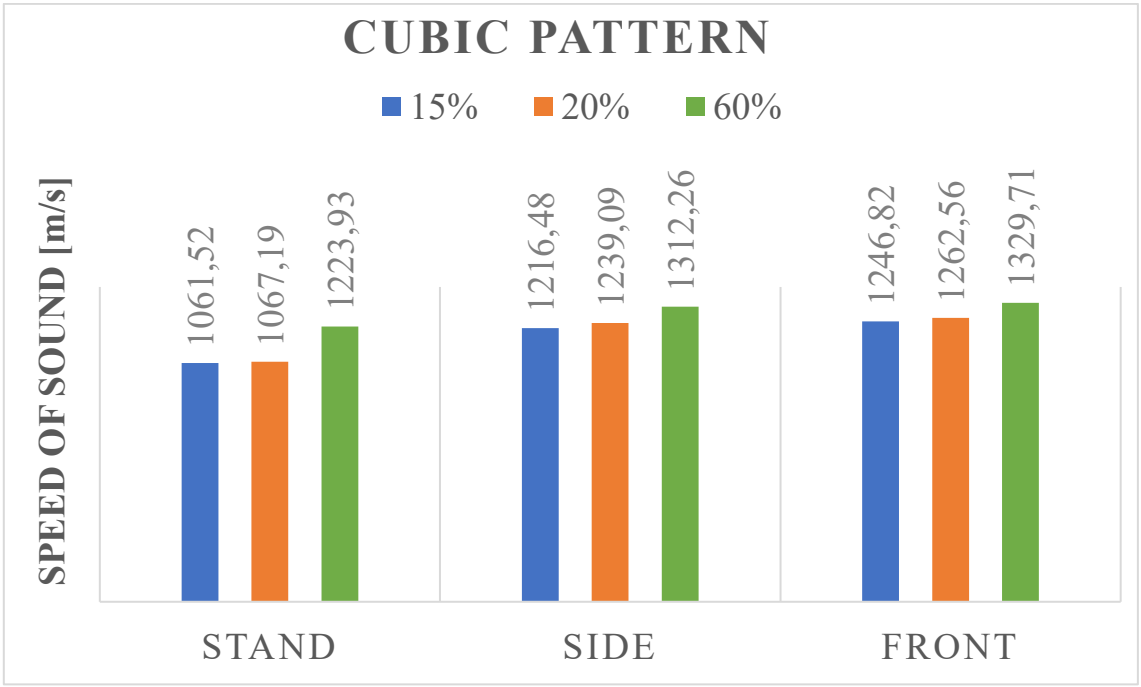

Figure 6.4 Comparison of ultrasound speed in different orientations and infill density of cubes with cubic infill pattern

For the cubic pattern, we can conclude that the ultrasounds speed increases from 15% to 60% infill density and changing from stand, side and front orientation (figure 6.4). The highest peak is found in the cube with 60% infill density placed in standing orientation, while at lower infill densities an opposite trend is observed.

6.2.2 Concentric pattern

Table 6.2 reports the signal data for the experiments performed on the cubes with concentric infill pattern. In contrast to the previous set of samples, for all infill densities the standing orientation allows the sound to travel faster than it does through the laying orientations. As expected, the concentric configuration is not isotropic; however the two lying orientations were expected to behave the same. However, the measurements show no clear agreement between the two lying orientations; the mismatch can be attributed to internals defect that occurred during the printing process (figure 6.5).

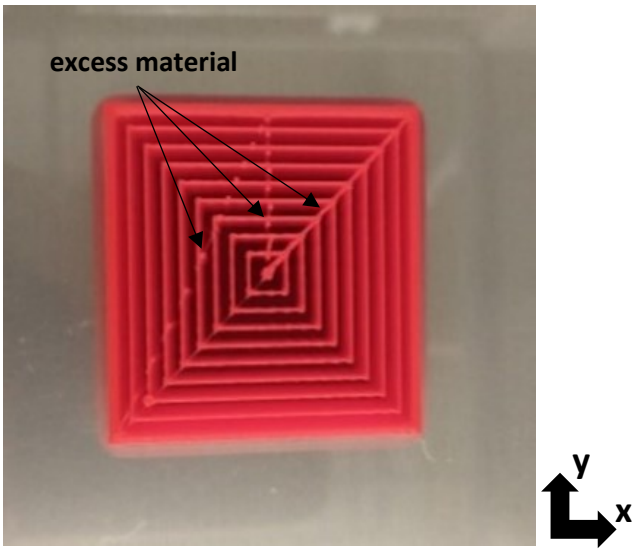

Figure 6.5 Cube with concentric infill pattern: excess material

When the nozzle interrupts the continuous flow of material to move to another position on the plate, it leaves a deposit of excess material; the defects repeat in the same positions in every layer, and their build-up results in additional inner walls. The positions of the defects do not repeat symmetrically in the sample, thus inducing differences in the signal output with the different orientations. The two lying orientations (front and side) with 15% and 20% infill density do not show a significant difference in ultrasound speed. On the other hand, in samples with 60% infill pattern the ultrasounds travel significantly faster through the cube along the x-axis than along the y-axis. This could be explained by the presence of a continuous path of material to travel through that only occurs to a significant extent at high infill density.

In order to verify this hypothesis, open samples (i.e., without the top) were printed to check their internal structure for the presence of excess material. Excess material was indeed present, but not always in the same position. It is not only placed differently in samples with different infill densities, but also in samples sliced and printed with the same parameters (same infill pattern and density; see figure 6.6 and 6.7).

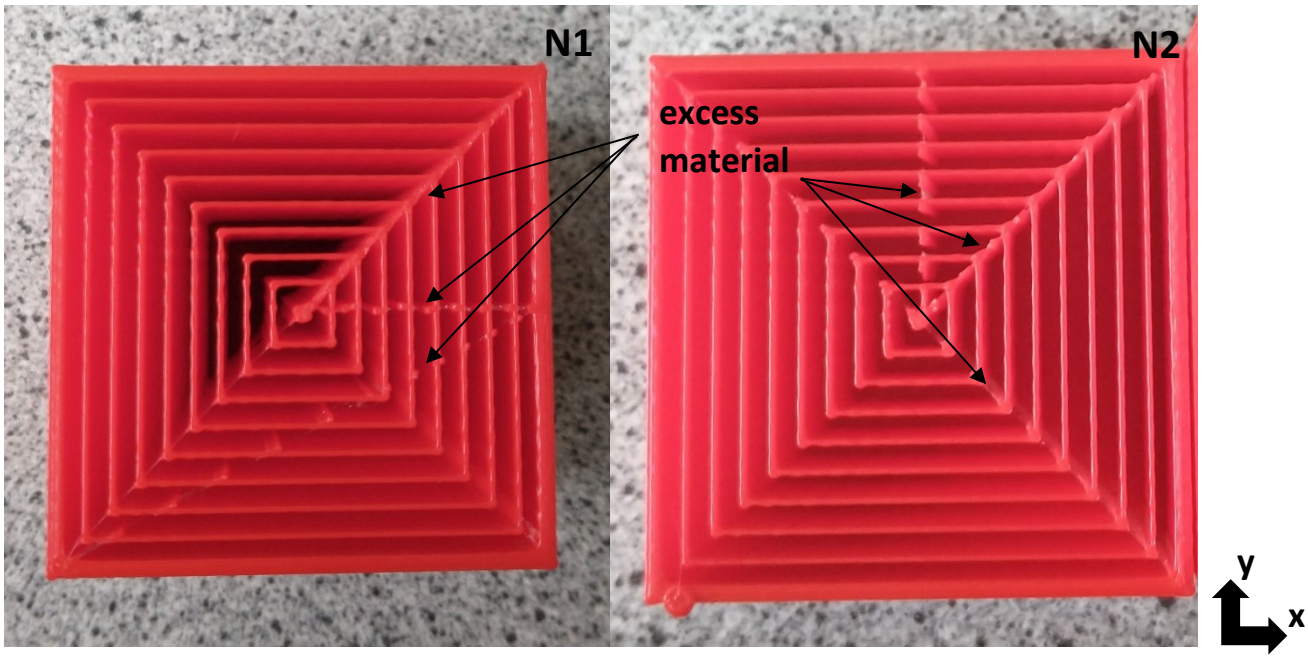

Figure 6.6 Samples of concentric cubes at 20% density with excess material in different positions

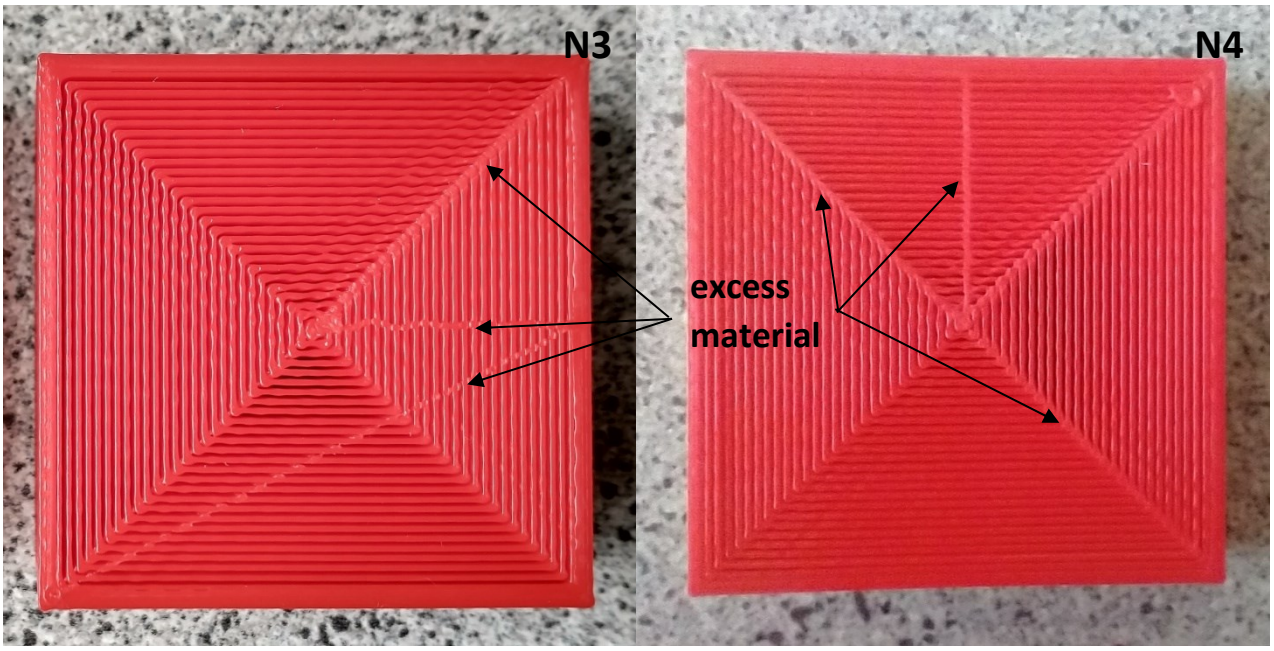

Figure 6.7 Samples of concentric cubes at 60% density with excess material in different positions

The appearance of these defects does not seem to be influenced by the choice of material or printer, yet it can be traced back to the slicing software. In fact, the algorithm that extrapolates the nozzle path from a 3D model has to include travels to different positions in the object which can be introduced in more than one place (hence the differences between models N1, N3 and models N2, N4 in figure 6.6 and 6.7). It is the interruption and reinstatement of material flow that results in the deposition of excess material; more defects of this sort would appear with higher infill density.

The open samples were also analysed with ultrasound, measuring their travel time (table 6.2).

Table 6.2 Ultrasonic velocity through the samples in side and front orientation for samples with 20% and 60% infill density. ToF_a=290.6 μs, C_a=344.11 m/s

20%	Orientation	ToF_m (μs)	Δt	Ultrasounds speed, C_m (m/s)
CONC N1	SIDE	209.6	81	1135.01
	FRONT	209.4	81.2	1141.49
CONC N2	SIDE	205.2	85.4	1296.94
	FRONT	205.2	85.4	1296.94
60%				
CONC N3	SIDE	205.4	85.2	1288.58
	FRONT	207.8	82.8	1196.10
CONC N4	SIDE	209	81.6	1154.67
	FRONT	204	86.6	1349.44

Table 6.2 confirms that at lower density the ultrasound speed is similar in both orientation, while at higher density the side and front orientations become different.

The ultrasound passes through the sample faster along the axis to which an additional inner wall has formed due to the excess material (see figure 6.7). This occurs along the x-axis of the N3 cube and along the y-axis of the N4 cube.

Along the z-axis, the signal travelling through the closed cubes shows clear sinusoids with much higher amplitude. As with the cubic infill pattern, the speed of the ultrasound waves increases as the density of the sample increases (table 6.3 and figure 6.8). On the other hand, the sample with the highest infill density shows the least number of peaks (3 instead of 4) as reported in figure 6.9; moreover, their amplitude decreases from 15% to 60%. In the other two orientations, the peaks are considerably smaller and difficult to distinguish but appear rather similar and just slightly higher in the denser sample.

Table 6.3 Signal data at different infill densities and orientations for cubes with concentric infill pattern

CONCENTRIC	Orientation	ToF$_m$ (µs)	Δt (µs)	Ultrasounds speed, C$_m$ (m/s)	Amplitude max. peaks (mV)	Peak-peak (mV)
15%	STAND	205.4 similar	88.8 similar	1384.96 similar	64.8; -73.6	138.4
	SIDE	210.8 (213.4)	83.4 (80.8)	1166.8 (1084.55)	-1.6; -3.28	1.68
	FRONT	211.2 similar	83 similar	1153.35 similar	-1.84; -2.88	1.04
20%	STAND	205.8 similar	88.4 similar	1366.04 similar	61.4; -69.6	131
	SIDE	211.6 (213)	82.6 (81.2)	1140.17 (1096.44)	-1.92; -3.28	1.36
	FRONT	211.2 (210.2)	83 (84)	1153.35 (1187.59)	-1.92; -3.36	1.44
60%	STAND	204 similar	90.2 similar	1455.51 similar	25.2; -30	55.2
	SIDE	226.4 similar	67.8 similar	801.9 similar	-1.36; -4	2.64
	FRONT	232.2 (229.6)	62 (64.6)	718.37 (753.55)	-1.52; -3.2	1.68

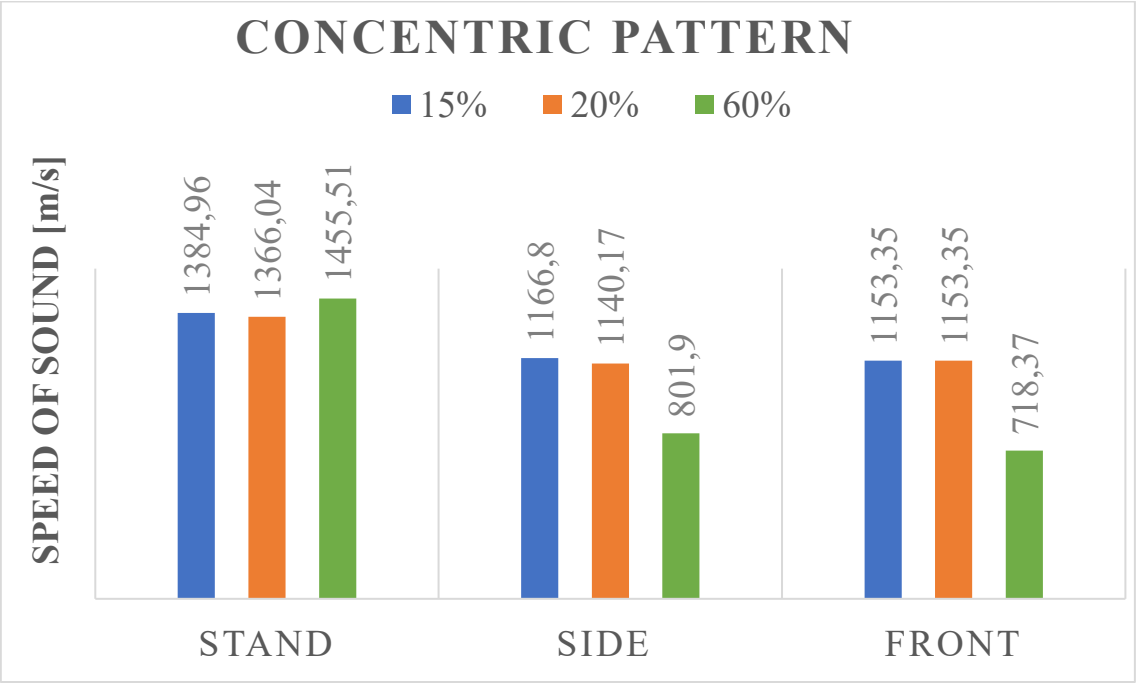

Figure 6.8 Comparison of ultrasound speed in different orientations and infill density of cubes with concentric infill pattern

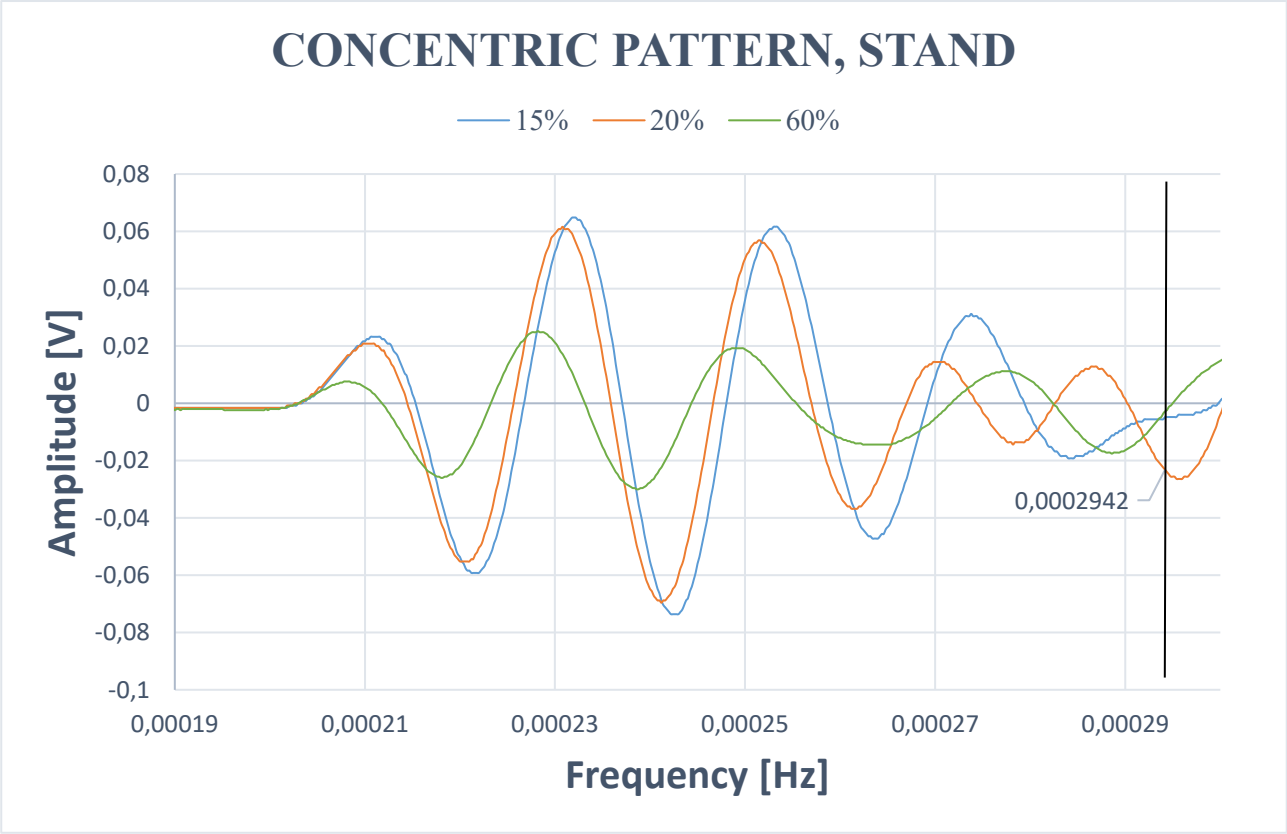

Figure 6.9 Ultrasound signals through cubes with concentric infill in stand configuration, at 15%, 20% and 60% infill density

It can be concluded that with the concentric pattern both the speed and the peak amplitude of ultrasound waves is higher in the standing orientation for any % density.

6.2.3 Zig-zag pattern

Wavelength resulting from the experiments on samples produced with zig-zag infill pattern were more difficult to analyse; in fact, the wavelength of the ultrasounds is large compared to the size of internal features and consequent air gaps. The effect of small variations on the signal is equally small and the sensitivity of the oscilloscope has to be increased to show the portion of interest of the wave.

In the cube with 15% infill density analysed in the standing configuration, for example, the onset of the signal shows a gradual increase, making it difficult to identify the exact moment of its beginning; therefore, several measurements were performed while varying the sensitivity of the oscilloscope in order to better visualise the phenomenon. The samples with 20% infill density show a similar trend; in both cases, the lying orientations allow the ultrasound waves to travel faster than in the standing orientation. Despite the small difference in density, the samples with 20% infill density produce a signal with higher speed and almost twice the peak amplitude (table 6.4). For a fixed orientation, the wave trend between equal orientation and different densities remains the same, with the number of peaks present increasing as the density increasesas observed with all infill patterns. For each infill density, the highest peak amplitude in the signal is reached in the stand orientation, although at higher density the difference becomes less evident. No amplitude trend with increasing density is observed for this pattern in the standing orientation, yet it appears in the lying orientations. Along the x- and y-axis, the zig-zag infill pattern is rather isotropic and the resulting signal is similar.

Table 6.4 Signal data at different infill densities and orientations for cubes with zig-zag infill pattern

ZIG-ZAG	Orientation	ToF$_m$ (µs)	Δt (µs)	Ultrasounds speed, C$_m$ (m/s)	Amplitude max. peaks (mV)	Peak-peak (mV)
15%	STAND	229.8 (226.6)	64.4 (67.6)	750.73 (798.69)	26.8; -42.4	69.2
	SIDE	212.8 (207.2)	81.4 (87)	1102.48 (1303.7)	2.88; -7.28	10.16
	FRONT	211.8 similar	82.4 similar	1133.73 similar	3.2; -7.76	10.96
20%	STAND	222.8 similar	71.4 similar	864.27 similar	67.2; -76	143.2
	SIDE	212.6 (211.4)	81.6 (82.8)	1108.6 (1146.73)	14.8; -20.4	35.2
	FRONT	215.4 (216.4)	78.8 (77.8)	1028.76 (1002.97)	18.6; -23.4	42
60%	STAND	210.6 similar	83.6 similar	1173.65 similar	40.8; -48	88.8
	SIDE	212 (213.2)	82.2 (81)	1127.34 (1090.46)	26.8; -36.4	63.2
	FRONT	213.2 similar	81 similar	1090.46 similar	28; -38	66

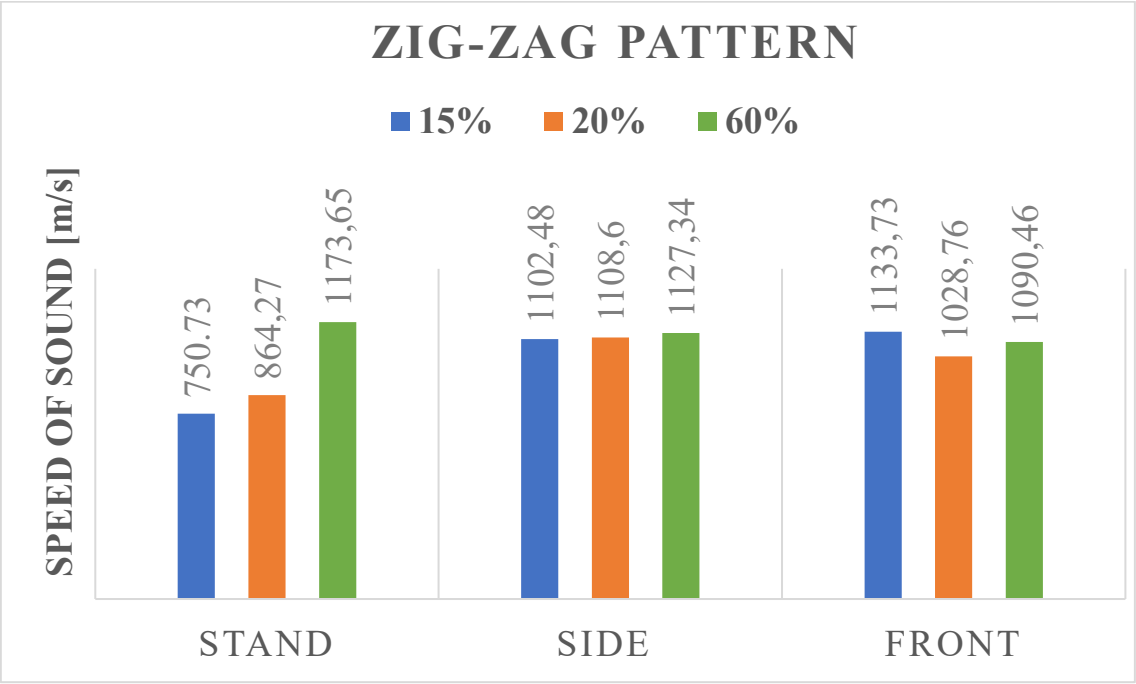

Figure 6.10 Comparison of ultrasound speed in different orientations and infill density of zig-zag cubes

The speed of the ultrasounds waves in the samples increase with increasing density in the cubes in the stand orientation; along the x- and y-axis of the samples, on the other hand, no significant differences are detected.

6.3 Frequency spectrum

In the tests, the signal generated is at 50 kHz. It is also possible to further process the signal to obtain the frequency domain representation by applying the fast Fourier transform (FFT). This is called the signal spectrum and shows the signal as an amplitude that varies depending on the frequency, or rather how the energy is distributed at the various frequencies.

A higher energy is expected for the signal collected in the presence of more material (i.e., 60% infill density). The choice of the infill pattern influences the propagation, especially at high frequencies.

6.3.1 Cubic pattern frequency spectrum

Comparing the normalised spectra along the standing orientation in the cubes, the samples with 60% dense cubic infill pattern show a higher peak at about 55 kHz (figure 6.11). Comparing z-axis (figure 6.11) and x-axis (figure 6.12), a smaller difference in height between the peaks at about 39 kHz and at 50 kHz can be detected in the latter. For each orientation, the spectrum broadens as the density decreases.

Table 6.5 Frequency at which more signal is transmitted depending on orientation in cubes with 15%, 20% and 60% cubic infill density

	Orientation	**Maximum Peak Frequency (kHz)**
60%	STAND	39.062
	SIDE	38.605
	FRONT	38.757
20%	STAND	40.283
	SIDE	38.91
	FRONT	39.368
15%	STAND	39.978
	SIDE	39.215
	FRONT	39.673

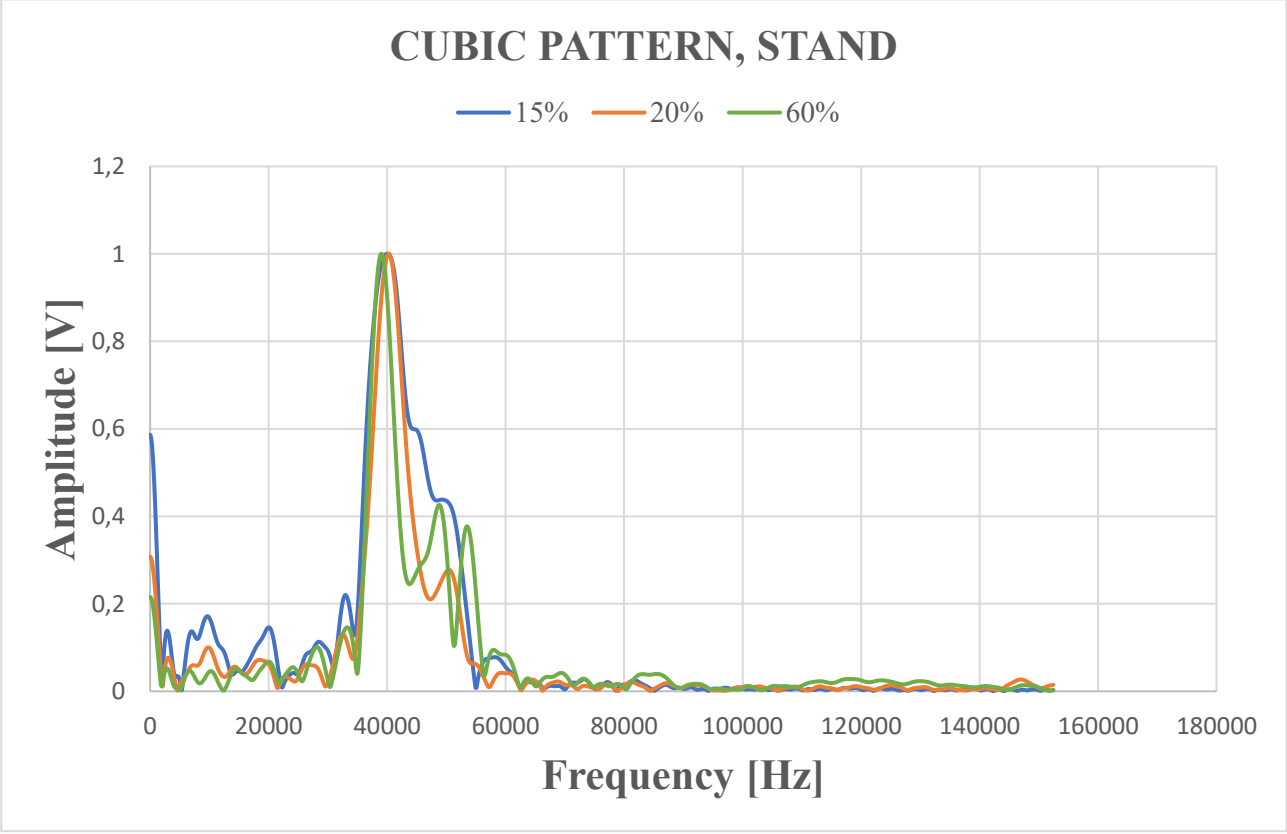

Figure 6.11 Normalised frequency spectra of the cubes with 15%, 20% and 60% cubic infill pattern in stand configuration

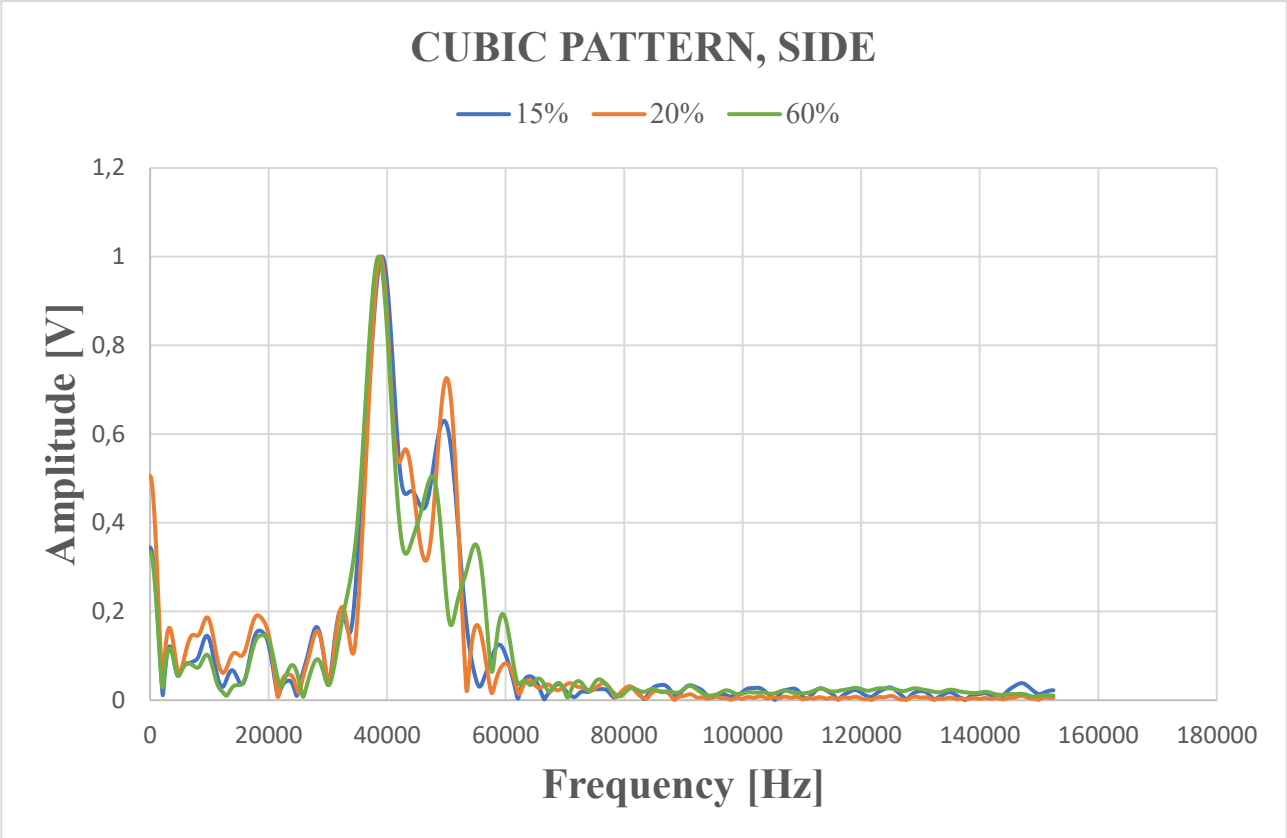

Figure 6.12 Normalised frequency spectra of the cubes with 15%, 20% and 60% cubic infill pattern in side configuration

6.3.2 Concentric pattern frequency spectrum

The stand configuration provides for the highest energy transmission at high frequencies (figure 6.13). The side orientation can be distinguished from the front one thanks to the higher amplitude of the peaks at frequencies higher than 39 kHz (figure 6.14) and the bigger peak width.

Table 6.6 Frequency at which more signal is transmitted depending on orientation in cubes with 15%, 20% and 60% concentric infill density

	Orientation	**Maximum Peak Frequency (kHz)**
60%	STAND	38.757
	SIDE	38.605
	FRONT	38.757
20%	STAND	39.062
	SIDE	38.757
	FRONT	38.910
15%	STAND	38.910
	SIDE	38.757
	FRONT	38.910

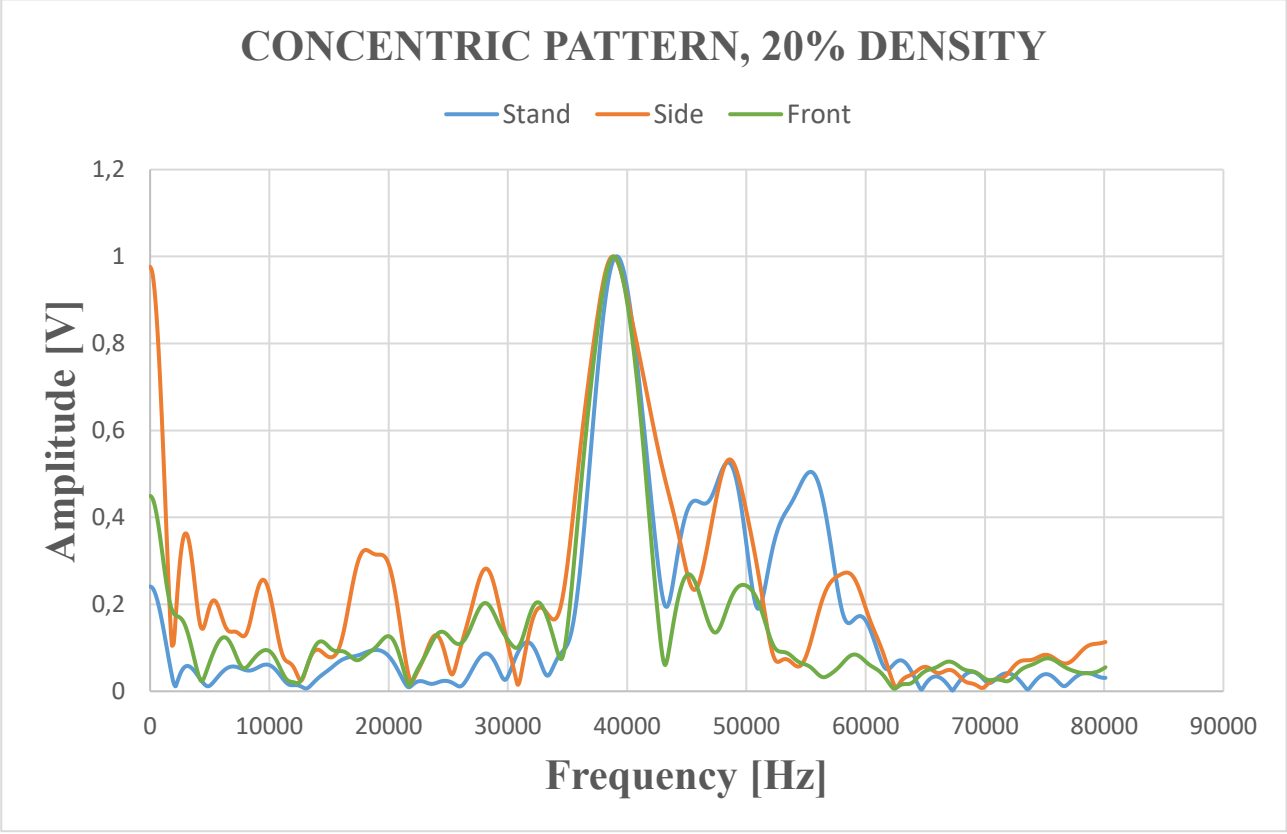

Figure 6.13 Normalised frequency spectra of the cubes with 20% concentric infill patterns in stand, side and front orientations

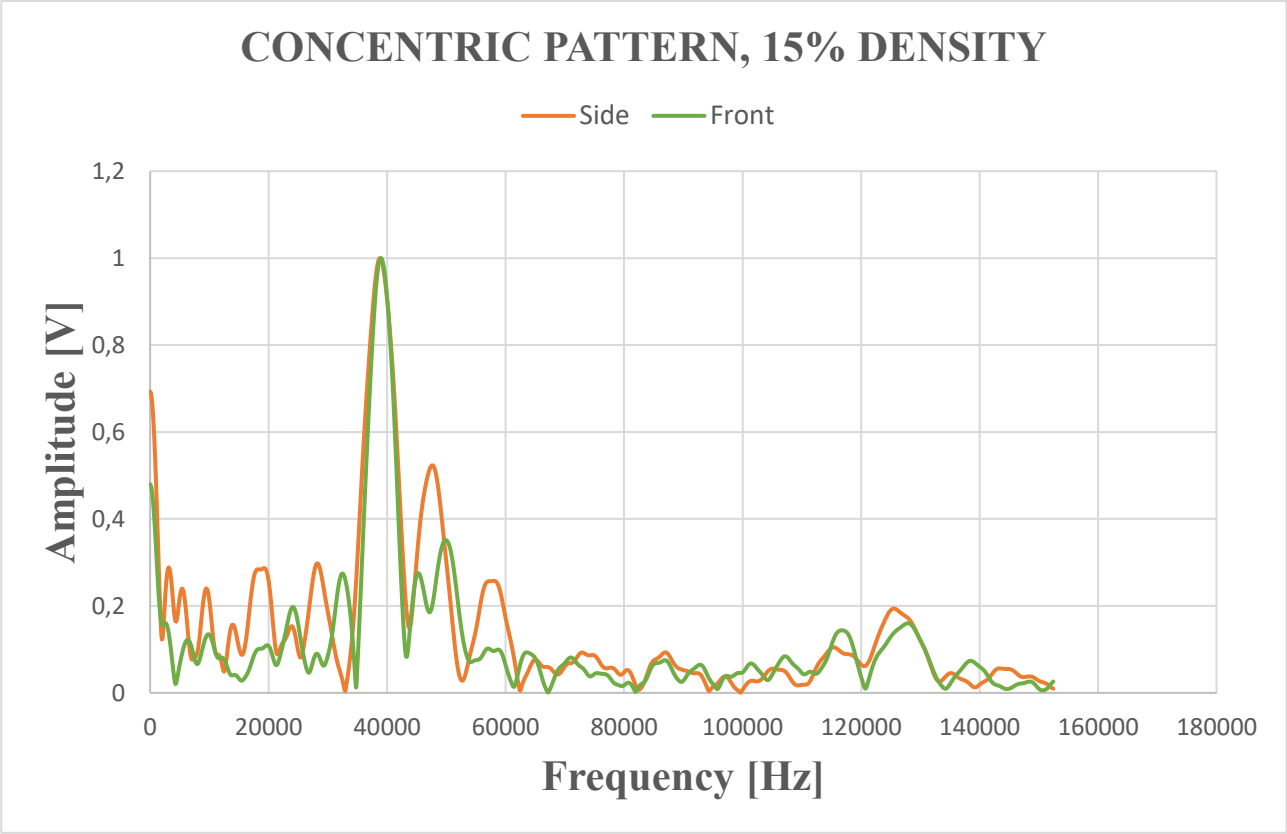

Figure 6.14 Normalised frequency spectra of the of the cubes with 15% concentric infill patterns in side and front orientations

6.3.3 Zig-zag pattern frequency spectrum

Samples with 60% zig-zag infill density in the stand orientation show the highest amplitude near 50 kHz (transmitter frequency), while in the side and front orientation the highest peak occurs at 39 kHz (figure 6.15); even so, the front and side orientations transmit more at high frequencies than the cubes with lower infill density. The latter samples maintain high transmitted intensities around the 39 kHz frequencies in stand orientation, while halving the intensity transmitted at 50 kHz.

The two normalised spectra in x and y-axis have a different shape: the first shows wider peaks than the second, as it can be easily observed from the analysis of cubes with 20% infill density (figure 6.16).

Table 6.7 Frequency at which more signal is transmitted depending on orientation in cubes with 15%, 20% and 60% zig-zag infill pattern density

	Orientation	**Maximum Peak Frequency (kHz)**
60%	STAND	49.286
	SIDE	39.063
	FRONT	39.063
20%	STAND	38.300
	SIDE	47.150
	FRONT	42.419
15%	STAND	39.978
	SIDE	36.621
	FRONT	37.842

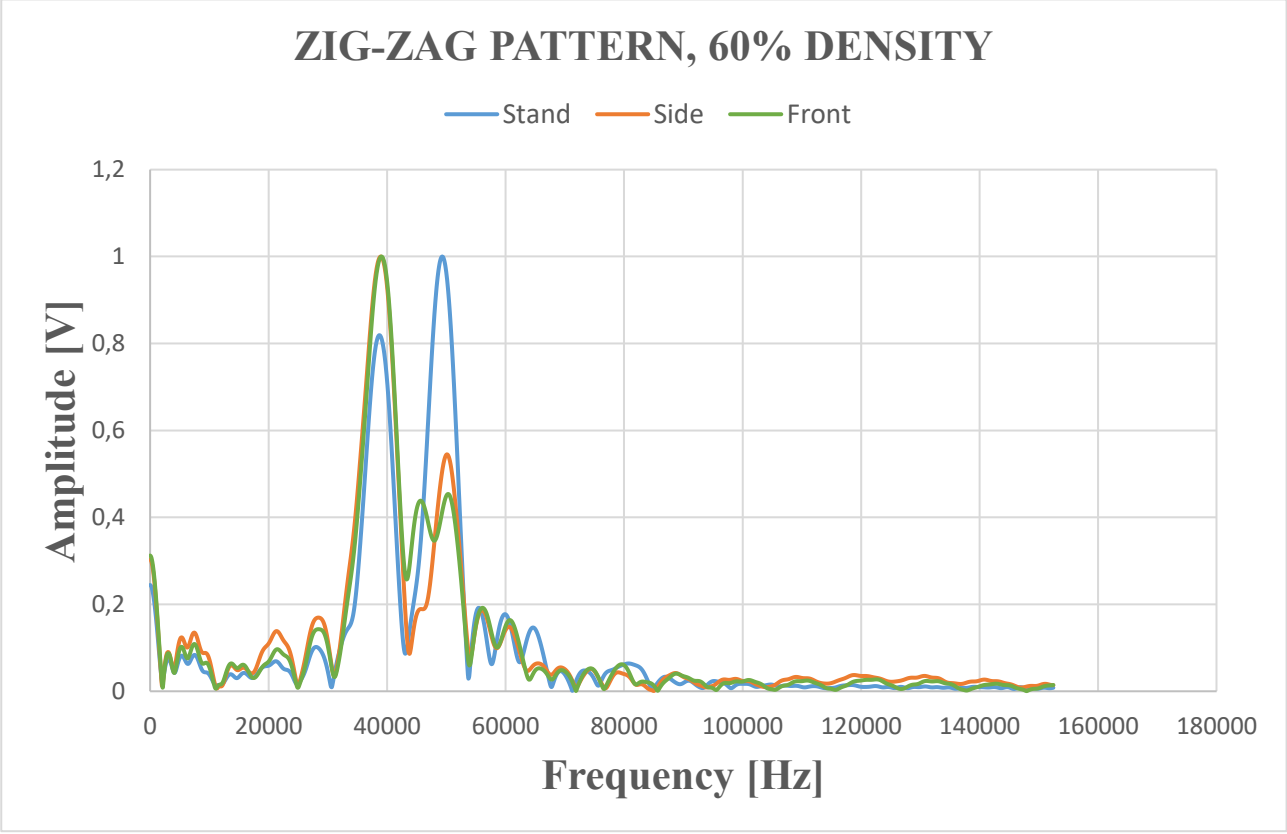

Figure 6.15 Normalised frequency spectra of the cubes with 60% zig-zag infill density in stand, side and front orientation

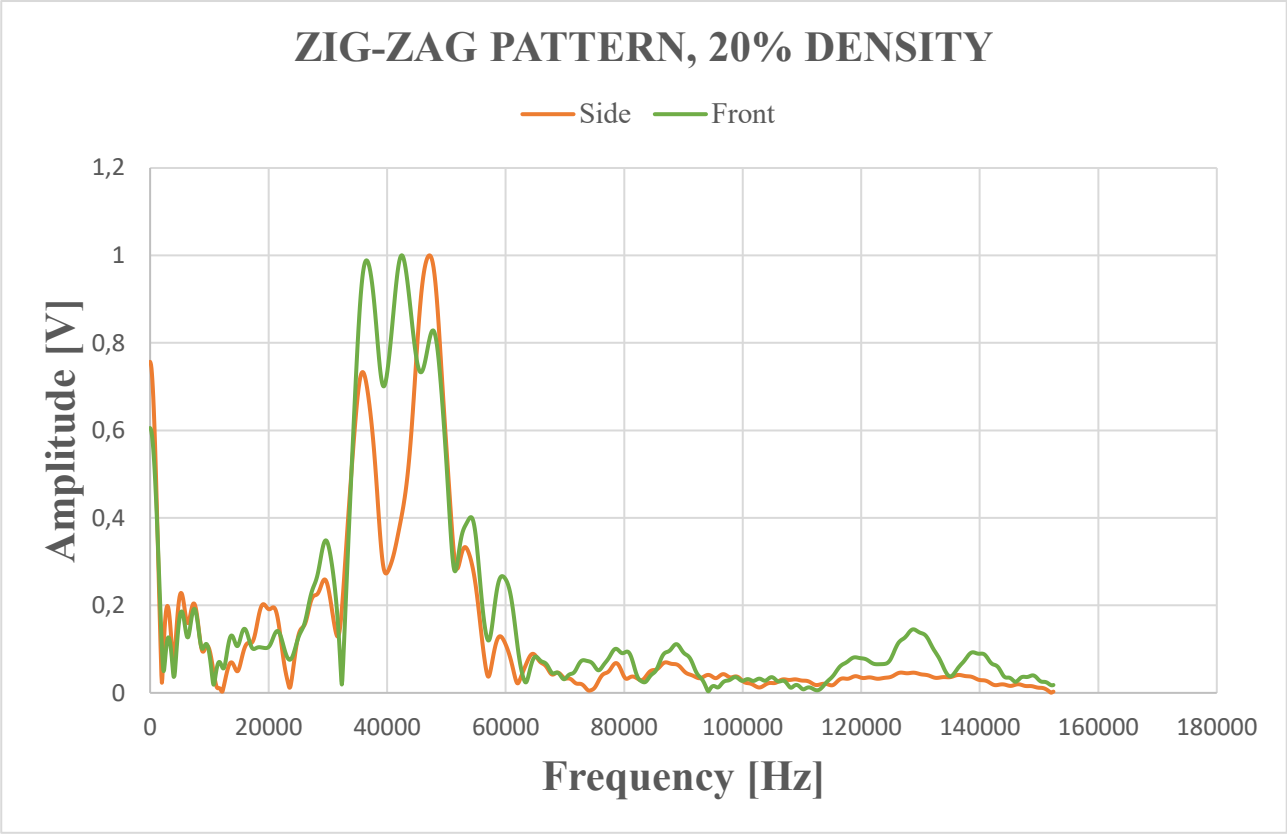

Figure 6.16 Normalised frequency spectra of the cubes with 20% zig-zag infill pattern in side and front orientation

6.4 Comparison of cubes of different patterns and densities

One of the aim of this work is to assess whether it is possible to distinguish the different infill patterns by comparing the ultrasound signals. Table 6.8 summarizes the ultrasound wave speed, signal shape and frequency spectrum characteristics for the cubes with 15% infill density.

Table 6.8 Comparison of signal data between cubes with different infill pattern ad 15% infill density

15%	Orientation	ToF_m (μs)	Δt (μs)	Ultrasounds speed, C_m (m/s)	Amplitude max. peaks (mV)	Peak-peak (mV)
CUBIC	STAND	214.2 similar	80 similar	1061.52 similar	4.4; -8.4	12.8
	SIDE	209.4 (208.8)	84.8 (85.4)	1216.48 (1239.09)	6; -11.2	17.2
	FRONT	208.6 similar	85.6 similar	1246.82 similar	7.6; -12.8	20.4
CONCENTRIC	STAND	205.4 similar	88.8 similar	1384.96 similar	64.8; -73.6	138.4
	SIDE	210.8 (213.4)	83.4 (80.8)	1166.8 (1084.55)	-1.6; -3.28	1.68
	FRONT	211.2 similar	83 similar	1153.35 similar	-1.84; -2.88	1.04
ZIG-ZAG	STAND	229.8 (226.6)	64.4 (67.6)	750.73 (798.69)	26.8; -42.4	69.2
	SIDE	212.8 (207.2)	81.4 (87)	1102.48 (1303.7)	2.88; -7.28	10.16
	FRONT	211.8 similar	82.4 similar	1133.73 similar	3.2; -7.76	10.96

The cubes with concentric infill analysed along the z-axis show the highest wave speed (ToF CU=214.2 μs; CONC=205.4 μs; ZZ=229.8 μs); the transmission is faster than that along x- and y-axis, differently than for the cubic and zig-zag infill pattern. The higher speed may be attributed to the wave encountering only vertical walls, along which the wave can penetrate faster, having a continuous path of material to travel.

As far as the absorbed energy is concerned, by observing the signal peaks, differences can be seen between the different patterns and orientations of the samples.

Looking at the maximum signal peak (figure 6.17), the CONC and ZZ patterns show a higher peak in the stand orientation, while the CU pattern in the same orientation shows the lowest peak.

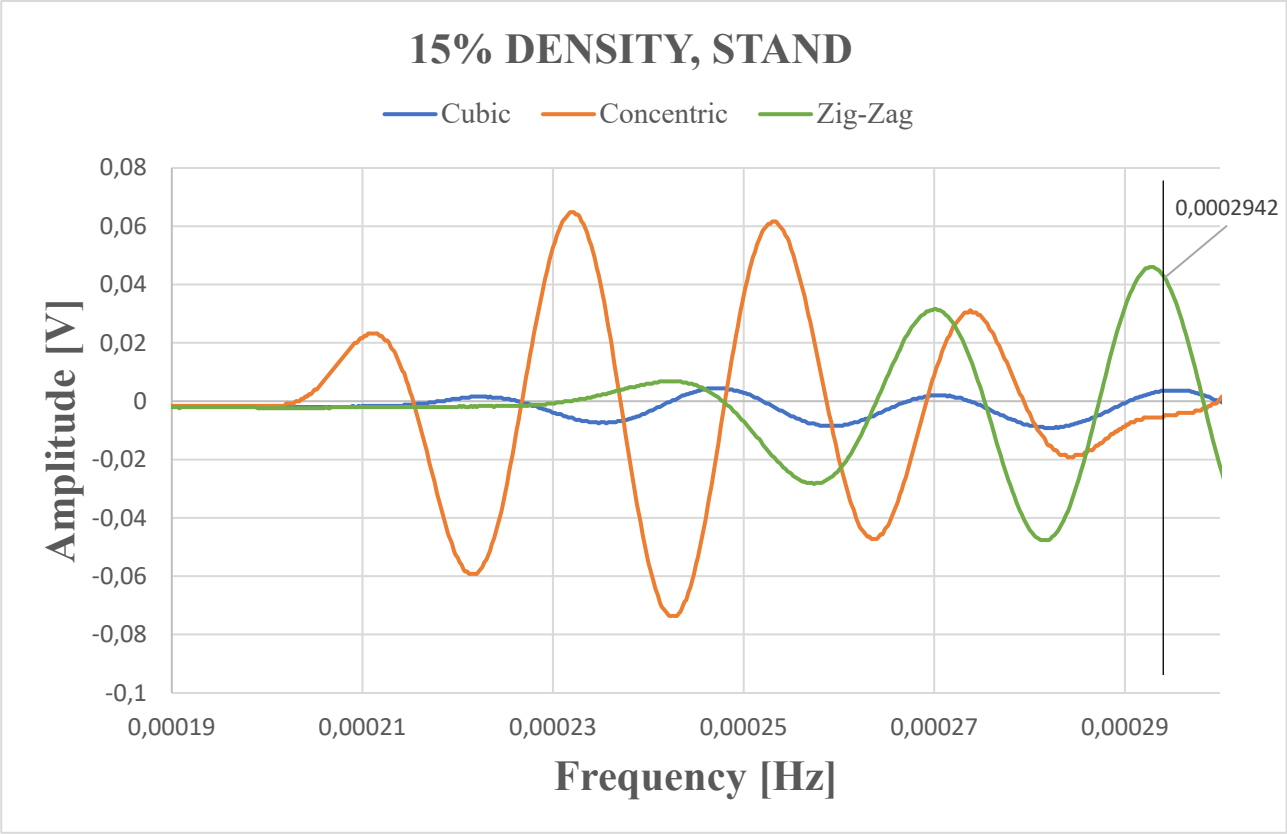

Figure 6.17 Ultrasound signals through cubes at 15% density in stand configuration, with cubic, concentric and zig-zag infill pattern

From figure 6.17, it can be seen that the number of peaks in the signal for the CU, CONC and ZZ configurations are 3, 4 and 2 respectively. This results in a higher transmission of high frequencies for the CONC configuration, as shown in figure 6.18.

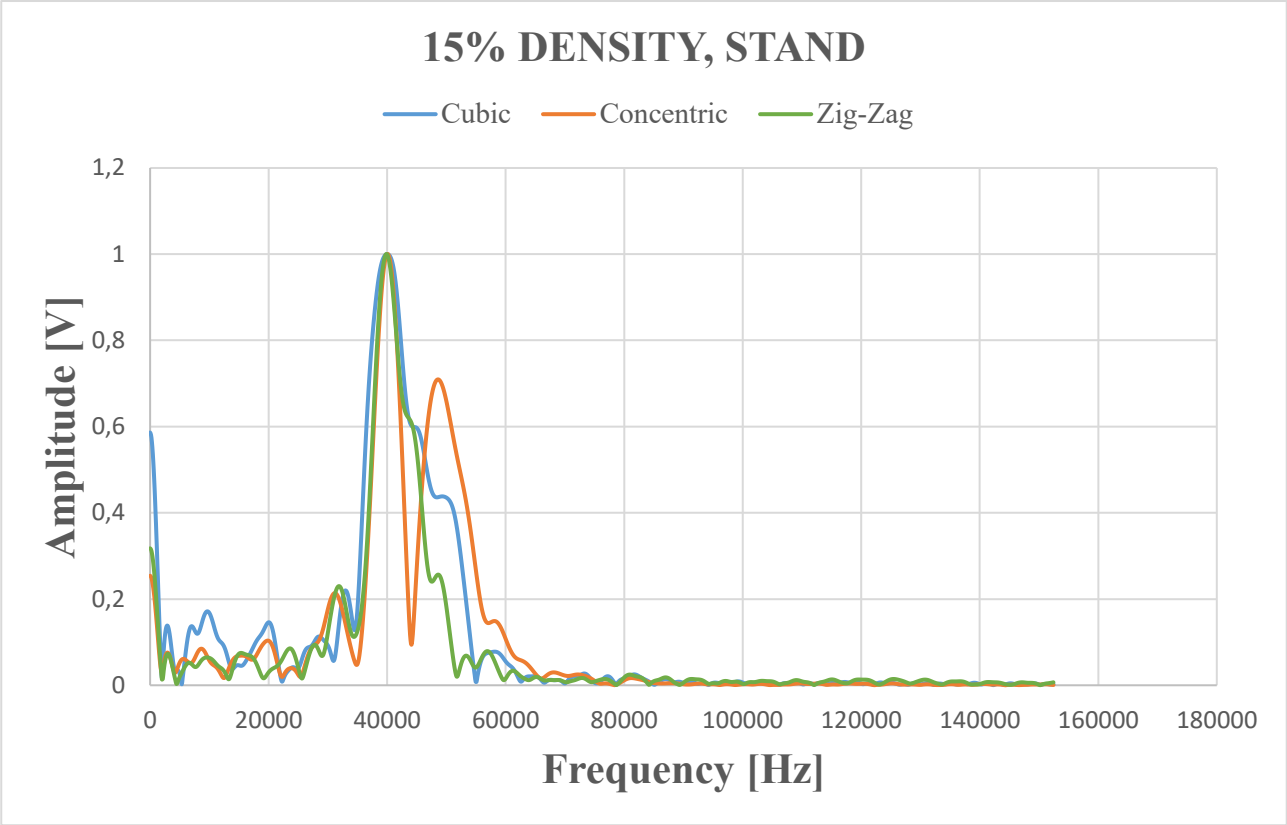

Figure 6.18 Normalised frequency spectra of the cubes in stand orientation, with cubic, concentric and zig-zag internal pattern and 15% infill density

When laid on their sides (side and front orientations), the cubes with cubic infill pattern (CU) differ from the stand orientation only by a few mV, demonstrating almost isotropic behaviour; the other two patterns, on the other hand, absorb much more in side and front than in the stand configuration.

With the concentric infill pattern (CONC), a non-isotropic behaviour is expected due to the internal geometry of the cube. Indeed, a difference of about 130 mV is detected in the amplitude of the highest peak between the standing and the two lying configurations. Similar attenuation is experienced by the cubes with zig-zag infill pattern (ZZ).

The influence of the infill density is evaluated by comparing samples with 15%, 20% and 60% infill density.

Table 6.9 Comparison of signal data between cubes with different infill pattern ad 20% infill density

20%	Orientation	ToF_m (μs)	Δt (μs)	Ultrasounds speed, C_m (m/s)	Amplitude max. peaks (mV)	Peak-peak (mV)
CUBIC	STAND	214 (213.4)	80.2 (80.8)	1067.19 (1084.55)	8.4; -18	26.4
	SIDE	208.8 similar	85.4 similar	1239.09 similar	10.8; -16	26.8
	FRONT	208.2 (209.2)	86 (85)	1262.56 (1223.93)	11.6; -17.6	29.2
CONCENTRIC	STAND	205.8 similar	88.4 similar	1366.04 similar	61.4; -69.6	131
	SIDE	211.6 (213)	82.6 (81.2)	1140.17 (1096.44)	-1.92; -3.28	1.36
	FRONT	211.2 (210.2)	83 (84)	1153.35 (1187.59)	-1.92; -3.36	1.44
ZIG-ZAG	STAND	222.8 similar	71.4 similar	864.27 similar	67.2; -76	143.2
	SIDE	212.6 (211.4)	81.6 (82.8)	1108.6 (1146.73)	14.8; -20.4	35.2
	FRONT	215.4 (216.4)	78.8 (77.8)	1028.76 (1002.97)	18.6; -23.4	42

Table 6.10 Comparison of signal data between cubes with different infill pattern ad 60% infill density

60%	Orientation	ToF_m (μs)	Δt (μs)	Ultrasounds speed, C_m (m/s)	Amplitude max. peaks (mV)	Peak-peak (mV)
CUBIC	STAND	209.2 similar	85 similar	1223.93 similar	24.4; -34	58.4
	SIDE	207 similar	87.2 similar	1312.26 Similar	20; -28	48
	FRONT	206.6 similar	87.6 similar	1329.71 similar	19.6; -27.2	46.8
CONCENTRIC	STAND	204 similar	90.2 similar	1455.51 similar	25.2; -30	55.2
	SIDE	226.4 similar	67.8 similar	801.9 similar	-1.36; -4	2.64
	FRONT	232.2 (229.6)	62 (64.6)	718.37 (753.55)	-1.52; -3.2	1.68
ZIG-ZAG	STAND	210.6 similar	83.6 similar	1173.65 similar	40.8; -48	88.8
	SIDE	212 (213.2)	82.2 (81)	1127.34 (1090.46)	26.8; -36.4	63.2
	FRONT	213.2 similar	81 similar	1090.46 similar	28; -38	66

With higher infill density, the speed of the ultrasound waves within the samples follows the trends described before: the fastest speed is achieved for a stand orientation of the CONC cubes, while the CU cubes result in the slowest speed. The ZZ cubes follows the previous trends at 20% density, but they behave like the CONC cubes at 60% density.

The maximum peak amplitude is maintained along the z-axis for the CONC and ZZ patterns; the CU pattern has opposite behaviour at lower densities, yet it aligns to the other patterns at 60% density.

Comparing the same orientations for the CU pattern at 15%, 20% and 60% density, both the speed of ultrasound wave and the energy content is higher for a higher density.

The CONC and ZZ patterns, on the other hand, show a particular behaviour.

The CONC pattern results in higher speed with a higher density along the z-axis, while along the x- and y-axis the speed decreases significantly.

In the cubes with the ZZ pattern, the ultrasounds increase their speed with increasing density only along the z-axis; along the other two orientations there is no significant change.

These trends are to be attributed to the internal geometry of these two configurations. Along the z-axis, they develop continuous air chambers divided by parallel walls through which the ultrasounds travel. In the ZZ model, this clearly occurs along the z-axis, only in the higher density and this can be clarified by looking at the figure 6.19.

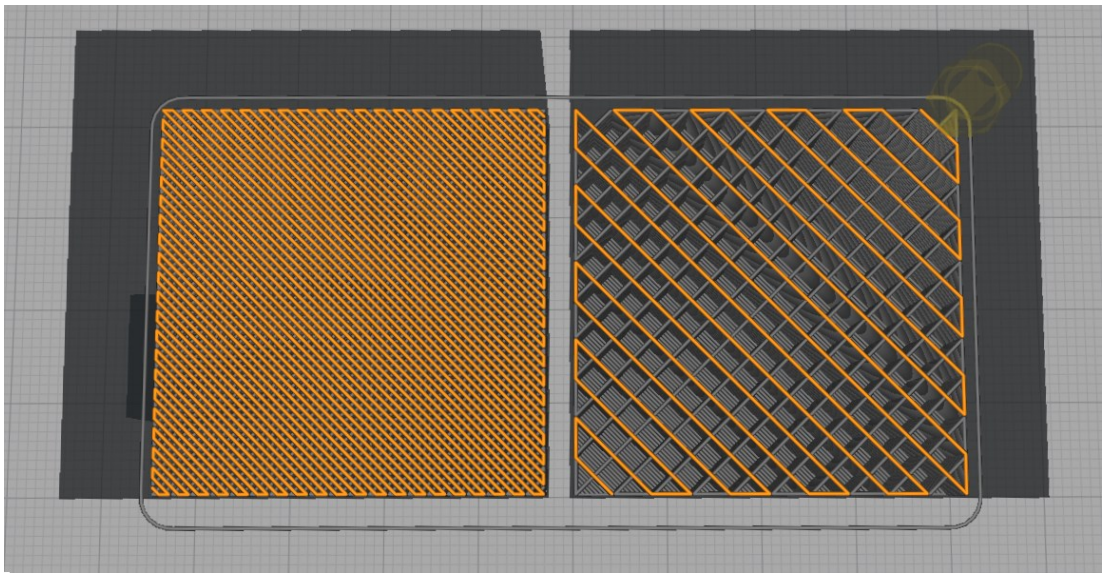

a.

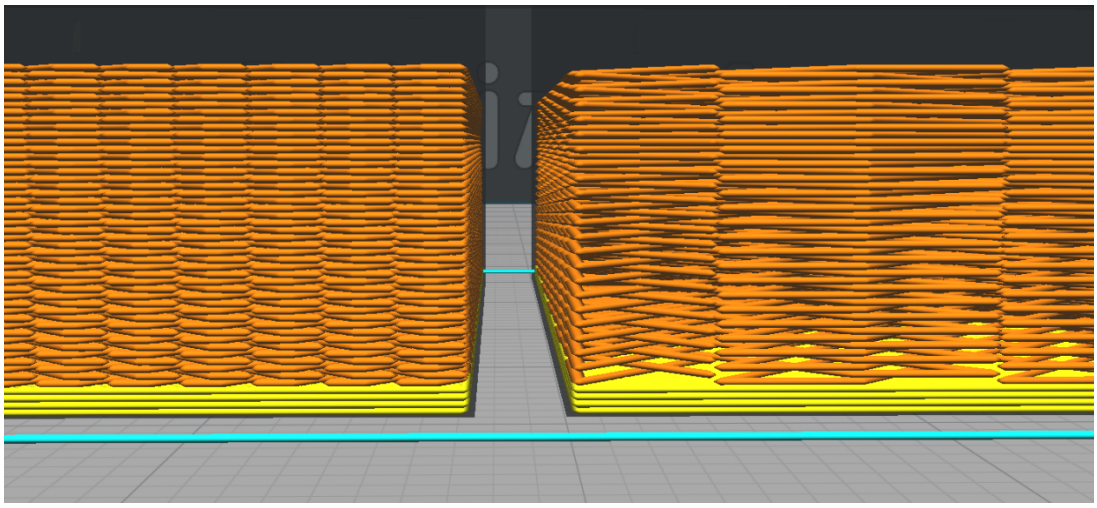

b.

Figure 6.19 Cubes with internal zig-zag pattern, 60% density (left) and 20% density (right), a. top view, b. front view

The explanation may lie in the fact that the layers of the ZZ model repeat themselves alternately, so at high density there are more contact points between two consecutive layers, building up like columns.

6.5 Analysis of 40x20x40 mm samples

Another set of samples studied are 40x20x40 mm 3D components printed with PLA, with 15% infill density and different internal configurations, respectively cubic, lines, triangles and grid (figure 6.20).

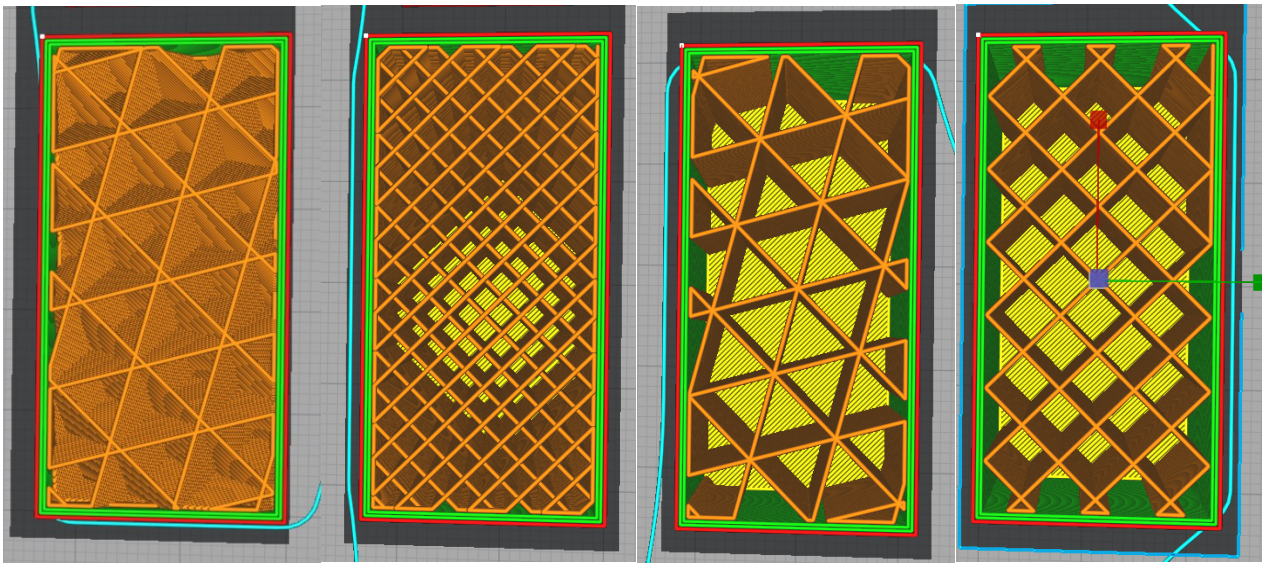

Figure 6.20 Samples with 15% infill density with cubic, lines, triangles and grid internal pattern (from left to right)

As with the cubes, the influence of different infill patterns on sound propagation through these samples was studied. Table 6.11 shows the collected data.

Table 6.11 Data of ultrasound signals passing through the samples in 3 different orientations: 40 mm along the x- and z-axis, 20 mm through the y-axis

		ToF (µs)	Δt	Speed (m/s)	Amplitude peaks (mV)	Peak-peak (mV)
CUBIC	STAND	204.2	86.2	1335.07	0.8; -6	6.8
	SIDE	200.6	89.8	1517.40	1; -8.6	9.6
	FRONT	248.2	42.2	1259.41	5.6; -17.4	23
LINES	STAND	204.2	86.2	1335.07	0.8; -12.6	13.4
	SIDE	203.6	86.8	1362.36	0; -6	6
	FRONT	252	38.4	1016.24	0.88; -7.36	8.24
TRIANGLES	STAND	202.6	87.8	1410.39	24.8; -35.2	60
	SIDE	200.2	90.2	1540.78	1.84; -7.36	9.2
	FRONT	247.4	43	1326.22	2.8; -7.84	10.64
GRID	STAND	203.4	87	1371.70	44; -60	104
	SIDE	202.2	88.2	1430.57	3; -12.2	15.2
	FRONT	251	39.4	1070.64	1.04; -4.08	5.12

Before placing the samples between the probes, the receiver measured the time of flight of the ultrasounds and their speed through the air: ToF_a = 290.4 µs and C_a = 344.35 m/s.

In previous experiments, it was concluded that the internal structure influences the way the ultrasounds propagate. In fact, triangles and grid models have a similar structure, and such is also the behaviour of the speed along the longer sides, which is higher on the side orientation. All models respect this peculiarity; however, the triangles infill pattern can be distinguished by a higher ultrasonic speed through the sample in all orientations.

The lines infill pattern appears similar to the triangles and grid ones, yet it behaves differently. In fact, the material is not deposited for each layer in the same position, but the sequence is repeated in alternating layers. This results in a more complex internal structure and a slight irregularity in the shape of the second peak. The difference in shape allows to distinguish it from a cubic infill pattern which shows the same ultrasound speed in stand orientation (figure 6.21).

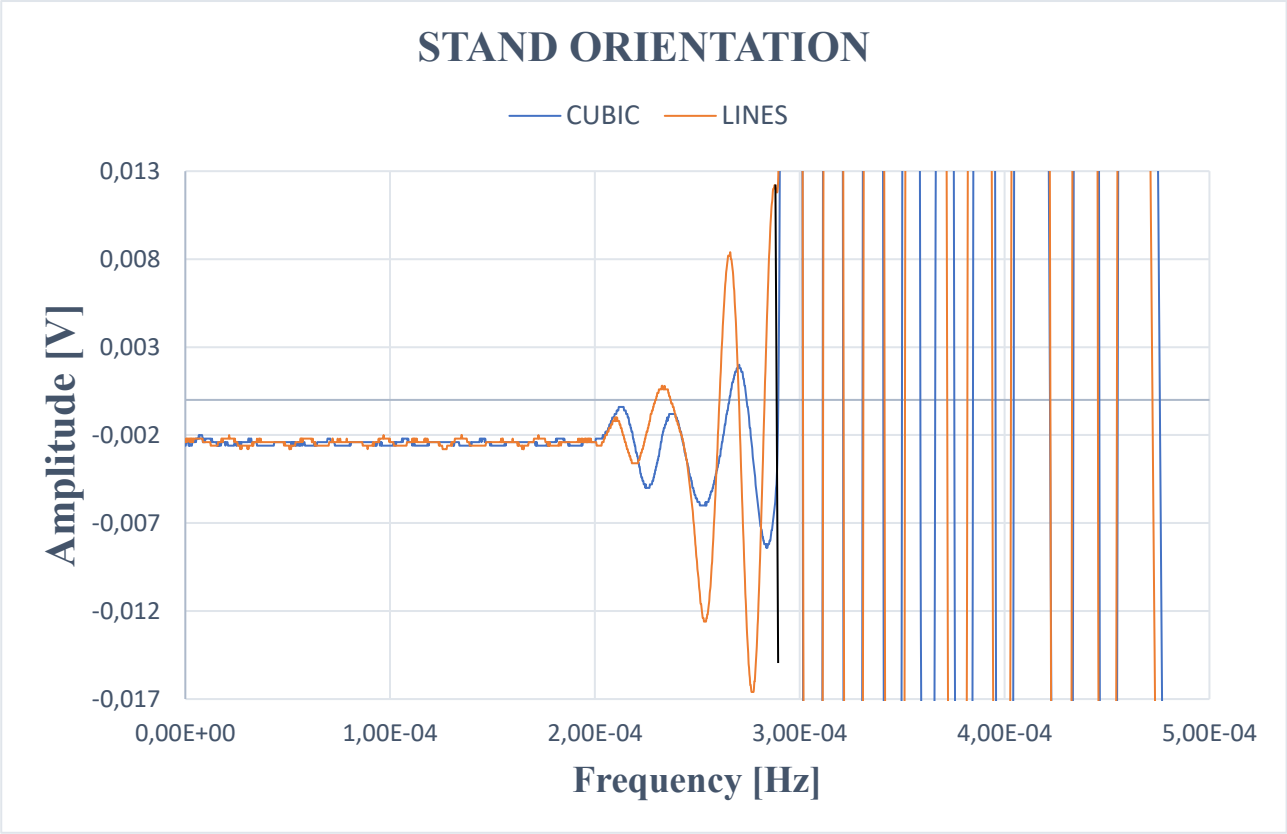

Figure 6.21 Ultrasounds signals of cubic and lines patterns in stand orientation

From the normalised frequency spectra, it appears that cubic and lines pattern transmit mostly around 40kHz (while the grid pattern has the highest peak around 47kHz). However, in the cubic pattern the transmission at high frequencies remains high (figure 6.22).

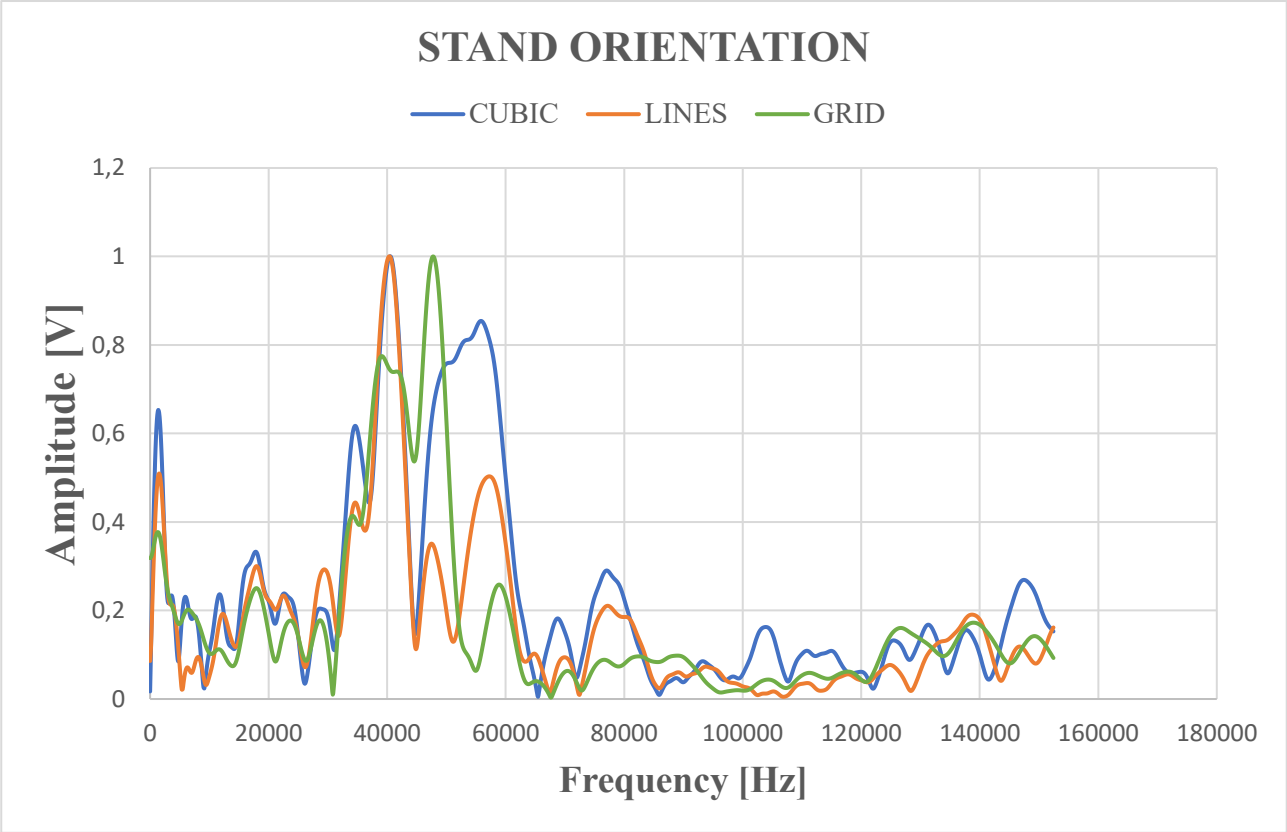

Figure 6.22 Normalised frequency spectrum of cubic, lines and grid samples in stand orientation

6.6 Internal defects

In this case, three samples were analysed, i.e., three 40x40x40 mm PLA cubes with 15% cubic infill density, two of which had an induced defect in the centre (figure 6.23).

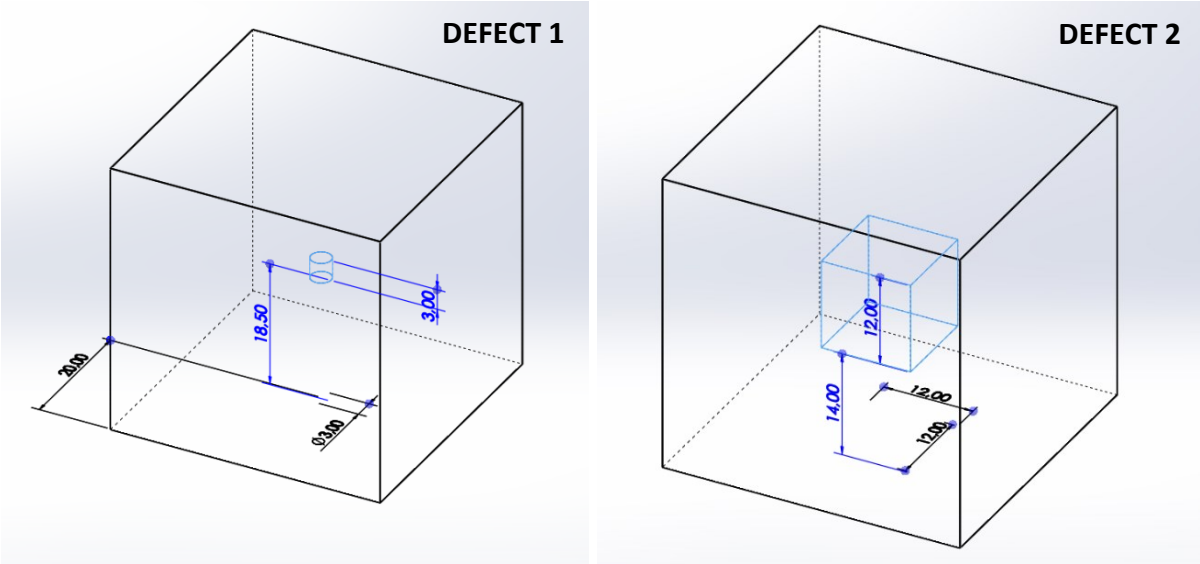

Figure 6.23 3D drawings of the defective cubes. “Cube defect 1” with a cylinder of 3 mm in diameter and 3 mm high (left) and “Cube defect 2” with a cube of side 12 mm (right)

The time of flight of ultrasounds in air and their speed are ToF_a= 290.6 µs, C_a= 344.11 m/s, for the “flawless” cube and the “defect 1”, ToF_a= 291.4 µs, C_a=343.17 m/s for “defect 2”.

Table 6.12 Signal data of the three different cubes

CUBE FLAWLESS 15% CUBIC	**ToF (µs)**	**Δt**	**Speed (m/s)**	**Amplitude peaks (mV)**	**Peak-peak (mV)**
STAND	209	81.6	1154.67	8; -13.2	21.2
SIDE	204.8	85.8	1313.98	12.8; -20.2	33
FRONT	204.2	86.4	1340.40	12.4; -18.2	30.6
CUBE DEFECT 1 15% CUBIC					
STAND	209.4	81.2	1141.49	5.2; -10.4	15.6
SIDE	204.2	86.4	1340.40	10.6; -18.6	29.2
FRONT	204.6	86	1322.67	9.2; -16.8	26
CUBE DEFECT 2 15% CUBIC					
STAND	208.6	82.8	1184.82	4.6; -11.4	16
SIDE	203.4	88	1400.54	6.6; -11.4	18
FRONT	204.2	87.2	1362.38	6; -10.6	16.6

In the cubes in stand orientation, there is a slight difference in the height of the peaks, but the shape of the signal is similar. The cube with the largest defect is traversed by the ultrasound faster, even if only slightly, and also has a wider frequency spectrum, but all three transmit most energy around 45 kHz (figure 6.24).

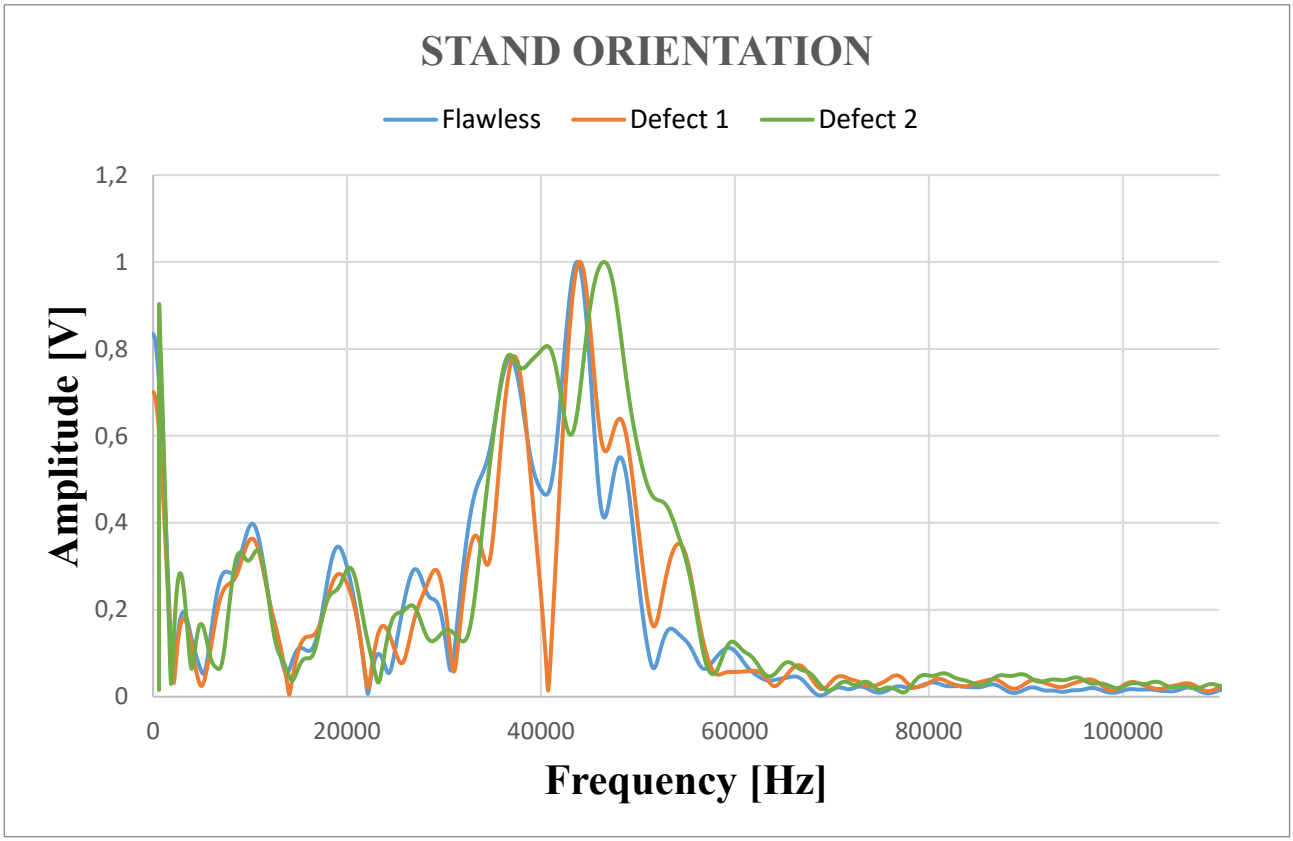

Figure 6.24 Normalised frequency spectrum along the z-axis of the three tested cubes

Along the x-axis, however, they transmit more around 39 kHz, and it is the flawless cube that has the widest spectrum, while the other two are similar. Again, the shape of the signal is similar between them.

The same happens with the 'front' orientation, the shapes of the signals in time, and frequency spectra are similar between the samples, slightly wider is the spectrum of the sample with the largest defect.

It can be seen, therefore, that with this technique it is difficult to discriminate defects that are not large in size. That is, as the wave frequency used by ultrasound probes is small, 50kHz, the corresponding wavelength is in the range of 6-8mm. This is therefore too high to be able to identify smaller features.

6.7 ABS samples and Ultimaker printers

Analyses were also performed on sample printed with different materials and printers. In this test, two 40x40x40 mm cubes were compared, with the same cubic infill pattern and 20% density; the first was printed with PLA on Ultimaker s3, while the second was produced with ABS on Ultimaker s5. A different material requires different slicing parameters to be selected in the slicing software. The same top/bottom and side wall thicknesses were set (at 0.8 mm) for both samples.

The registered time of flight of the ultrasound in air is ToF_a = 290.8 μs with a speed of C_a = 343.88 m/s.

Table 6.13 Data of ultrasound signals passing through PLA and ABS samples at 20% density

CUBIC CUBE 20%		**ToF (μs)**	**Δt**	**Speed (m/s)**	**Amplitude peaks (mV)**	**Peak-peak (mV)**
PLA	STAND	210.4	80.4	1113.60	13.4; -24.2	37.6
	SIDE	205.8	85	1277.15	17; -22.6	39.6
	FRONT	205.4	85.4	1293.67	15.2; -21.8	37
ABS	STAND	215.2	75.6	982.33	16; -22.6	38.6
	SIDE	211.2	81.2	1089.33	20.2; -25	45.2
	FRONT	210.2	80.6	1119.83	18.6; -25	43.6

Comparing the samples along the same axis, what emerges is that the ultrasounds travel faster in the PLA sample (figure 6.25).

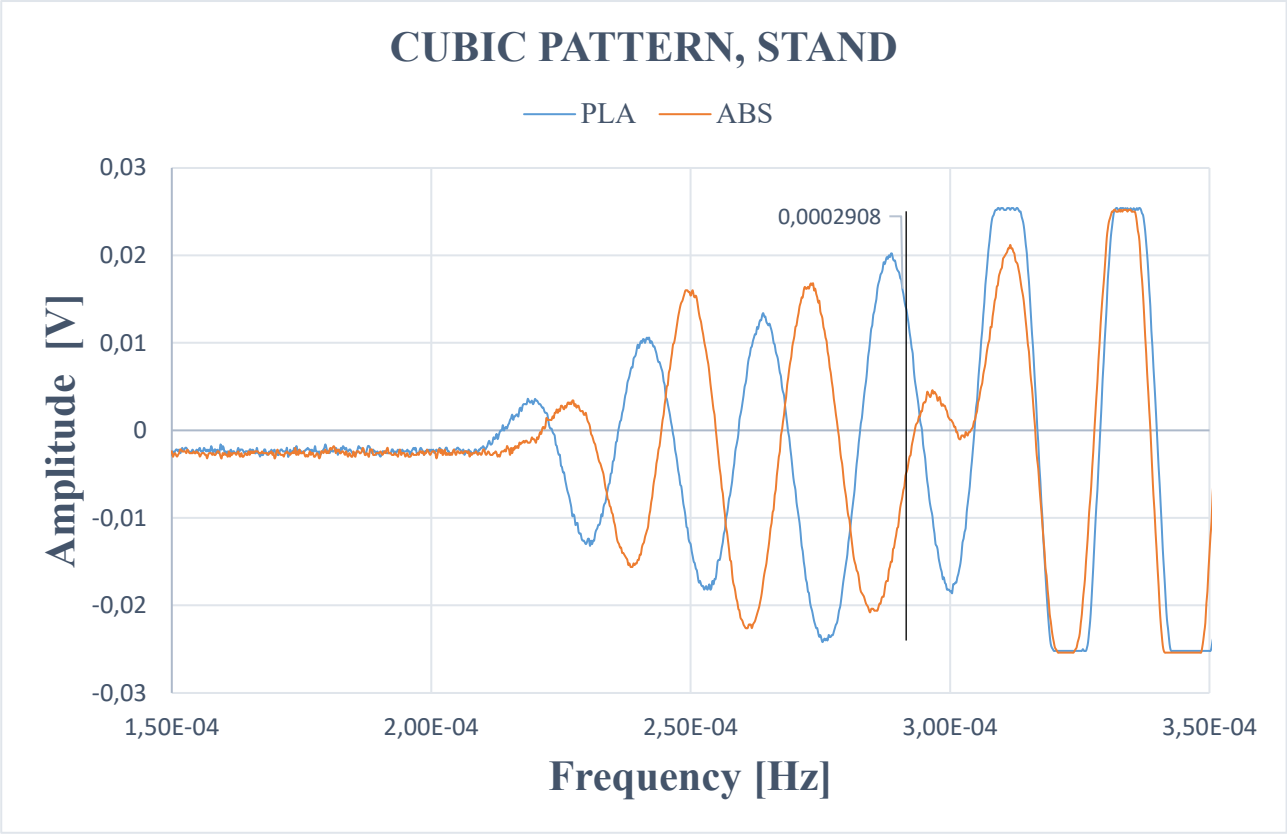

Figure 6.25 Ultrasounds signals passing through the z-axis of PLA and ABS samples

It is interesting to confirm that the infill pattern has a distinct behaviour that repeats in the two samples irrespective of the material. In fact, the speed increases similarly in the two samples when moving from the stand orientation to the side and front orientations, which are roughly similar to each other. The 'side' and 'front' orientations are therefore traversed faster by the ultrasounds.

As with the PLA cubes, the normalised frequency spectrum can also be observed for the ABS cubes in order to understand the internal orientation. They all transmit more energy around 39 kHz, but along the x-axis the spectrum is widest while it is narrowest along the y-axis (figure 6.26 and 6.27), following the same behaviour as the PLA cube.

Table 6.14 Frequency at which more signal is transmitted depending on orientation, in PLA and ABS samples with 20% cubic infill density

CUBIC CUBE 20%	Orientation	Maximum Peak Frequency (kHz)
PLA	STAND	40.588
	SIDE	37.689
	FRONT	39.215
ABS	STAND	37.689
	SIDE	40.741
	FRONT	40.741

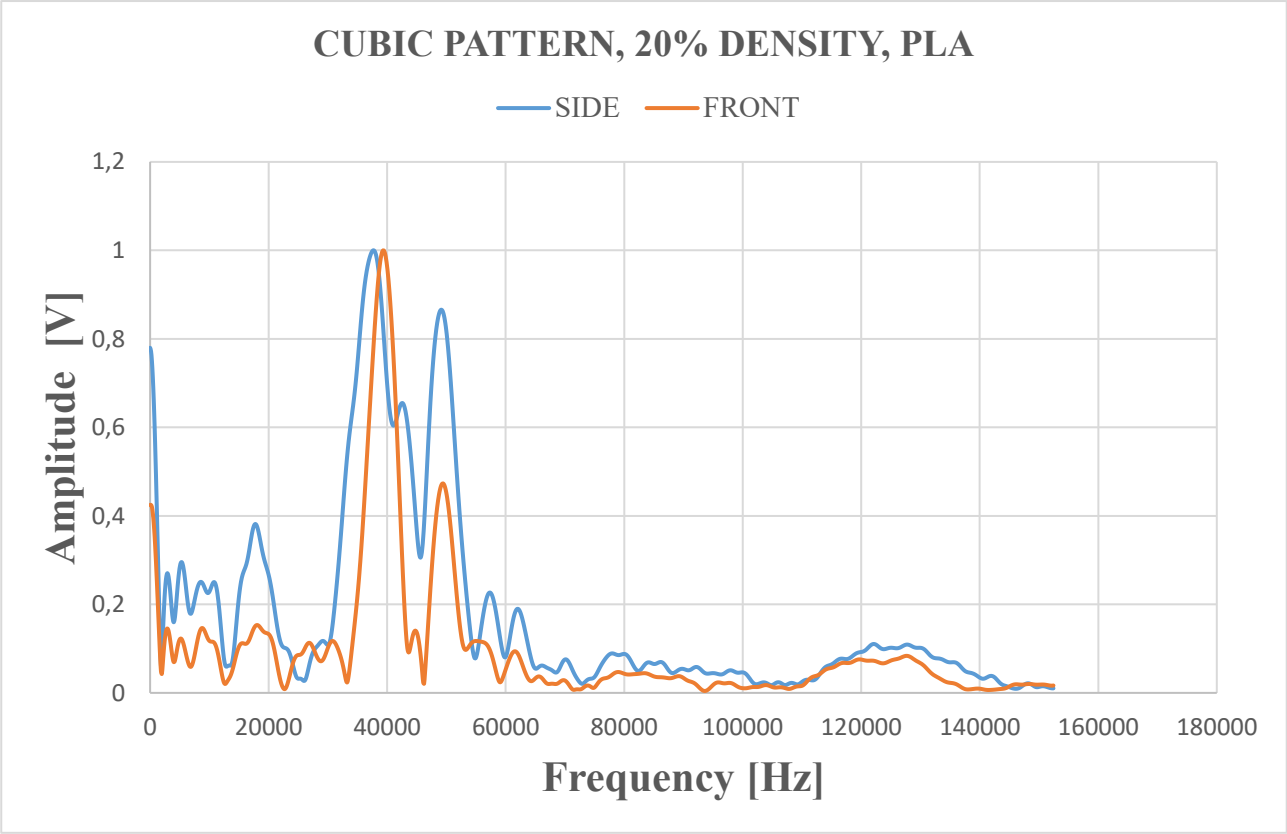

Figure 6.26 Normalised frequency spectrum of the PLA cube along the x and y axes of the sample

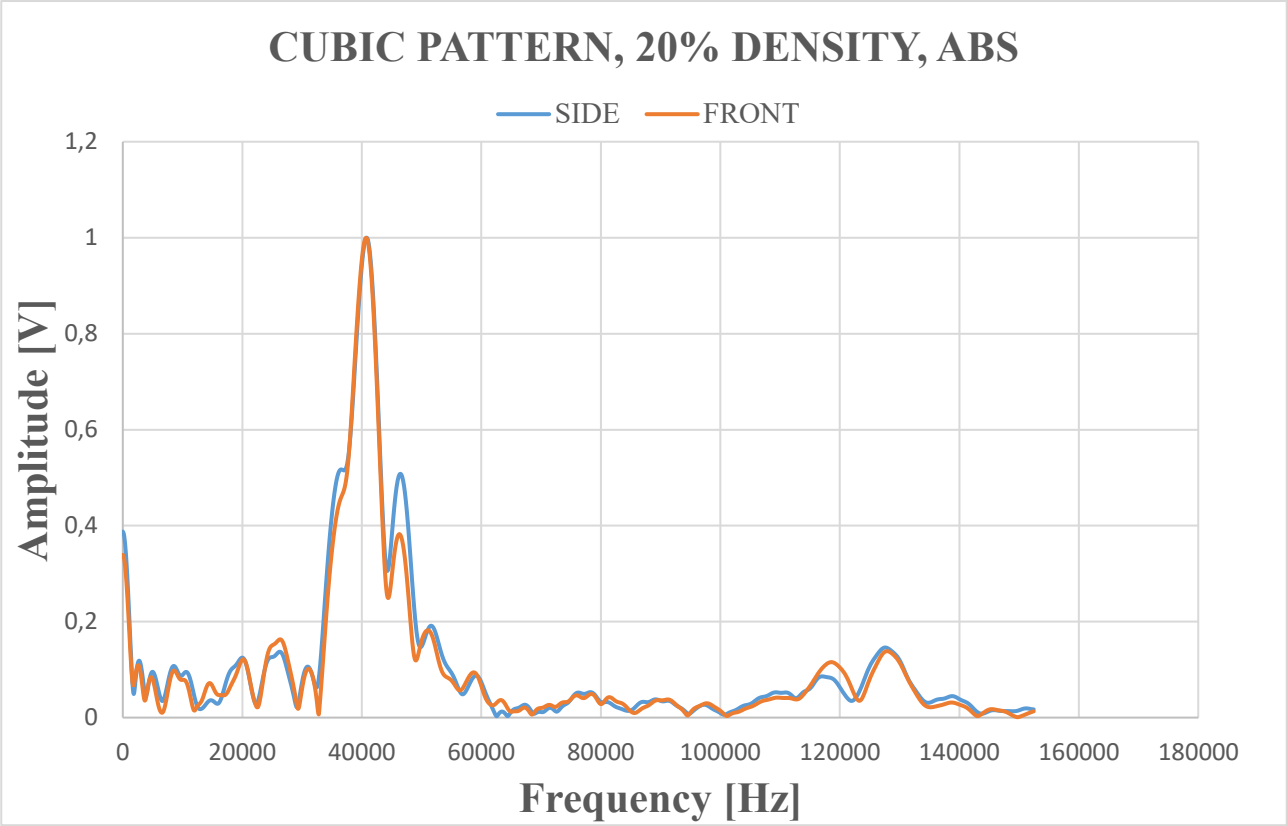

Figure 6.27 Normalised frequency spectrum of the ABS cube along the x and y axes of the sample

It can therefore be concluded that ultrasound travels with different velocities in the two materials, which, however, show the same variations with this pattern along the x, y and z axes.

6.8 ABS samples and Stratasys Dimension Elite printer

An ABS cube printed with the Ultimaker s5 printer (sample 1), was compared with one printed with the Stratasys Dimension Elite (sample 2). The latter, as mentioned in chapter 5, can make high density, intermediate density or low density parts. The sample 2 was made with low density, set using the slicing software CatalystEX, which corresponds approximately to the 20% infill set with Cura software. The pattern chosen in Cura for the sample made with Ultimaker s5 is the zig-zag pattern which corresponds to that used by the Dimension Elite industrial printer.

The time of flight of the ultrasound in air without sample was ToF_a = 290.8 µs with speed C_a = 343.88 m/s

Table 6.15 Time of flight, ultrasonic speed and signal peaks in PLA and ABS cubes

ZIG-ZAG CUBE 20%	Orientation	ToF (µs)	Δt	Speed (m/s)	Amplitude peaks (mV)	Peak-peak (mV)
ABS Ultimaker s5	STAND	230.6	60.2	712.76	60.8; -68.8	129.6
	SIDE	218.8	72	902.53	20.8; -25.6	46.4
	FRONT	216.2	74.6	958.78	21.4; -24.8	46.2
ABS Dimension Elite	STAND	244.2	46.6	573.73	4.8; -24	28.8
	SIDE	211.4	79.4	1083.43	8.2; -14	22.2
	FRONT	212.6	78.2	1049.33	8.6; -14.2	22.8

From the results obtained (table 6.15), it appears that in both samples the ultrasound speed increases when moving from the stand orientation to the side and front orientations. Along the z-axis, the ultrasounds travel faster in sample 1, while in the other two directions they travel faster in sample 2.

Analysing the frequency spectrum obtained with the FFT, a more detailed comparison is carried out to see if a distinction is possible between the two samples.

In all orientations, the spectrum from sample 2 appears wider (figure 7.28). For both sample 1 and 2, the spectrum along the x-axis is wider than that along the y-axis.

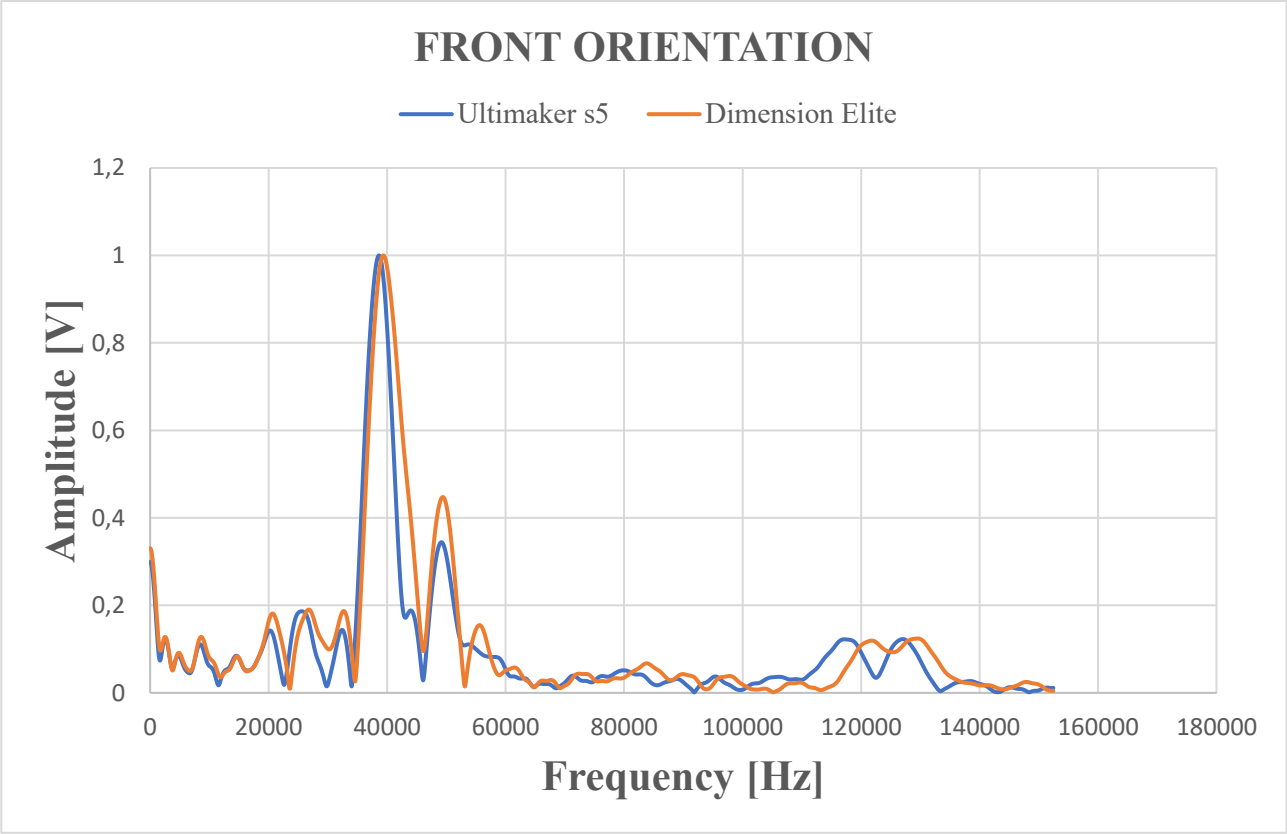

Figure 6.28 Normalised frequency spectrum of sample 1 and sample 2 along the y-axis.

In any case, this pattern once again revealed a certain anisotropy between the stand orientation and the others. In fact, along the z-axis, it was reconfirmed to be the direction traversed most slowly by the ultrasound, as was also the case in the experiments in Chapter 6 with the PLA sample.

Chapter 8

Conclusion

The aim of this work is to study the influence of the internal structure of 3D printed objects and their material on the propagation of ultrasound.
In particular, two different feedstock materials (PLA and ABS) and three different 3D printers were employed to produce the samples.

It turned out that the initial questions, whether it was possible to find a relationship between ultrasound signal and internal pattern, could be answered, even though in some cases the signal obtained is affected by noise; this, together with some limitations of the available technology, does not allow to distinguish very small variations and defects in the internal structure of the material. Only one type of probe emitting at 50 kHz was employed in the tests; the choice of frequency should be informed by the type of analysis to be performed and may not be suitable, for example to detect induced internal defects.

The use of ultrasounds to analyse 3D printed objects, however, proved its worth for the intended purpose.
The defects that occurred during the printing process added greater disturbance and resulted in some anomalies in the signal, however, it was their influence on ultrasound propagation that allowed to detect them, proving the validity of this technique to highlight such defects.
The response of the ultrasounds varies with different infill patterns as well as with different infill densities, but the different patterns result in different trends.
By analysing the signal obtained after data processing, it is possible to distinguish between the different internal patterns of the samples. The shape and intensity of the signal can therefore be correlated with the infill pattern and density of the samples.

To our knowledge, this is one of the first systematic studies on ultrasound analysis of 3D printed components; the results are encouraging and bode well for a fast, non-destructive analysis of such products. Implementation of specific algorithms that recognise different waveforms and frequency spectra would allow not only for comparison but also for proper identification of infill pattern and density as well as printing direction, and to a more effective discovery of defects.

Appendix A

Velocity of ultrasounds

At first, the velocity of ultrasonic waves in samples of massive material were measured, and this is done by measuring the time of flight, that is, the time it takes for the sound to pass through the sample.

Methods and setup

The ultrasonic measurements were carried out on massive samples of aluminium, stainless steel, carbon steel, acrylic and nylon. The samples consist of rectangles made up of a sequence of square steps (30x30 mm) with thickness increasing from 2.5 mm to 12.5 mm in increments of 2.5 mm each (figure A.1a).

Measurements were performed with OLYMPUS probes with a circular aperture (diameter of 12.7 mm) and a flat radiating surface. Three of these generate compression waves with a nominal frequency of 5 MHZ, 2.25 MHZ and 1 MHZ, and one shear wave at 5 MHz (figure A.1b).

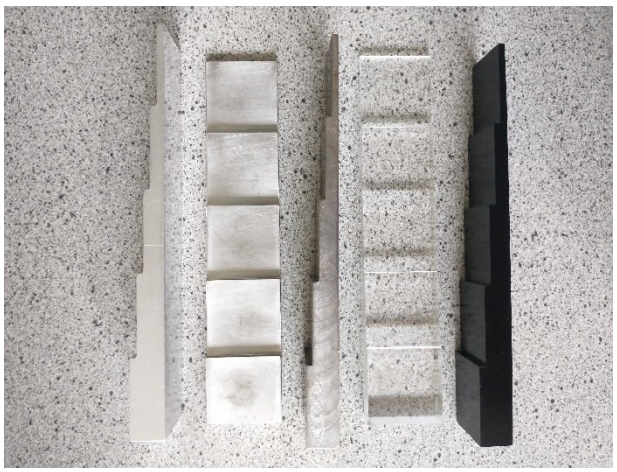

a

b

Figure A.1a Samples with increasing thickness steps. Aluminium, stainless steel, carbon steel, acrylic and nylon from left to right

A.1b from left to right 5MHz, 2.25MHz and 1MHz compression waves probes and 5MHz transverse waves probe

The signal collected by the probe is sent, via the same channel acting as transmitter/receiver, to the Tektronix TDS 210 oscilloscope (figure A.2), after it has been amplified and filtered by the Panametrics-NDT 5800 pulser/receiver.

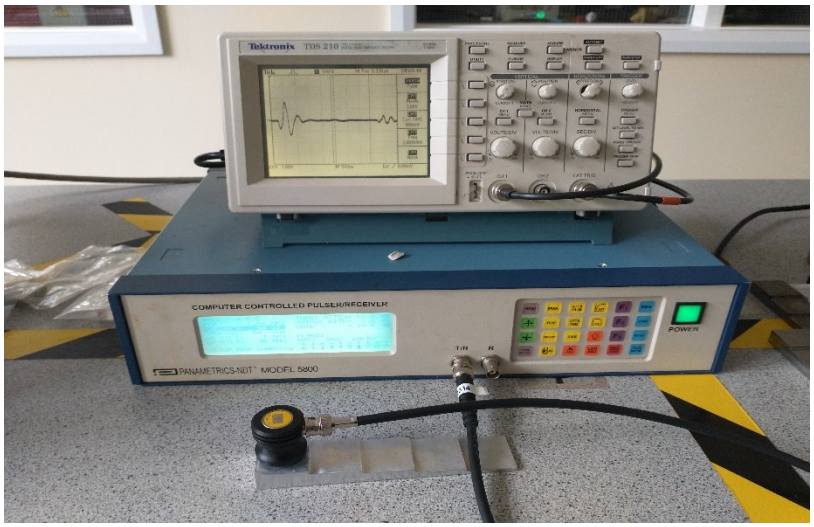

Figure A.2 Pulser/receiver and oscilloscope used to collect and elaborate the signal

Pulse-echo testing

The transducers worked in pulse-echo mode, transmitting the ultrasound into the samples via a coupling fluid (honey for shear waves) and receiving the echo of the signal from the back wall of the sample. The measured time of flight, ToF (t_s), of the wave gives the possibility of calculating the speed of sound (c), knowing the thickness (t) of the sample with the formula (A.1):

$$c = \frac{2t}{t_s} \tag{A.1}$$

In it, the thickness is multiplied by 2 because in the pulse-echo technique the sound travels twice the thickness of the sample before reaching the receiver. The speed of sound is characteristic in each material, which makes it a discriminating factor in the material itself, allowing the quantity and size of defects in it to be calculated during inspections [96].

Table A.1 shows the ToF of the compression sound waves generated with the 5MHz probe in each step of the aluminium sample. From the time of flight, the speed of the waves in the aluminium was calculated, knowing the thickness passed through.

Table A.1 Time of flight and speed of ultrasound in different thicknesses of an aluminium sample

Thickness step [mm]	ToF [µs]	Speed $\left[\frac{m}{s}\right]$
12.5 mm	3.89	6426.74
10 mm	3.11	6430.87
7.5 mm	2.34	6410.26
5 mm	1.55	6451.61
2.5 mm	0.77	6493.51

The oscilloscope digitises the signal, displays it on its screen and stores it. This can then be loaded into Matlab and processed further.

Figure A.3 shows an example of the time course of the ultrasonic signals through two different thicknesses of the aluminium sample. It can be seen that the time interval between two successive peaks corresponds to the ToF presented in table A.1.

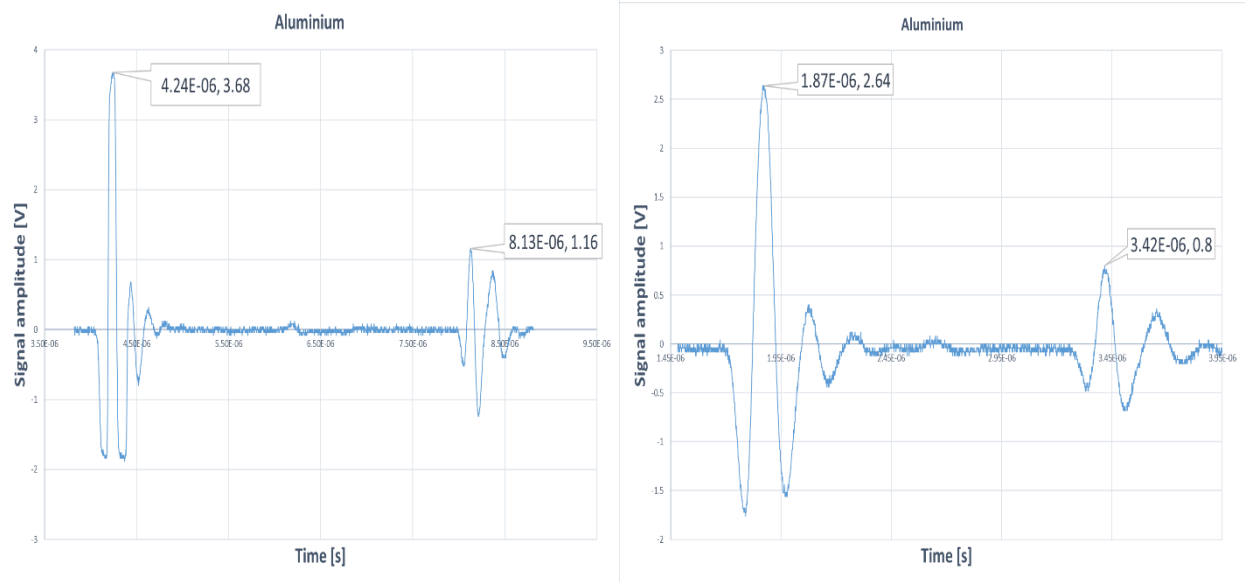

Figure A.3 Signal versus time trend in the aluminium sample, 12.5 mm step (left) and 5 mm step (right). Compression ultrasonic waves generated with 5 MHz probe.

All the samples described in this Appendix were tested with the probes listed in the same paragraph, and the data demonstrate the validity of the instrumentation and methodology.

The velocities obtained in these samples, in fact, are those characteristic of ultrasonic propagation in these materials [97], [98], as shown in table A.2. The tests also showed that the speed of the transverse waves was about half the speed of the longitudinal waves, as expected.

Table A.2 Speed of ultrasonic propagation in test sample materials (step 7.5 mm, probe 5 MHz)

Material	Speed of sound expected $\left[\frac{m}{s}\right]$	Speed of sound measured $\left[\frac{m}{s}\right]$	Shear speed of sound measured $\left[\frac{m}{s}\right]$
Aluminium	6300	6355	3165
Stainless steel	5900	5725	3164
Carbon steel	5920	5952	3304
Acrylic	2750	2767	1394
Nylon	2600	2396	No signal

The signals of nylon, acrylic and carbon steel, samples are also shown in figure A.4 which confirm the ultrasound velocity.

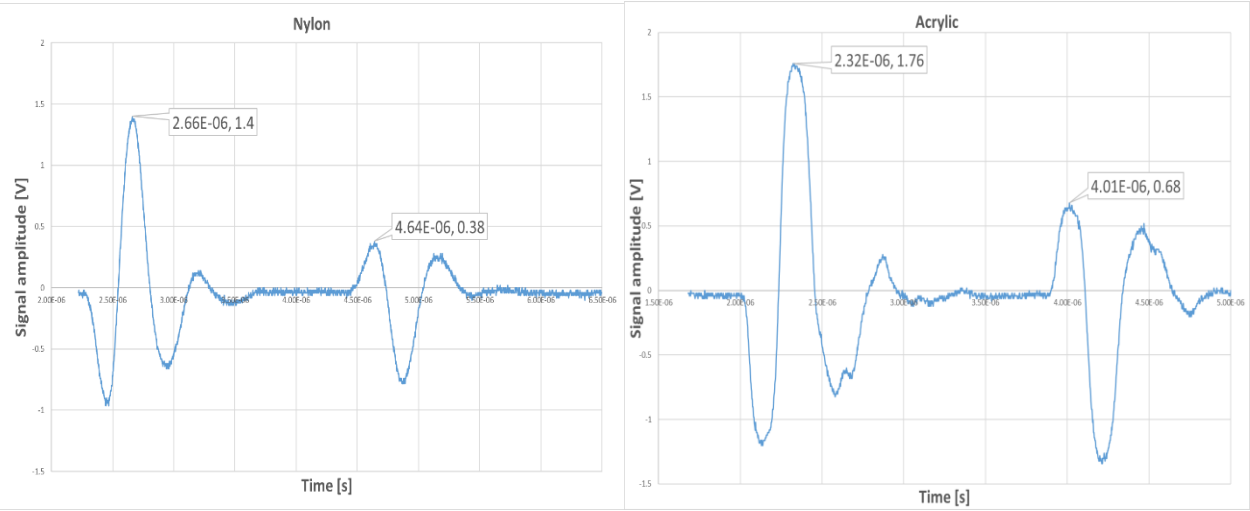

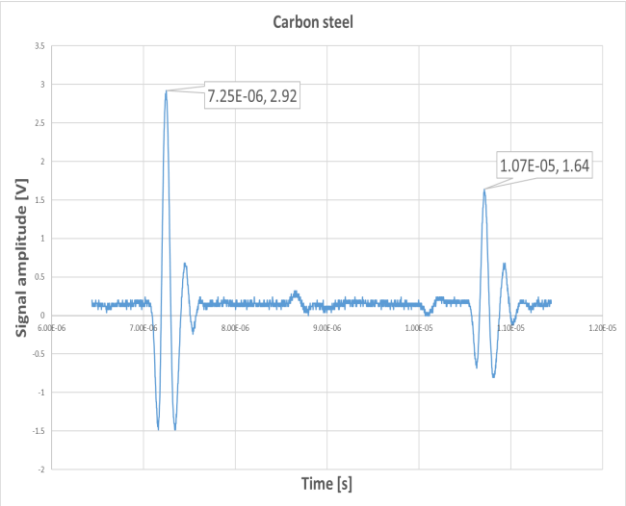

Figure A.4 Signal transmitted by the 2.25 MHz probe with compression waves on Nylon (top-left) and Acrylic (top-right) samples for the 2.5 mm step. Signal of compression waves emitted by the 5 MHz probe through the 10 mm carbon steel step. (bottom)

From the same graph, it is possible to make an analysis of how the signal decays in the sample, that is, its attenuation. This is provided either by the decay rate of the signal passing through the same sample or by the decay rate of the back wall echoes [99]. The attenuation coefficient α [dB/mm], which quantifies the reduction in signal amplitude, can then be calculated using the formula (A.2):

$$\alpha = \frac{20}{2x}\log\frac{A_0}{A_1} \tag{A.2}$$

where x [mm] is the sample thickness, A_0 and A_1 are the amplitudes of the first and second echo respectively [dB].

BIBLIOGRAPHY

[1] YOUSSEF, H.A., EL-HOFY, H., 2008. *Machining technology: machine tools and operations*. CRC Press. *Mentioned in:* HONARVARA, F., VARVANI-FARAHANI, A., December 2020. A review of ultrasonic testing applications in additive manufacturing: Defect evaluation, material characterization, and process control. *Ultrasonics,* 108

[2] CHENOT, J., WAGONER, R., 1997. *Fundamentals of metal forming*, John Wiley & Sons. *Mentioned in* : HONARVARA, F., VARVANI-FARAHANI, A., December 2020. A review of ultrasonic testing applications in additive manufacturing: Defect evaluation, material characterization, and process control. *Ultrasonics,* 108

[3] CRAEGHS, T., et al., 2010. Feedback control of layerwise laser melting using optical sensors, *Physics Procedia,* 5, (B), pp 505-514, available on < https://doi.org/10.1016/j.phpro.2010.08.078> Mentioned in: CHEN, Y., et al., 2021, Defect inspection technologies for additive manufacturing, *International Journal of Extreme Manufacturing*, 3, (2) available on < https://doi.org/10.1088/2631-7990/abe0d0> [Date of access 28/04/2022]

[4] MOON, S.K., et. al. 2014. Application of 3D printing technology for designing light-weight unmanned aerial vehicle wing structures. *International Journal of Precision Engineering and Manufacturing-Green Technology.* 1**,** pp**.** 223–228, available on <https://doi.org/10.1007/s40684-014-0028-x>. Mentioned in CHEN, Y., et al., 2021, Defect inspection technologies for additive manufacturing, *International Journal of Extreme Manufacturing*, 3, (2) available on < https://doi.org/10.1088/2631-7990/abe0d0> [Date of access 28/04/2022]

[5] February 10, 2011. The Printed World: Threedimensional printing from digital designs. *The Economist* [online], available on <https://www.economist.com/briefing/2011/02/10/the-printed-world>. Mentioned in: CARR, S., October 16, 2017. OFFICE OF ENERGY EFFICIENCY & RENEWABLE ENERGY, *What is Additive Manufacturing?* [online], available on

<https://www.energy.gov/eere/articles/what-additive-manufacturing#1> [Date of access: 09/03/2022]

[6] TRACTUS 3D, *Advantages of 3D printing (and disadvantages)* [online], available on <https://tractus3d.com/knowledge/learn-3d-printing/advantages-of-3d-printing#:~:text=TL%3BDR%20%3A%20The%20main%20advantages%20of%203D%20printing,competitive%20advantage%2C%20reduce%20errors%2C%20confidentiality%2C%20production%20on%20demand.> [Date of access: 22/03/2022]

[7] AFFORDABLE HOUSING TIPS [online], available on < https://affordablehousingtips.com/newsarticle/3d-printed-house-guide-affordable-housing/#:~:text=The%20time%20frame%20depends%20on%20the%20size%20of,can%20already%20be%20printed%20in%20under%2024%20hours.> [Date of access: 22/03/2022]

[8] LANZETTA, M., and SACHS, E., 2003. "Improved surface finish in 3D printing using bimodal powder distribution", *Rapid Prototyping Journal,* 9 (3), pp. 157-166, available on <https://doi.org/10.1108/13552540310477463>. Mentioned in CHARALAMPOUS, P., KOSTAVELIS, I., AND TZOVARAS, D., 2020, Non-destructive quality control methods in additive manufacturing: a survey, *Rapid Prototyping Journal*, 26 (4), pp. 777-790, available on <https://doi.org/10.1108/RPJ-08-2019-0224>

[9] MYMODERNMET, *Complex Geometric Lamp Designs Produced with 3D Printing* [online], available on <https://mymodernmet.com/bathsheba-grossman-3d-printed-lamps/> [Date of access 22/03/2022]

[10] ICON, [online], available on <https://www.iconbuild.com/> [Date of access: 22/03/2022]

[11] NING, F., et. al., 2015. Additive Manufacturing of Carbon Fibre Reinforced Thermoplastic Composites Using Fused Deposition Modeling. *Composites Part B: Engineering*, 80, pp. 369-378, available on <http://dx.doi.org/10.1016/j.compositesb.2015.06.013>. Mentioned in MARTINS, A., P., et. al., Simulation of NDT methods for Additive Manufacturing of composites. *12th European Conference on Non-Destructive Testing (ECNDT 2018),* June 11-15 2018, Gothenburg, Sweden.

[12] MOHSEN, A., 2017 The rise of 3-D printing: The advantages of additive manufacturing over traditional manufacturing. *Business Horizons.* 60 (5), pp. 677-688, available on <https://doi.org/10.1016/j.bushor.2017.05.011>

[13] SATISH PRAKASH, K., NANCHARAIH, T., and SUBBA RAO, V.,V., 2018. Additive Manufacturing Techniques in Manufacturing - An Overview. *Materials Today: Proceedings*, 5 (2), pp. 3873-3882, available on < https://doi.org/10.1016/j.matpr.2017.11.642.>

[14] IRONCAD, *6 Advantages of 3D Printing vs Injection Molding* [online], available on <6 Advantages of 3D Printing vs Injection Molding | IronCAD CAD Software Solutions> [Date of access: 25/05/2022]

[15] 3DSOURCED, *6 Exciting 3D Printed Organs & 3D Bioprinting Projects* [online], available on <6 Exciting 3D Printed Organs & 3D Bioprinting Projects - 3DSourced>. [Date of access: 23/05/2022]

[16] KING, R., 2012. 3D Printing Coming to the Manufacturing Space and Outer Space. *Bloomberg LP*, *Bloomberg*. Mentioned in: MOHSEN, A., 2017 The rise of 3-D printing: The advantages of additive manufacturing over traditional manufacturing. *Business Horizons.* 60 (5), pp. 677-688, available on <https://doi.org/10.1016/j.bushor.2017.05.011>

[17] TRAN, J.L., 2016. 3D-printed food. *Minnesota Jourrnal of Law, Science & Technology*, *17 (1)*, pp.855.

[18] GIBSON, I., ROSEN, D., and STUCKER, B., 2014. *Additive manufacturing technologies: 3D printing, Rapid Prototyping and Direct Digital Manufacturing.* 2° ed. Berlin: Springer. Mentioned in CHARALAMPOUS, P., KOSTAVELIS, I., AND TZOVARAS, D., 2020, Non-destructive quality control methods in additive manufacturing: a survey, *Rapid Prototyping Journal*, 26 (4), pp. 777-790, available on <https://doi.org/10.1108/RPJ-08-2019-0224>

[19] MSALLEM, B., et. al., 2017. Craniofacial Reconstruction by a Cost-Efficient Template-Based Process Using 3D Printing. *Plastic and reconstructive surgery. Global open*, 5 (11), e1582, available on <https://doi.org/10.1097/GOX.0000000000001582>. Mentioned in: ROONEY, S.C.,

POCHIRAJU, K., 2019. Simulations of Online Non-Destructive Acoustic Diagnosis of 3D-Printed Parts Using Air-Coupled Ultrasonic Transducers. *Advanced Manufacturing,* 2A, available on <https://doi.org/10.1115/IMECE2019-11101>

[20] Lux Research. 2013. Building the future: Assessing 3-D printing's opportunities and challenges. Boston: Lux Research Inc. Mentioned in: MOHSEN, A., 2017 The rise of 3-D printing: The advantages of additive manufacturing over traditional manufacturing. *Business Horizons.* 60 (5), pp. 677-688, available on <https://doi.org/10.1016/j.bushor.2017.05.011>

[21] IMARC, *3D Printing Market: Global Industry Trends, Share, Size, Growth, Opportunity and Forecast 2022-2027* [online], available on < 3D Printing Market Report, Size, Share and Analysis 2022-27 (imarcgroup.com)> [Date of access: 23/05/2022]

[22] ZELTMANN, S.E., et al. 2016. Manufacturing and Security Challenges in 3D Printing. *JOM*, 68 (7), pp. 1872–1881, available on <https://doi.org/10.1007/s11837-016-1937-7>

[23] LONGWEI Y., et. al., 2016. The Fused Deposition Modeling 3D Printing. *Proceedings of the 2016 International Conference on Electrical, Mechanical and Industrial Engineering,* available on <https://doi.org/10.2991/icemie-16.2016.50>

[24] MANUFACTUR3D, April 6, 2018. *The 7 Types of Additive Manufacturing Technologies* [online], available on <https://manufactur3dmag.com/7-types-additive-manufacturing-technologies/#1_Material_Extrusion> [Date of access: 09/03/2022]

[25] CHEN, Y., et al., 2021. Defect inspection technologies for additive manufacturing, *International Journal of Extreme Manufacturing*, 3, (2), available on < https://doi.org/10.1088/2631-7990/abe0d0> [Date of access 28/04/2022]

[26] MAKER INDUSTRY, January 5, 2022. *FFF vs FDM: Is there any difference?* [online], available on <FFF vs FDM: Is there any difference? - Maker Industry> [Date of access: 25/05/2022]

[27] HUBS, *What is FDM (Fused Deposition Modeling) 3D printing? Explained by Hubs* [online], available on <https://www.hubs.com/knowledge-base/what-is-fdm-3d-printing/> [Date of access: 26/05/2022]

[28] HUBS, *FDM 3D printing materials compared* [online], available on <FDM 3D printing materials compared | Hubs> [Date of access: 26/05/2022]

[29] MWEMA, F.M., AKINLABI, E.T., 2020. Basics of Fused Deposition Modelling (FDM). In: Fused Deposition Modeling. SpringerBriefs in Applied Sciences and Technology. Springer, Cham., available on <https://doi.org/10.1007/978-3-030-48259-6_1>

[30] KRISZTIÁN K., 2016. Reconstruction and Development of a 3D Printer Using FDM Technology, *Procedia Engineering,* 149, pp. 203-211, available on < https://doi.org/10.1016/j.proeng.2016.06.657>

[31] DEY, A., YODO, N., 2019. A Systematic Survey of FDM Process Parameter Optimization and Their Influence on Part Characteristics, *Journal of Manufacturing and Materials Processing*, 3 (3): 64, available on <**https://doi.org/10.3390/jmmp3030064**>

[32] BOCHMANN, L., et al., 2015. Understanding error generation in fused deposition modeling, *Surface Topography: Metrology and Properties*, 3 (1), available on <Understanding error generation in fused deposition modeling - IOPscience>

[33] HUBS, *Selecting the optimal shell and infill parameters for FDM 3D printing* [online], available on <Selecting the optimal shell and infill parameters for FDM 3D printing | Hubs> [Date of access: 29/05/2022]

[34] ANITHA, R., ARUNACHALAM, S., and RADHAKRISHNAN, P., 2001. Critical parameters influencing the quality of prototypes in fused deposition modelling, *Journal of Materials Processing Technology*, 118 (1-3), pp. 385-388, available on <https://doi.org/10.1016/S0924-0136(01)00980-3>

[35] GUNAYDIN, K., TÜRKMEN, H., 2018. Common FDM 3D Printing Defects. *International Congress on 3D Printing (Additive Manufacturing) Technologies and Digital Industry*. 19-21 April 2018.

[36] BAUMANN, F., ROLLER, D., 2016. Vision based error detection for 3D printing processes. *MATEC Web of Conferences,* 59, available on <https://doi.org/10.1051/matecconf/20165906003>

[37] DYE, D., HUNZIKER, O., REED, R.C., 2001. Numerical analysis of the weldability of superalloys, *Acta Materialia*, 49 (4), pp. 683-697, available on < https://doi.org/10.1016/S1359-6454(00)00361-X>

[38] MERCELIS, P., KRUTH, J., 2006. Residual stresses in selective laser sintering and selective laser melting, *Rapid Prototyping Journal*, 12 (5), pp. 254-265, available on <https://doi.org/10.1108/13552540610707013>

[39] DEMIR, A.G., PREVITALI, B., 2017. Investigation of remelting and preheating in SLM of 18Ni300 maraging steel as corrective and preventive measures for porosity reduction. *The International Journal of Advanced Manufacturing Technology*, 93, pp. 2697–2709, available on <https://doi.org/10.1007/s00170-017-0697-z>

[40] BERNHARD R., et al., 2020. Defect detection in additive manufacturing via a toolpath overlaid melt-pool-temperature tomography, *Journal of Laser Applications*, 32, available on <https://doi.org/10.2351/7.0000055>

[41] TIAN, L., et al., 2020. Identifying flow defects in amorphous alloys using machine learning outlier detection methods, *Scripta Materialia*, 186, pp. 185-189, available on <https://doi.org/10.1016/j.scriptamat.2020.05.038>

[42] MECH STUDIES, *What is a Non-Destructive Testing (NDT) – Methods, Advantages & Disadvantages* [online], available on < https://www.mechstudies.com/what-non-destructive-testing-ndt-methods/> [Date of access: 23/03/2022]

[43] CHARALAMPOUS, P., KOSTAVELIS, I., AND TZOVARAS, D., 2020, Non-destructive quality control methods in additive manufacturing: a survey, *Rapid Prototyping Journal*, 26 (4), pp. 777-790, available on <https://doi.org/10.1108/RPJ-08-2019-0224>

[44] SUNDAR, September 18, 2018. *What are the Non-Destructive testing methods?* [online]. Extrudesign.com. available on https://extrudesign.com/what-are-the-non-destructive-testing-methods/ [Date on access: 12/03/2022]

[45] RUUD, C.O., GREEN, R., 1984. *Nondestructive Methods for Material Property* Determination. New York: Plenum Press. pp. 410. Mentioned in: JIN. Y., et al. 2020. Nondestructive ultrasonic evaluation of fused deposition modeling based additively manufactured 3D-printed structures, *Smart Mater. Struct,* 29 (4)

[46] BRITISH INSTITUTE OF NON-DESTRUCTIVE TESTING, November 2015. *Non-Destructive Testing (NDT) – Guidance Document: An Introduction to NDT Common Methods*.

[47] ROSE, J.L., 2014. *Ultrasonic guided waves in solid media*. Cambridge university press. *Mentioned in:* HONARVARA, F., VARVANI-FARAHANI, A., December 2020. A review of ultrasonic testing applications in additive manufacturing: Defect evaluation, material characterization, and process control. *Ultrasonics,* 108

[48] DECLERCQ, N.F., 2014. Experimental study of ultrasonic beam sectors for energy conversion into Lamb waves and Rayleigh waves. *Ultrasonics. 54 (2), pp 609-613 available on <https://doi.org/10.1016/j.ultras.2013.08.016> Mentioned in:* HONARVARA, F., VARVANI-FARAHANI, A., December 2020. A review of ultrasonic testing applications in additive manufacturing: Defect evaluation, material characterization, and process control. *Ultrasonics,* 108

[49] SRAVANTH, C., et al., Snell's Law. *Brilliant.org*. Retrieved 12:44, April 20, 2022, available on <https://brilliant.org/wiki/snells-law/>

[50] ASTRONOMIA.COM, April 24, 2013. *Applichiamo la diffrazione al telescopio*, [online], available on <https://www.astronomia.com/2013/04/24/applichiamo-la-diffrazione-al-telescopio/> [Date of access: 26/03/2022]

[51] IOWA STATE UNIVERSITY CENTER FOR NONDESTRUCTIVE EVALUATION, Ultrasonic Testing [online], available on <https://www.nde-ed.org/NDETechniques/Ultrasonics/index.xhtml> [Date of access: 28/03/2022]

[52] WORLD OF NDT, March 18, 2020. *Equipment used in Ultrasonic Testing [online],* available on <https://worldofndt.com/equipment-used-in-ultrasonic-testing/> [Date of access: 26/03/2022]

[53] RATHOD, V. T., 2020. A Review of Acoustic Impedance Matching Techniques for Piezoelectric Sensors and Transducers. *Sensors*. 20 (14), available on <**https://** DOI:10.3390/s20144051>

[54] FLYABILITY. *Ultrasonic testing: guide* [online], available on <https://www.flyability.com/ultrasonic-testing> [Date of access: 28/03/2022]

[55] SRIVASTAVA, A., et al., Automated Ultrasonic Immersion Through Transmission Imaging Technique - A Novel Way to Evaluate Dissimilar Metal Joints. *NDE 2018 Conference & Exhibition of the society for NDT (ISNT).* 19-21 December 2018, Mumbai, India.

[56] SCRUBY, C.B., 1987. An introduction to acoustic emission. *Journal of Physics E: Scientific Instruments*. 20 (946), available on <https://iopscience.iop.org/article/10.1088/0022-3735/20/8/001>

[57] KANJI, O., 2014. *Springer Handbook of Acoustics.* New York, NY: Rossing, T.D. pp 1209–1229, available on <https://doi.org/10.1007/978-1-4939-0755-7_30>

[58] SOLODOV, I., BUSSE, G., 2006. New Advances in Air-Coupled Ultrasonic NDT Using Acoustic Mode Conversion. In *ECNDT, European Conference on Non-Destructive Testing.* Berlin.

[59] ROSE, J., et al., 2000. Flaw sizing potential with guided waves. *AIP Conference Proceedings* [online], 509 (927), available on < https://doi.org/10.1063/1.1306144>

[60] MASLAKOWSKI, M.S., et al., 2020, November. The Characterization and Assembly of an Efficient, Cost Effective Focused Ultrasound Transducer. In *2020 IEEE 14th Dallas Circuits and Systems Conference (DCAS)* (pp. 1-6). IEEE.

[61] PARKER, L., 2015. Applications of Ultrasonic Non-Destructive Testing in 3D Printing. *The Journal of Undergraduate Research*. 13 (4), available on <http://openprairie.sdstate.edu/jur/vol13/iss1/4>

[62] MATERIAL WELDING, Types of ultrasonic testing Displays: A-scan B-scan and C-scan, [online] available on <https://www.materialwelding.com/types-of-ultrasonic-testing-displays-a-scan-b-scan-and-c-scan/?msclkid=caf72754ba4811eca87d371b8fb29bb7> [Date of access: 28/03/2022]

[63] SALSKI, B., GWAREK, W., KORPAS, P., RESZEWICZ, S., CHONG, A., THEODORAKEAS, P., HATZIIOANNIDIS, I., KAPPATOS, V., SELCUK, C., GAN, T. H., KOUI, M., IWANOWSKI, M., ZIELINSKI, B. 2015. Non-destructive testing of carbon-fibre-reinforced polymer materials with a radio-frequency inductive sensor. *Composite Structures*. 122, pp.104-112, available on <https://doi.org/10.1016/j.compstruct.2014.11.056>.

[64] BLOMME, E., BULCAEN, D., and DECLERCQ, F., 2002. Air-coupled ultrasonic NDE: experiments in the frequency range 750kHz–2MHz. *NDT & E International*, 35 (7), pp 417-426, available on <https://doi.org/10.1016/S0963-8695(02)00012-9>

[65] ACHENBACH, J.D., 2000. Quantitative nondestructive evaluation. *International Journal of Solids and Structures.* 37 (1-2), pp 13-27, available on <https://doi.org/10.1016/S0020-7683(99)00074-8>

[66] SCHINDEL, D.W., 1999. Air-coupled ultrasonic measurements of adhesively bonded multi-layer structures. *Ultrasonics*, 37 (3), pp 185-200, available on <https://doi.org/10.1016/S0041-624X(98)00061-4>

[67] ROSTKOWSKI, K., MAGHBOOLI, N., 2019. Air Coupled Ultrasound-New approaches in the field of coupling agent-free testing. *Proceedings of the 5th Iranian International NDT Conference,* 4-5 November 2018, Olympic Hotel, Tehran, Iran

[68] WRIGHT, W.M., SCHINDEL, D.W., and HUTCHINS, D.A., 1994. Studies of laser-generated ultrasound using a micromachined silicon electrostatic transducer in air. *Journal of the Acoustical*

Society of America, 95, pp 2567-2575, available on <https://doi.org/10.1121/1.409826>. Mentioned in SCHINDEL, D.,W., 1999. Air-coupled ultrasonic measurements of adhesively bonded multi-layer structures. *Ultrasonics*, 37 (3), pp 185-200, available on <https://doi.org/10.1016/S0041-624X(98)00061-4>

[69] SCHINDEL, D.W., HUTCHINS, D.A., 1995. Through-thickness characterization of solids by wideband air-coupled ultrasound. *Ultrasonics,* 33, (1), pp 11-17 available on <https://doi.org/10.1016/0041-624X(95)00011-Q>

[70] SCHINDEL, D.W., HUTCHINS, D.A., 1998. Non-contact characterization and inspection of materials using wideband air-coupled ultrasound. US Patent 5,824,908 available on <US5824908A - Non-contact characterization and inspection of materials using wideband air coupled ultrasound - Google Patents>. Mentioned in SCHINDEL, D.W., 1999. Air-coupled ultrasonic measurements of adhesively bonded multi-layer structures. *Ultrasonics*, 37 (3), pp 185-200, available on <https://doi.org/10.1016/S0041-624X(98)00061-4>

[71] SCHINDEL, D.W., 1997. Air-coupled generation and detection of ultrasonic bulk waves in metals using micromachined capacitance transducers. *Ultrasonics,* 35 (2), pp 179–181, available on <https://doi.org/10.1016/S0041-624X(96)00103-5>. Mentioned in ÁLVAREZ-ARENAS, TOMÁS, G., and CAMACHO, J., 2019. "Air-Coupled and Resonant Pulse-Echo Ultrasonic Technique" *Sensors* [online], 19 (10: 2221) available on <https://doi.org/10.3390/s19102221> [Date of access: 30/04/2022]

[72] ÁLVAREZ-ARENAS, TOMÁS, G., and CAMACHO, J., 2019. "Air-Coupled and Resonant Pulse-Echo Ultrasonic Technique". *Sensors* [online], 19 (10: 2221) available on <https://doi.org/10.3390/s19102221> [Date of access 30/04/2022]

[73] STOESSEL, R., et al., 2002. Air-coupled ultrasound inspection of various materials. *Ultrasonics,* 40 (1-8), pp 159-163, available on <https://doi.org/10.1016/S0041-624X(02)00130-0>

[74] ESSIG, W., et al., 2021. Air-coupled Ultrasound – Emerging NDT Method, pp 32-43, available on <(PDF) Air-coupled Ultrasound – Emerging NDT Method (researchgate.net)>

[75] HICKLING, R., MARIN, S.P., 1986. The use of ultrasonics for gauging and proximity sensing in air. *The Journal of the Acoustical Society of America* [online], 79 (1151) available on <https://doi.org/10.1121/1.393387>

[76] WRIGHT, W.M.D., HUTCHINS, D.A., 1999. Air-coupled ultrasonic testing of metals using broadband pulses in through-transmission. *Ultrasonics*, 37 (1), pp 19-22, available on < https://doi.org/10.1016/S0041-624X(98)00034-1>

[77] MINASI, M. 2015. *How to Select and Mount Transducers in Ultrasonic Sensing for Level Sensing and Fluid ID* [online], available on <https://www.ti.com/lit/an/snaa266a/snaa266a.pdf> [Date of access: 30/06/2022]

[78] BANNER, *Ultrasonic Sensors 101: Answers to Frequently Asked Questions* [online], available on <Ultrasonic Sensors: Answers to Frequently Asked Questions (bannerengineering.com)> [Date of access: 07/06/2022]

[79] GÓMEZ ÁLVAREZ-ARENAS, T.E., and ESPINOSA, F., 2011. Materiales y técnicas para el acoplamiento mecánico óptimo de piezocerámicas en aire. *Boletín de la Sociedad Española de Cerámica y Vidrio*, 41 (1), pp. 16-21, available on <http://doi:10.3989/cyv.2002.v41.i1.690>

[80] GÓMEZ ALVAREZ-ARENAS, T.E., 2004. Acoustic impedance matching of piezoelectric transducers to the air. *IEEE Transactions on Ultrasonics, Ferroelectrics, and Frequency Control*, 51 (5), pp. 624-633, available on <http://doi:10.1109/TUFFC.2004.1320834>

[81] SCHINDEL, D.W., HUTCHINS, D.A., and GRANDIA, W.A., 1996. Capacitive and piezoelectric air-coupled transducers for resonant ultrasonic inspection, *Ultrasonics*, 34 (6), pp 621-627, available on <https://doi.org/10.1016/0041-624X(96)00063-7>

[82] HUTCHINS, D.A., WRIGHT, W.M.D., and SCHINDEL, D.W., 1994. Ultrasonic measurements in polymeric materials using air-coupled capacitance transducers. *The Journal of the Acoustical Society of America* [online], 96 (3) available on < https://doi.org/10.1121/1.410243>

[83] SCHINDEL, D.W., et al. 1995. The design and characterization of micromachined air-coupled capacitance transducers. *IEEE Transactions on Ultrasonics, Ferroelectrics and Frequency Control*, 42 (1), pp. 42-50, available on < https://doi.org/10.1109/58.368314>

[84] GAAL, M., et al., 2016. Focusing of ferroelectret air-coupled ultrasound transducers. *AIP Conference Proceedings* [online], 1706 (1), available on <https://doi.org/10.1063/1.4940533>

[85] MATTE RHACKERS, *3D printer filament comparison guide* [online], available on <https://www.matterhackers.com/3d-printer-filament-compare> [Date of access: 06/07/2022]

[86] ALL3DP, *The Ultimate Filament Guide, Best 3D Printer Filament: The Types in 2022* [online], available on <https://all3dp.com/1/3d-printer-filament-types-3d-printing-3d-filament/> [Date of access: 06/07/2022]

[87] ETHAN C., *PLA vs ABS Filament – Plastic Strength, Flexibility Compared! Buyer's Guide 2022* [online], available on <https://www.allthat3d.com/pla-vs-abs/> [Date of access: 06/07/2022]

[88] ULTIMAKER, [online], available on <https://ultimaker.com/3d-printers/ultimaker-s3> [Date of access: 11/07/2022]

[89] ULTIMAKER, [online], available on <https://ultimaker.com/3d-printers/ultimaker-s5> [Date of access: 11/07/2022]

[90] 3D NATIVES, *Compare 3D Printers* [online], available on <https://www.smg3d.co.uk/stratasys/dimension_elite_3d_printer> [Date of access: 11/07/2022]

[91] AIMTTI, [online], available on <https://www.aimtti.com/product-category/pulse-generators/aim-tgp110> [Date of access: 13/07/2022]

[92] FALCO SYSTEM, [online], available on < https://www.falco-systems.com/High_voltage_amplifier_WMA-300.html> [Date of access: 13/07/2022]

[93] DELTA ELEKTRONIKA, [online], available on <https://www.delta-elektronika.nl/upload/DATA_SHEET_ES150.pdf> [Date of access: 18/07/2022]

[94] TEKTRONIX, [online], available on <https://www.tek.com/en/datasheet/tds200-series> [Date of access: 18/07/2022]

[95] SENSCOMP, [online], available on <https://senscomp.com/wp-content/uploads/2019/12/Series-600-Envir-Grade-Ultrasonic-Sensor-Spec-03Mar15-1.pdf> [Date of access: 18/07/2022]

[96] CERUTTI, M., 2002. Principi dell'analisi ad ultrasuoni. *Nautica,* 487

[97] SIGNAL PROCESSING, *acoustic properties of...* [online], available on <https://www.signal-processing.com/table.php> [Date of access: 04/07/2022]

[98] CALCULLA, *Speed of sound in various mediums table* [online], available on <https://calculla.com/sound_velocity_table> [Date of access: 04/07/2022]

[99] KARTHIK, N.V., GU, H. PAL, D., STARR, T., STUCKER, B., 2013. High frequency ultrasonic non destructive evaluation of additively manufactured components. *24th International SFF Symposium - An Additive Manufacturing Conference*, pp. 311-325.